Exploratory Investigation of Forebody Strakes for Yaw Control of a Generic Fighter With a Symmetric 60˚ Half-Angle Chine Forebody

Holly M. Ross
Langley Research Center • Hampton, Virginia

Matthew J. O'Rourke
Lockheed Martin Engineering & Sciences Company • Hampton, Virginia

April 1997

Summary

Forebody strakes were tested in the Langley 12-Foot Low-Speed Tunnel to determine their effectiveness producing yaw control on a generic fighter model incorporating a forebody with a symmetric 60° half-angle chine cross section. Previous studies show that forebody strakes provide increased levels of yaw control at angles of attack where conventional rudders are ineffective. These studies were conducted using smooth, conventionally shaped forebodies. The chine forebody shape was chosen for this study because chine forebodies can be designed with lower radar cross section (RCS) values than smooth forebody shapes. Previous studies show that the chine edges of the forebody would fix the point of flow separation and could potentially minimize the effectiveness of a strake, and it was unknown if any effectiveness achieved could be modulated as was successfully done with the smooth forebody shapes.

The results show that use of forebody strakes on a chine forebody produce high levels of yaw control, and when combined with rudder effectiveness, significant yaw control is available for a large range of angles of attack. The strake effectiveness was very dependent on radial location, with the most effective location being either on the chine line or slightly above it. Very small strakes placed at the tip of the forebody were nearly as effective as very long strakes. Control modulation by deflecting the strake did not work well for any of the many strake shapes tested. However, an axial translation scheme provided almost linear increments of control effectiveness.

Introduction

During modern air combat, aircraft detection by ground- or air-based avionics or weapons systems can easily occur outside of the visual range of the people involved, and an entire battle can take place without establishing visual contact. For the next generation of combat aircraft, the ability to avoid detection during beyond-visual-range (BVR) engagements is a major design consideration for increasing an aircraft's survivability. Thus, increased attention is being given to lowering the observability of combat aircraft. Observability depends on factors such as the aircraft's visual, acoustic, infrared, and radar signatures (ref. 1). Decreasing any or all of these signatures could enhance the survivability of the aircraft during BVR combat situations.

If a combat engagement progresses to within visual range, survivability becomes less dependent on low observability and more dependent on maneuverability. Achieving victory during an air-to-air battle hinges on the pilot's ability to outmaneuver the enemy. An aircraft with the ability to operate in the post-stall region at slow speeds and high angles of attack would give a pilot the advantage over an opponent. An example of post-stall maneuvering would be longitudinal nose-pointing or a high angle-of-attack roll about the velocity vector used to quickly reposition the nose of the aircraft to acquire a target. These types of maneuvers could give a pilot the tactical advantage needed to achieve victory over an opponent.

A limitation of high angle-of-attack maneuvering is the lack of yaw control available because of ineffectiveness of the vertical tail (or tails) which becomes immersed in the stalled wake behind the fuselage and wing. However, as the yaw control provided by the rudder (or rudders) decreases sharply in this regime, the yaw control required to coordinate rolling maneuvers about the velocity vector increases, as depicted in figure 1. (See ref. 2.) The lack of good coordination in this flight regime could lead to undesirable sideslip conditions that would limit the aircraft's maneuverability.

Forebody aerodynamics play a very important role in an aircraft's high angle-of-attack characteristics because the forebody remains in free-stream air and has a strong vortical flow field. Also, the forebody on most modern fighter aircraft is far ahead of the center of gravity, which gives the forebody a long moment arm (fig. 2). A longer moment arm will produce a larger yawing moment for a given side force. For these reasons, the forebody is a good location for a high angle-of-attack control effector.

Much research has been conducted on the effectiveness of forebody controls for yaw control, including forebody strakes (refs. 3–11) and pneumatic forebody controls (refs. 12–16). This research shows that high levels of yaw control can be achieved at high angles of attack, while conventional aerodynamic controls become ineffective in this regime. These yaw controls act upon the powerful forebody vortical flow field by producing new vortices and modifying the existing forebody vortices, thus generating large yawing moments at high angles of attack. Most forebody controls research has focused on smooth forebody shapes, i.e., circular or elliptical cross sections. However, the next generation of fighter aircraft is likely to have chined forebodies, as seen on the YF-23 and F-22, as a way to reduce the radar cross section (RCS) of the aircraft. Flow separation on chined forebodies is fixed by the chines, and because of this, it was not known if forebody controls could be successfully implemented on a chined forebody.

This study was initiated to determine if forebody strakes could be effective on a configuration with a chined forebody. A generic fighter configuration with a symmetric 60° half-angle chine forebody representative of a next-generation, low-observable fighter aircraft

design was selected for testing. Forebody strakes on a low-observable design were considered operationally feasible because the strakes would not be deployed until a combat engagement progressed to within visual range and maneuvering the aircraft is required. This study includes an evaluation of the effects of strake size, shape, location, and control deployment and linearity.

Symbols

All longitudinal forces and moments are referred to the stability-axis system, and all lateral-directional forces and moments are referred to a body-axis system. The aerodynamic data are referred to a center of gravity located at 41.6 percent of the mean aerodynamic chord (fig. 3(a)). This center of gravity was chosen so that the static longitudinal stability of the baseline full configuration was unstable, with a static margin of -5 percent in the low angle-of-attack range. This amount of instability was considered typical for low-speed conditions so that high-speed trim drag would be minimized.

b wing span, 3.33 ft (40.00 in.)

$\bar{c}$ wing mean aerodynamic chord, 1.83 ft (21.96 in.)

C_l rolling moment coefficient, $\dfrac{\text{Rolling moment}}{\bar{q}Sb}$

C_L lift coefficient, $\dfrac{\text{Lift force}}{\bar{q}S}$

$C_{L,\max}$ maximum value of lift coefficient

C_m pitching moment coefficient, $\dfrac{\text{Pitching moment}}{\bar{q}S\bar{c}}$

C_n yawing moment coefficient, $\dfrac{\text{Yawing moment}}{\bar{q}Sb}$

$C_{n,\max}$ maximum value of yawing moment coefficient

ΔC_n yawing moment due to maximum rudder deflection

C_p local static pressure coefficient, $\dfrac{p_l - p_\infty}{\bar{q}}$

C_R maximum strake width, in.

C_R/R_B ratio of maximum strake width to half width of forebody at forebody base

C_Y side-force coefficient, $\dfrac{\text{Side force}}{\bar{q}S}$

d strake deployment distance, in.

p_l local static pressure, lb/ft^2

p_∞ free-stream static pressure, lb/ft^2

$\bar{q}$ free-stream dynamic pressure, lb/ft^2

r local half width of forebody cross section, in.

R_B half width of forebody cross section at forebody base, in.

S wing reference area, 5.18 ft^2 (745.60 in^2)

x axial location, measured aft from forebody tip along the forebody centerline, in.

y lateral translation distance, in.

Y lateral body axis, positive along right wing

Z directional body axis, positive down

α angle of attack, deg

β angle of sideslip, deg

δ_S strake deflection angle, positive toward forebody upper surface, measured normal to forebody surface (fig. 12), deg

ϕ_S strake radial location on forebody, positive on forebody right side, measured from bottom center position of forebody (fig. 5), deg

Abbreviations:

BVR   beyond visual range

RCS   radar cross section

Model Description and Test Procedure

The model used for this investigation was a generic design intended to conceptually represent a next generation low RCS fighter aircraft (fig. 3(a)). The configuration consisted of a 60° half-angle chine forebody symmetric from top to bottom. The fuselage was circular and the wing planform was a clipped diamond with leading and trailing edge sweep angles of 45° and −20°, respectively. The horizontal tails had the same 45°/−20° planform shape as the wings. The twin vertical tails had leading and trailing edge sweep angles of 30° and −30°, respectively, and were canted 30° outboard from vertical. Figure 3(a) is a three-view sketch of the model with a detail of the forebody cross section, and figure 3(b) is a photo of the model mounted in the wind tunnel. Table I gives the coordinates for the forebody cross section normalized by the forebody cross section local half width.

An aluminum strongback was used as the structure to which the wings, tails, fuselage fairings, and forebody were attached. The wings and tails were flat plates with sharp leading and trailing edges and were constructed from wood. The circular fuselage fairings were also constructed from wood. All edges on the wings and tails were beveled 30° top and bottom. The forebody was machined from aluminum to ensure geometric accuracy, smoothness, and durability. A row of surface static pressure ports was incorporated halfway between the forebody tip and base. Figure 4 shows the radial pressure port locations tested, and the coordinates of the ports are

listed in table II. Because the forebody was chined and the fuselage was circular, there was a transition zone of one fuselage diameter that faired the two shapes starting at the forebody base and extending to the front of the fuselage (fig. 4). Based on maximum forebody width, the fineness ratio was 2.9, or based on the diameter of an equivalent area circle, the fineness ratio was 3.5. The planform of the forebody was a tangent ogive.

The forebody strakes were constructed from thin sheet metal and were generally attached perpendicularly to the forebody surface. The radial locations (ϕ_S) tested are shown in figure 5 and were defined by rays passing through the center of the cross section with $\phi_S = 0°$ located at the bottom center and $\phi_S = 90°$ located at the right-side half-breadth line. Negative values of ϕ_S indicate strakes on the left side of the forebody. Figures 6–11 show sketches of the many strake sizes and shapes tested.

Figure 6 shows the ogival-shaped strakes. The long ogival strakes were designed to be the same length as the forebody with a tangent ogive defining the planform shape. The term C_R/R_B is a ratio used to describe the width of the strake at the strake base and was .3 for the ogive strakes tested. The short ogival strakes were half the length of the long strakes, and the term C_R/R_B is again used to define the width at the strake base. Figure 6 also shows strakes that were derivatives of the .3 short ogival strake. These strakes were designed by using the .3 short ogival strake planform and reducing the length to 1/2, 1/4, 1/8, and 1/16 of the .3 short ogive strake length.

Another family of strakes tested were cropped strakes (fig. 7). Cropped strakes were designed by using the rear half of a long ogival strake and angling the front and back at 45° and −45°, respectively.

A set of very small "micro" strakes were also designed and tested. Two different lengths and widths of cropped strakes and two lengths of a wider delta shape were chosen as the strake planforms. Figure 8 shows the "micro" strake shapes and dimensions.

Several methods of strake deployment were investigated. Because of the model construction, deployment of the strakes had to be simulated by testing strake shapes that represented different stages of the strake deployment. A scheme to deploy strakes by rotating them in planform about a point at the forebody tip was simulated by using long ogive strakes with defined deployment distances d equal to 0.5 in., 0.99 in., and 1.98 in. (fig. 9). Deployment of the cropped strakes involved translation outward from the forebody centerline and was simulated by testing a series of progressively larger cropped strakes with sizes representing a strake moving out from the forebody centerline (fig. 10). Axial translation was also

tested by mounting the .3 short ogive and 1/4 length .3 short ogive strakes at several different axial locations (fig. 11). Strake deflections were performed to simulate a strake that folds out from the forebody surface, and figure 12 defines the convention used for the deflection angle δ_S.

The static force and moment tests, pressure tests, and flow visualization tests on the generic model were conducted at the Langley 12-Foot Low-Speed Tunnel. The dynamic pressure for the pressure and static force and moment testing was 4 lb/ft² which corresponds to a Reynolds number of 674 000 based on the mean aerodynamic chord of the wing. Data were acquired over an angle-of-attack range of 0° to 70° in increments of 5° and over an angle-of-sideslip range of −20° to 20° in increments of 5° with additional points at −2° and 2°. Sideslip runs were conducted moving from −20° to 20° in a continuous manner. The static pressure data were acquired by the data acquisition system concurrent with the force and moment data.

Flow visualization was performed using vaporized propylene glycol and a laser light sheet. The flow visualization tests were run at a dynamic pressure of 0.25 lb/ft², which corresponds to a Reynolds number of 168 500 based on the mean aerodynamic chord of the wing. The flow visualization testing was performed at a lower dynamic pressure to permit denser, more visible vapor. The low Reynolds number of the testing was not believed to greatly impact the data because separation was fixed by both the forebody chines and the forebody strakes.

Results and Discussion

Baseline Configuration Results

Figure 13 presents the baseline lateral-directional characteristics for the forebody alone configuration and the full configuration. The forebody alone configuration consists of the forebody mounted on the fuselage without the wings or tail surfaces. This configuration was tested to investigate what effect the wings and tails had on the aerodynamic characteristics.

Both the forebody alone and full configurations demonstrated a natural yawing moment asymmetry. This was not unexpected because this yawing moment phenomenon has been seen in numerous studies. Reference 17 explains the generation of nonzero side forces and yawing moments in zero sideslip conditions. Because the side force and yawing moment in figure 13 are the same sign, the force causing the yawing moment occurred in front of the center of gravity, indicating it was caused by the formation of asymmetric forebody vortices. This asymmetry was greater for the full

configuration, indicating that the asymmetry of the forebody vortices was enhanced by interactions with the wings and tail surfaces.

.3 Long Ogive Strake Results

Forebody alone. The .3 long ogive strake was the only strake tested on the forebody alone configuration. All right-side radial locations (positive ϕ_S) shown in figure 5 were tested. Figures 14 and 15 show the results for the lower surface and upper surface locations, respectively. The yawing moment coefficients (fig. 14) indicate that for the baseline, strake-off condition, a naturally occurring asymmetry existed that caused a positive yawing moment, also seen in figure 13. The strake at $\phi_S = 30°$ was ineffective, and at $\phi_S = 76°$ a small amount of asymmetric control was produced. However, with a strake at $\phi_S = 54°$ or $90°$ greater asymmetry was achieved, with the $\phi_S = 54°$ location creating a positive moment (pulling towards the strake) between $\alpha = 20°$–$70°$ and $\phi_S = 90°$, creating a negative moment (away from the strake) between $\alpha = 10°$–$70°$.

Figure 15 shows data for upper-surface mounted strakes. The location that provided the greatest yawing moment was $\phi_S = 104°$ which gave negative yawing moments (away from the strake) between $\alpha = 10°$–$70°$. The strake at $\phi_S = 104°$, which worked similarly to the strake at $\phi_S = 90°$, created a force to the left.

Figure 16 shows surface static pressure vector plots for the baseline and the most effective .3 long ogive strake locations ($\phi_S = 54°$, $90°$, and $104°$) for $\alpha = 50°$. These data are presented with the surface static pressure values shown as vectors normal to the surface at each port location. Each ring of the polar grid represents an increment value of $C_p = 1.0$. Arrows pointing away from the surface indicate suction and arrows pointing toward the surface indicate compression. Areas with no visible arrows have pressures near free-stream or zero C_p values.

The pressure data in this report should be interpreted with some caution. With only one pressure port ring, the longitudinal variability of the forebody flow field was not always captured. This was especially true because of the presence of strakes on the forebody. Also, the pressure plots may not look like the flow visualization pictures or sketches presented because most of the flow visualization information presented shows the flow field aft of the pressure port ring.

The pressure distribution for the strake off, baseline configuration (fig. 16(a)) shows the presence of vortex formation above the chine regions, evidenced by the suction in those areas. The right-side vortex was presumed to be close to the surface and is indicated by the large suction values, while the left-side vortex was believed to

be farther from the surface. The resulting asymmetry caused a force to the right side, creating the positive yawing moment seen in the force data.

With the .3 long ogive strake at $\phi_S = 54°$ it is likely that a vortex formed off the strake and affected the chine vortex. The area of suction on the right side (fig. 16(b)) indicates that the vortex was much closer to the chine line than on the baseline configuration. Also, part of the vortex created off the strake became trapped between the strake and the chine, creating a large suction area below the chine. Thus, the resulting force was to the right.

With the same strake at $\phi_S = 90°$ (fig. 16(c)), it is believed that the strake acted like a spoiler by forcing the forebody flow to separate at the strake edge and then directing the separated flow away from the forebody surface. However, the increased suction on the left side indicates that the left-side vortex was able to remain close to the surface because of the displaced right-side flow. Because the left side of the forebody had a larger area over which low pressure was acting and the right-side vorticity was farther from the body, the resulting force was to the left (away from the strake).

Figure 16(d) shows the effect of the strake at $\phi_S = 104°$. The resulting pressure distribution shows the right-side system had lower suction pressures than the other strake positions. The pressure data for the area between the strake and the chine show only small suction values, indicating that the chine vortex was pushed away from the surface by the strake. On the left side of the forebody, the suction values were much greater and provided the resulting force to the left.

Figure 17 summarizes the yawing moment coefficient as a function of the strake radial location at $\alpha = 50°$, which is the angle of attack where yawing moments were close to their maximum value. In general, the lower surface strakes caused a positive moment (force towards the strake) while the upper surface strakes caused a negative moment (force away from the strake) with the crossover point occurring between $\phi_S = 76°$ and $90°$. These results were very similar to the results detailed in reference 3.

Full configuration—effect of radial location. Based on forebody alone testing results, the most effective strake locations, $\phi_S = 54°$, $90°$, and $104°$, were chosen for further investigation with the full configuration. Figure 18 shows the lateral-directional characteristics for the .3 long ogive strake comparing the three selected radial locations. Also included in figure 18 is the rudder effectiveness obtained by deflecting the rudders $30°$ with no strakes. The rudder data shown are ΔC_n, which has the naturally occurring yawing moment asymmetry subtracted so only the rudder contribution is shown. The

rudder power began to diminish at about $\alpha = 20°$ and was nearly zero by $\alpha = 30°$.

The strake-off asymmetry started at about $\alpha = 30°$. With a strake at $\phi_S = 54°$ a large positive yawing moment occurred as it did with the forebody alone, and for $\phi_S = 90°$ and $104°$ a negative yawing moment occurred. The maximum magnitudes were higher in all cases with the full configuration when compared to the forebody alone, but the trends remained the same. It was thus concluded that the addition of the wings and tails did not cause the yawing moment asymmetries, but the increases in magnitudes were attributed to forebody vortex interactions with the wings and tails.

The strake at $\phi_S = 54°$ was the least effective because the asymmetry began at $\alpha = 25°$ compared to $\alpha = 5°$ for $\phi_S = 90°$ and $104°$. With the contribution from the strakes at either $\phi_S = 90°$ or $\phi_S = 104°$ combined with the rudder contribution, good levels of yaw control were provided for the entire angle-of-attack range tested. The side force data and yawing moment data were always the same sign, indicating that the net force was coming from the forebody. The rolling moment data show that, in general, small amounts of proverse roll existed.

Figure 19 shows cross-flow sketches at $\alpha = 50°$ for the strake-off configuration and the .3 long ogive strake at radial locations of $\phi_S = 54°$, $90°$, and $104°$. These cross-flow sketches are not intended to be exact but rather to qualitatively present the relative positions of the forebody vortices. For the baseline strake-off configuration, the flow on both sides of the forebody separated at the chine as expected, and a naturally occurring asymmetry was present. The right-side vortex stayed close to the forebody upper surface while the left-side vortex remained farther away from the forebody surface. This resulted in the net force to the right that caused the positive yawing moments seen in the static data (fig. 18).

With a .3 long ogive strake at the $\phi_S = 54°$ location, the right-side upper-surface vortex was affected by the vortex formed off the strake and remained close to the forebody upper surface. The net force was to the right as seen in the static data. The laser light sheet was not able to illuminate the underside of the forebody so the vortex formed off of the strake could not be seen and thus does not appear in figure 19. At the $\phi_S = 90°$ location, the .3 long ogive strake pushed the right-side flow away from the surface of the forebody, allowing the left-side vortex to remain close to the forebody upper surface. Thus, the yawing moment coefficients were negative because of the net force to the left. For the same strake at $\phi_S = 104°$, the flow visualization looked very similar to the flow visualization for the $\phi_S = 90°$ location in that the right-side vortex was pushed away from the forebody surface. Because of the higher positioning of the strake

at $\phi_S = 104°$, the right-side vortex appeared to be pushed farther away from the forebody than with the strake at $\phi_S = 90°$. This allowed the left-side vortex to increase the area over which the vortex had influence. These effects combined to create a greater net force to the left than the $\phi_S = 90°$ location.

Figures 20–22 present the lateral-directional characteristics for the .3 long ogive strake and compare the right- and left-side placement of strakes at $\phi_S = 54°$, $90°$, and $104°$, respectively. These data show that the lateral-directional characteristics were nearly symmetric about the x-axis, indicating that equal control was produced by the right- and left-side strakes. These data indicate the strake did not merely shift the natural asymmetry but created a completely new flow field that had a forced asymmetry caused by the presence of the strake. The forced asymmetry resulted in a change in the cross-flow circulation around the forebody which changed the pressure distribution and the forces and moments. For this reason, all of the strake effectiveness force and moment plots show the total forces and moments measured and are not presented as a difference from the strake-off data.

The static pressure vector plots at $\alpha = 50°$ for the $\phi_S = 104°$ location (fig. 23) illustrate that the pressure distributions were reversed for the strake on the right versus left sides of the forebody. These data support the conclusion that switching the strake side resulted in mirror-imaged flow fields created by a change in the circulation around the forebody.

Figure 24 presents the effectiveness in sideslip at $\alpha = 50°$ for the baseline configuration and for the .3 long ogive strake at locations of $\phi_S = 54°$, $90°$, and $104°$. The baseline strake-off configuration data show the natural asymmetry that occurred at $\beta = 0°$ and the nonlinearity of the data with sideslip. With a strake at $\phi_S = 90°$ or $104°$, good yawing moment control was maintained for values of sideslip between $-5°$ and $5°$. This indicates that the strakes had some robustness in their ability to maintain effectiveness in nonzero sideslip conditions. This is needed if such strakes are incorporated into an aircraft design. For $\phi_S = 54°$, nonzero sideslip robustness was not as good, as the strake provided nearly no controlling moment at $\beta = -5°$.

Figure 25 presents the longitudinal characteristics for these strake locations. These data show that the strake at $\phi_S = 90°$ had the largest value of pitch-up due to the added planform area with $\phi_S = 104°$ having the second largest pitch-up. For $\phi_S = 54°$, the data for angles of attack less than $\alpha = 35°$ show pitching moment values nearly equal to the baseline. At angles of attack between about $\alpha = 42°$ and $\alpha = 60°$, the strake provided an increment of nose-down pitching moment probably because of a trapped vortex between the strake and chine.

The lift curve data showed that the strake at $\phi_S = 90°$ increased $C_{L,\text{max}}$ with a combination of increased planform area and vortex lift produced by the strake. For $\phi_S = 104°$, $C_{L,\text{max}}$ was approximately the same as with the strake off but occurred at $\alpha = 45°$ instead of $\alpha = 40°$. $C_{L,\text{max}}$ was decreased for $\phi_S = 54°$ because of the vortex trapped on the lower surface.

Modulation methods. Several strake deployment methods were investigated to find a control modulation scheme that would produce linearly increasing control forces as the strake was deployed. One method used successfully in references 3–6 was strake deflections, which represent the folding out of the strake from the forebody surface. For radial locations of $\phi_S = 90°$ and 104°, strake deflections were tested as a means of modulation (fig. 12). To obtain the most desirable modulation, the strake deflections have to produce linear increments in yawing moment between the fully retracted case (strake off) and the fully deployed case ($\delta_S = 0°$). However, this is not necessary if a nonlinear control scheme is employed.

Figures 26 and 27 show the results of using strake deflections at $\phi_S = 90°$ and 104°, respectively. At the $\phi_S = 90°$ location (fig. 26), the positive deflections (upward) actually increased the effectiveness instead of modulating it, while the negative deflections (downward) showed more potential for actual modulation. The $\delta_S = 60°$ deflection produced a yawing moment that was equivalent to the baseline asymmetry, which indicates that the strake would have to be deflected at least to that location from the undeployed position before any control effectiveness would be gained on this particular configuration. It was believed that the negative deflections worked better than the positive deflections because in the deflected positions, the point of flow separation at the strake edge was located at a point lower and closer to the forebody surface than the undeflected or positive deflection cases. As a result, the flow had a better chance of staying close to the forebody upper surface, which could lead to modulated control. With positive deflections, the flow was kept away from the surface and thus only minimal modulation was achieved.

Figure 27 shows that deflections at $\phi_S = 104°$ had essentially no effect on the yawing moment control. At this location, the flow that separated off the edge of the strake remained away from the forebody surface for all of the deflection angles and did not influence the vortex on the opposite side of the forebody.

Because strake deflections showed poor modulation characteristics, strake rotation in planform was investigated as an alternative deployment method. Long ogive strakes with deployment distances d of 0.5 in., 0.99 in.,

and 1.98 in. were tested separately to simulate rotation of a strake out from the forebody centerline with a center of rotation located at the forebody tip (fig. 9). The data for strake rotation at $\phi_S = 90°$ (fig. 28) show that for angles of attack up to $\alpha = 30°$, linear yawing moment control modulation was achieved, but with increased angle of attack, the modulation became nonlinear. Data for strake rotations at $\phi_S = 104°$ (fig. 29) show that the $d = 0.5$ in. strake had no effect until $\alpha = 30°$, but the $d = 0.99$ in. and 1.98 in. strakes had somewhat linear increments up to $\alpha = 35°$. Overall, long ogive strake rotation proved moderately successful for limited angle-of-attack ranges.

Cropped Strake Results

Effect of size and location. All cropped strake testing was done with the full configuration. Cropped strakes with values of $C_R/R_B = .6$ and $.3$ were tested in the middle and aft positions, and figure 7 shows sketches of these strakes.

Radial locations of $\phi_S = 90°$ and 104° were tested for selected cropped strake configurations. However, because the $\phi_S = 104°$ location proved more effective, only those results are presented. Figure 30 shows the lateral-directional characteristics of the cropped strakes tested at $\phi_S = 104°$. These data show that the cropped strakes in the middle position were the most effective, with the .6 cropped strake producing the largest asymmetry. The .6 cropped strake was more effective because its larger width was able to push the vortex farther away from the forebody surface than the .3 cropped strake. The middle position proved more effective than the aft position for both the .3 and .6 cropped strakes. With the strake located closer to the front of the forebody, the flow was influenced farther upstream so that the resultant flow field had more of the forebody surface to act upon. Additionally, the increased moment arm of that surface contributed to increasing the resultant yawing moment.

It should be noted that when the strakes were tested in the aft position, the naturally occurring asymmetry of the forebody had more influence over the resulting flow field. Thus, when the strakes were located aft on the forebody, the strake effectiveness was determined by the difference between the strake-on and the strake-off yawing moments. For this reason, it was decided the .3 cropped strake in the aft position was ineffective because the yawing moment was nearly equal to the strake-off case.

Figure 31 shows cross-flow sketches at $\alpha = 50°$ for the .3 and .6 cropped strakes in the middle position at $\phi_S = 104°$. These strakes produced similar results to the .3 long ogive strake because they pushed the right-side vortex away from the forebody surface. The right-side

vortex appeared somewhat closer to the body with the .3 cropped strake because of the smaller width of the strake, and the left-side vortex appeared to be located at a slightly lower point on the upper surface.

Figure 32 shows the effects of sideslip on the lateral-directional characteristics of the cropped strakes in the middle position for $\alpha = 50°$. All three configurations produced similar yawing moment characteristics for values of sideslip less than $-5°$, which leads to the conclusion that the strakes were not effective. However, for $\beta > -5°$, both strakes were effective, with the .6 cropped strake being more effective. The .6 cropped strake produced a relatively constant moment between sideslip values of $-5°$ and $5°$, indicating robustness so that slight sideslip excursions would not adversely affect the yaw control. However, the .3 cropped strake did not maintain a constant level of effectiveness for nonzero sideslip values and would be more sensitive to sideslip excursions.

Modulation methods. Modulation of the cropped strakes was attempted by deflecting the strakes mounted at $\phi_S = 104°$. Consistent with previous data, the results were considered poor and thus are not presented here. However, lateral translation was tested to evaluate the modulation characteristics using a series of cropped strakes. This concept is illustrated in figure 10. Lateral translation data (fig. 33) show that only a small amount of modulation was produced by the first translation to $y = 0.49$ in. from the strake-off, nondeployed position, but larger increments occurred for $y = 0.99$ in. and 1.32 in. For $y = 1.65$ in. and 1.98 in. only small increments were achieved. Lateral translation could possibly be used as a modulation method, but a nonlinear control scheme would have to be employed.

Short Ogive Strake Results

Effect of position. All short ogive strake testing was done with the full configuration. A short ogive strake with a value of $C_R/R_B = .3$ was tested in the front, middle, and aft position (fig. 6). Because the $\phi_S = 104°$ location produced the best results for the .3 long ogive strake, only the results for that radial location are presented for the short ogive strakes.

Figure 34 compares axial position for the .3 short ogive strake at a radial location of $\phi_S = 104°$. With the strake in the front position, a large asymmetry was produced, but with the strake in either the middle or aft position, essentially no control moment was produced by the strake when compared to the strake-off data. This result differs from the .3 cropped strake testing results which showed some amount of effectiveness in the middle position (fig. 30). Even though the two strakes had the same length and C_R/R_B value, the cropped strake forced the

vortex away from the fuselage more quickly than the short ogive strake. With the flow closer to the surface over more area on the strake side for the short ogive strake, the asymmetry was reduced.

Figure 35 presents a comparison of the data for the .3 short ogive strake in the front position to the data for the .3 long ogive strake. These data show that the yawing moment asymmetries were equal up to $\alpha = 45°$, but that the maximum magnitude for the .3 short ogive strake was slightly less than that for the .3 long ogive strake. This result led to the conclusion that the length of the strake had only minor effects, and it was the proximity of the strake to the front of the forebody that created the large asymmetric moments. This also led to the belief that the .3 short ogive strake could be made shorter in length without much loss in the asymmetric yawing moment. With this in mind, shorter length derivative strakes based on the .3 short ogive strake were tested, and the results will be presented in the Strake Size Minimization Results subsection of this report.

Figure 36 shows the pressure vector plot for the .3 short ogive strake at $\phi_S = 104°$ in the front position for $\alpha = 50°$. Compared to the pressure vector plot for the .3 long ogive strake at $\phi_S = 104°$ (fig. 23(a)) only slight differences were noted. Because the .3 short ogive strake ended where the pressure port ring was located, no flow-field characteristics aft of the strake were measured. Thus, differences in the pressure distribution between the .3 long ogive strake and the .3 short ogive strake aft of this point could not be measured.

Figure 37 shows the cross-flow sketch at $\alpha = 50°$ for the .3 short ogive strake in the front position at $\phi_S = 104°$. Like other strake shapes, the flow was pushed away from the forebody by the strake on the right side while the vortex on the left side remained close to the forebody upper surface. However, the flow field aft of the strake included a third vortex that formed along the chine line. This vortex remained small and was low on the upper surface and did not affect the left-side flow. The yawing moment data for the .3 short ogive strake in the front position and for the .3 long ogive strake are very similar, indicating that this third vortex did not have a large influence.

Figure 38 is a photograph showing the same strake configuration shown in figure 37. The camera was pointed downstream looking up at the forebody at an angle of about 10°, and the laser light sheet was positioned aft of the strake. The flow is seen being pushed away from the forebody by the strake. The third, smaller vortex is also visible on the strake side of the forebody (left side of photograph).

7

Figure 39 shows good effectiveness in sideslip for the .3 short ogive strake and shows the same trend that was seen in figure 24 for the .3 long ogive strake at $\phi_S = 104°$.

Modulation methods. Deflections were tested for the .3 short ogive strake in the front position and proved ineffective in modulating the control moments, as was expected. Thus, a second modulation scheme, axial translation, was attempted. This involved moving the .3 short ogive strake to increase distances back from the forebody tip (fig. 11(b)).

Figure 40 shows the results of axial translation, where x is the distance between the forebody tip and the strake tip measured along the forebody centerline. For angles of attack greater than $\alpha = 15°$ a fairly linear increment was achieved between the different axial positions except for the axial position of $x = 0$ in. for $\alpha > 50°$.

Figure 41 shows the values of the yawing moment coefficients achieved at $\alpha = 50°$ for axial locations between $x = 0$ in. and $x = 3$ in., and the data show a nearly linear change as a function of the location. Based on the data presented in figure 22, it was assumed that a strake on the left side of the forebody would produce equal yawing moment magnitudes of opposite sign as the right-side strake as long as the strake is near the tip of the forebody. As the strake is moved aft on the forebody, the natural asymmetry would probably have a stronger influence. Thus, strakes on the left side may not produce equal yawing moment magnitudes of opposite sign as the right-side strake for strake locations farther aft on the forebody.

Strake Size Minimization Results

Effects of size. As discussed previously, the data for the .3 long ogive strake and the .3 short ogive strake were nearly equivalent. Thus, different lengths of the .3 short ogive strake were tested to determine how small a strake could be while maintaining effectiveness. Figure 6 shows sketches of the 1/2, 1/4, 1/8, and 1/16 length .3 short ogive strakes tested.

The data for these strakes (fig. 42) indicate that for angles of attack between $\alpha = 40°$ and 70°, the lateral-directional characteristics are very similar for the .3 short ogive, 1/2 length .3 short ogive, and the 1/4 length .3 short ogive strakes. For angles of attack less than $\alpha = 40°$, the yawing moment magnitudes decreased with decreasing strake length. This indicates that the high angle-of-attack effectiveness was achieved by affecting the flow at the tip of the forebody while the low angle-of-attack effectiveness was related to the length of the strake.

One possible explanation for this strake length effect is that with the shorter length strakes, a third vortex forms along the chine line aft of the strake on the strake side of the forebody which decreases the low angle-of-attack effectiveness. As the angle of attack increases, the vortices produced by the chine aft of the strake and the strake tend to follow the free-stream flow, and the forebody aerodynamics appear to be dominated more by the tip flow so the length of the strake is less important.

The characteristics of the 1/4 length .3 short ogive strake were studied further because of its effectiveness and small size. If a strake is incorporated into a real aircraft, a small strake would be beneficial because of low weight for its structure and any actuation hardware. Figure 43 shows the lateral-directional data for the 1/4 length .3 short ogive strake at radial locations of $\phi_S = 90°$ and 104°. Very little difference was noted between the two locations, but the $\phi_S = 90°$ location showed a very slight increase in yawing moment.

Figure 44 shows a photograph taken of the flow visualization at $\alpha = 40°$ for the 1/4 length .3 short ogive strake at $\phi_S = 90°$. On the strake side (left side of photograph), the flow separated off the strake edge and remained off the body for the length of the forebody. On the opposite side, the flow remained close to the forebody upper surface which created the net force to the left. A third vortex formed on the right side aft of the strake. At lower angles of attack, this vortex was small, but remained close to the forebody upper surface near the chine line. At higher angles of attack near $\alpha = 50°$, this third vortex appeared to be entrained in the separated flow caused by the strake. This effect was seen in the yawing moment data which showed the 1/4 length .3 short ogive strake to be less effective than the .3 long ogive strake at low angles of attack but equally effective at high angles of attack between $\alpha = 35°$ and 70°.

The 1/4 length .3 short ogive strake was also tested on the left side of the forebody at $\phi_S = 90°$. The data in figure 45 show that the strake on the left side produced near mirror image results as the strake on the right side. This was consistent with the results seen for .3 long ogive strake testing. As previously mentioned, this shows that the naturally occurring asymmetry can be masked and replaced by an asymmetry created by the strakes.

Figure 46 shows the effectiveness in sideslip with the 1/4 length .3 short ogive strake for $\alpha = 50°$. These data show similar trends as the sideslip data for the .3 long ogive strake at $\phi_S = 90°$ (fig. 24) in that sideslip excursions to $\beta = -5°$ or 5° would not result in large yawing moment changes compared to the $\beta = 0°$ yawing moment.

Figure 47 presents the sideslip characteristics for the 1/4 length .3 long ogive strake comparing the right- and left-side placement of strakes at $\phi_S = 90°$. These data show that in sideslip a strake on the left side produced nearly the same force and moment magnitude as a strake on the right side at opposite values of sideslip, indicating that equal control was produced by the right- and left-side strakes. These data reinforce the concept that the strakes did not merely shift the natural asymmetry but created a completely new asymmetry. As mentioned before, for this reason, the force and moment plots presented for strakes placed near the forebody tip show the total forces and moments measured and are not presented as a difference from the strake-off data.

Figure 48 shows the longitudinal data for the 1/4 length .3 short ogive strake at $\phi_S = 90°$. With this strake, $C_{L,\max}$ occurred at a slightly lower angle of attack than the strake-off configuration but produced slightly or no higher levels of pitching moment. Because the .3 long ogive strake at $\phi_S = 90°$ produced a relatively large pitch-up increment (fig. 25), the slight pitching moment increment of the 1/4 length .3 short ogive strake is considered much more desirable. The smaller planform area of the 1/4 length .3 short ogive strake is believed to be responsible for this reduction in pitching moment compared with the .3 long ogive strake.

Modulation methods. Control modulations using deflections and axial translation were tested for the 1/4 length .3 short ogive strake at $\phi_S = 90°$. Deflections generally changed the yawing moment characteristics by slight amounts, but not enough to be considered a good modulation method. This result was consistent with previous attempts to modulate control by means of strake deflections.

The axial translation data (fig. 49) show good modulation characteristics for angles of attack greater than $\alpha = 25°$. Moving the strake away from the forebody tip in small increments resulted in slightly decreased yawing moments. Below $\alpha = 25°$, the strakes showed little effectiveness, so modulation was not important. At approximately $\alpha = 25°$, the rudder authority was diminishing, but by combining the yawing moments produced by the strakes with the yawing moment contribution due to a maximum (30°) rudder deflection (ΔC_n), good yawing moment control was maintained up to high angles of attack.

Figure 50 shows the yawing moment at $\alpha = 50°$ as a function of x, the distance between the forebody tip and the strake tip. The variation in yawing moment was nearly linear as the strake was translated back along the forebody chine, indicating that this kind of deployment method could probably be easily incorporated into a control system.

The results shown in figure 50 are very similar to those shown in figure 41 for the .3 short ogive strake. Like the .3 short ogive strake, the 1/4 length .3 short ogive strake showed a strong correlation between yawing moment control magnitude and proximity to the forebody tip. This supports the conclusion that control over the forebody flow field can be achieved by a strake at the forebody tip that is fairly small in both length and width. If such a strake were to be incorporated into an aircraft design, the small size would save weight and cost compared to a larger strake.

"Micro" Strake Results

Effect of shape. Because the 1/4 length .3 short ogive strake data showed that a relatively small strake placed near the forebody tip can be very effective, the effects of strake planform shape, width, and length were investigated. A set of "micro" strakes was designed specifically for testing near the tip of the forebody slightly back from the forebody tip. Figure 8 shows the shapes and dimensions of these strakes. The nominal placement of these strakes was such that each strake midpoint was 1 in. back from the forebody tip. It was believed that placement slightly aft of the forebody tip may be preferable on a real aircraft configuration because of installation and actuation considerations.

Figures 51 and 52 present the data for the 1/16 and 1/8 length "micro" strakes, respectively, at $\phi_S = 104°$. The most effective 1/16 length "micro" strakes proved to be moderately effective at higher angles of attack, but produced little asymmetric moment at angles of attack below $\alpha = 30°$. The 1/8 length "micro" strakes performed much better (fig. 52), producing large maximum magnitudes and some low angle-of-attack control. For these strakes, a definite correlation existed with the width of the strake and the maximum C_n achieved, with the wider "micro" delta strake having the largest yawing moment.

Modulation methods. Attempts to modulate the control effectiveness of the 1/8 length wide cropped "micro" strake at $\phi_S = 90°$ using deflections showed poor characteristics and were unacceptable. Axial translation testing was also performed using the same strake (fig. 53). The locations tested were 1 in., 2 in., and 3 in. measured from the tip of the forebody to the center of the "micro" strake which resulted in distances of 0.44 in., 1.44 in., and 2.44 in., respectively, to the tip of the strake. The results show potential for good modulation past $\alpha = 20°$ up through about $\alpha = 55°$. Figure 54 shows the range and linearity of control that could be achieved with this strake. In general, the 1/8 length wide cropped "micro" strake showed good characteristics at $\phi_S = 90°$.

Figure 55 summarizes the "micro" strake results, including the 1/4 length .3 short ogive strake. Several of the "micro" strakes were tested at more than one axial location, as was the 1/4 length .3 short ogive strake. Figure 55 shows the maximum yawing moment attained by the strakes as a function of their axial location, measured between the forebody tip and the front of the strake. The maximum yawing moment occurred at either $\alpha = 45°$ or $50°$ for all cases and was either at a radial location of $\phi_S = 90°$ or $104°$. The data in most cases were nearly identical for either radial location in the instances where the strake was tested at both locations.

The data clearly indicate that the farther away from the tip the strake was placed, the less effective the strake was. This result was seen with other strake shapes. The lines drawn between the points in figure 55 are lines of equal maximum strake widths. With the exception of the line for a width of .19 in. and .28 in., a trend was established. The data trend indicated that for an equal distance aft of the forebody tip, a larger width increased the effectiveness of the strake.

Figure 55 can be used as a preliminary design chart by choosing a desired value for $C_{n,max}$; then based on how far forward the strake is placed, a strake width can be estimated. This chart allows a user to do a trade-off study on strake size and position. The numbers on this chart are directly applicable only to this particular forebody cross-section shape or one that is very similar. However, this kind of chart can be produced for any given forebody design and can be a valuable design tool for deciding strake size and placement.

Conclusions

A low-speed wind tunnel investigation was conducted in the Langley 12-Foot Low-Speed Tunnel to determine the effectiveness of forebody strakes on a chine forebody to provide yaw control at angles of attack where conventional control surfaces are ineffective. Tests were conducted at a dynamic pressure of 4 lb/ft^2, and data were acquired over an angle-of-attack range of $0°$ to $70°$ and over an angle-of-sideslip range of $-20°$ to $20°$. Previous forebody strake testing was performed with smooth forebodies, and the results indicated that forebody strakes were effective yaw control devices at high angles of attack. The present tests were conducted with a generic fighter aircraft model that incorporated a symmetric $60°$ half-angle chine forebody designed to

have a lower radar cross section than conventional smooth forebodies. The scope of the investigation included investigating the effects of strake size, shape, location, control deployment, and control linearity. The results are summarized as follows:

1. Using a forebody strake on a chine forebody provides significant yaw control capability that, when blended with a rudder contribution, provides high levels of yaw control up to high angles of attack.

2. The radial location of the strakes had a major influence on the magnitude and direction of the control moment produced. Strakes placed on the lower surface of the forebody produced yawing moments toward the strake side of the forebody, while strakes on the chine line and the upper surface produced yawing moments away from the strake side of the forebody. The radial locations shown to give the best results for both low and high angles of attack were along the chine line and just slightly above the chine line.

3. For a given strake shape, the strake length dominated the low angle-of-attack characteristics while the strake axial placement dominated the high angle-of-attack characteristics.

4. Modulation of the yaw control level by strake deflections, with the strake-forebody intersection as the hingeline, was generally either ineffective or nonlinear. However, axial translation of a strake provided a more desirable linear change in the yawing moment.

5. It was shown that a very small strake (1/8 of the forebody length) placed at the forebody tip generated very large yawing moments equal to what was achieved by a strake with a length equal to the forebody length. Axial translation of this small strake provided the levels of control conducive for linear modulation.

6. For very small strakes, a direct correlation between strake width, axial location, and maximum yawing moment coefficient was found for the forebody shape tested. It showed that a strake placed farther aft on the forebody required a greater width to provide a given yawing moment.

References

1. Ball, Robert E.: *The Fundamentals of Aircraft Combat Survivability Analysis and Design*. AIAA, 1985.

2. Nguyen, Luat T.: *Flight Dynamics Research for Highly Agile Aircraft*. SAE Paper 892235, Sept. 1989.

3. Murri, Daniel G.; and Rao, Dhanvada M.: Exploratory Studies of Actuated Forebody Strakes for Yaw Control at High Angles of Attack. AIAA-87-2557, Aug. 1987.

4. Murri, Daniel G.; Biedron, Robert T.; Erickson, Gary E.; Jordan, Frank L., Jr.; and Hoffler, Keith D.: Development of Actuated Forebody Strake Controls for the F-18 High Alpha Research Vehicle. *High-Angle-of-Attack Technology*, Volume I, Joseph R. Chambers, William P. Gilbert, and Luat T. Nguyen, eds., NASA CP-3149, Part I, 1992, pp. 335–380.

5. Murri, Daniel G.; Shah, Guatam H.; DiCarlo, Daniel J.; Lord, Mark T.; and Strickland, Mark E.: Status of Ground and Flight Research on Actuated Forebody Strake Controls. *High-Angle-of-Attack-Technology*, Volume III, Neil W. Matheny, compiler, NASA CP-3137, 1992, pp. 261–282.

6. Murri, Daniel G.; Shah, Guatam H.; DiCarlo, Daniel J.; Lord, Mark T.; and Strickland, Mark E.: Status of Ground and Flight Research on Actuated Forebody Strake Controls. *High-Angle-of-Attack-Technology*, Volume III, Neil W. Matheny, compiler, NASA CP-3137, 1992, pp. 261–282.

7. Murri, Daniel G.; Shah, Gautam H.; DiCarlo, Daniel J.; and Trilling, Todd W.: Actuated Forebody Strake Controls for the F-18 High Alpha Research Vehicle. AIAA-92-3675, Aug. 1993.

8. Malcolm, G. N.; and Skow, A. M.: Enhanced Controllability Through Vortex Manipulation on Fighter Aircraft at High-Angles of Attack. AIAA-86-2277, Aug. 1986.

9. Malcolm, Gerald N.; Ng, T. Terry; Lewis, Liane C.; and Murri, Daniel G.: Development of Non-Conventional Control Methods for High Angle of Attack Flight Using Vortex Manipulation. AIAA-89-2192, July 1989.

10. Malcolm, G. N.; and Ng, T. T.: *Forebody Vortex Manipulation for Aerodynamic Control of Aircraft at High Angles of Attack*. SAE Paper 892220, Sept. 1989.

11. Malcolm, Gerald N.; Ng, T. Terry; Lewis, Liane C.; and Murri, Daniel G.: Development of Non-Conventional Control Methods for High Angle of Attack Flight Using Vortex Manipulation. *Aerodynamics of Combat Aircraft Controls and of Ground Effects*. AGARD CP-465, 1990. (Available from DTIC as AD A223 680.)

12. Ng, T. Terry; and Malcolm, Gerald N.: Aerodynamic Control Using Forebody Strakes. AIAA-91-0618, Jan. 1991.

13. Walchli, Lawrence A.; Guyton, Robert W.; Luria, Frank; and Gillard, William J.: High Angle-of-Attack Control Enhancement on a Forward Swept Wing Aircraft. AIAA-92-4427, 1992.

14. Lanser, Wendy R.; and Meyn, Larry A.: Forebody Flow Control on a Full-Scale F/A-18 Aircraft. AIAA-92-2674, June 1992.

15. Iwanski, Kenneth P.; and O'Rourke, Matthew J.: F-15 Forebody Vortex Flow Control Using Jet Nozzle Blowing. AIAA-95-1800, June 1995.

16. Boalbey, Richard E.; Ely, Wayne; and Hahne, David E.: High-Angle-of-Attack Stability and Control Concepts for Supercruise Fighters. *High-Angle-of-Attack Technology*, Volume I, Joseph R. Chambers, William P. Gilbert, Luat T. Nguyen, eds., NASA CP-3149, Part II, 1992, pp. 759–784.

17. O'Rourke, Matthew J.: Fighter Configuration With a Chined Forebody. AIAA-95-1798, June 1995.

Table I. Forebody Coordinates

Equations for forebody cross section are:

Upper surface: $(Z/r) = -(1.6 - \tan 60°)|(Y/r)|^3 - (\tan 60° - 2.4)(Y/r)^2 - .8$

Lower surface: $(Z/r) = (1.6 - \tan 60°)|(Y/r)|^3 + (\tan 60° - 2.4)(Y/r)^2 + .8$

Y/r	Z/r
0	−0.80000
−.16663	−.78084
−.32489	−.72497
−.46932	−.63923
−.59885	−.53210
−.71490	−.41038
−.81962	−.27858
−.91484	−.13987
−.98044	−.03347
−1.00000	0
−.98044	.03347
−.91484	.13987
−.81962	.27858
−.71490	.41038
−.59885	.53210
−.46932	.63923
−.32489	.72497
−.16663	.78084
0	.80000
.16663	.78084
.32489	.72497
.46932	.63923
.59885	.53210
.71490	.41038
.81962	.27858
.91484	.13987
.98044	.03347
1.00000	0
.98044	−.03347
.91484	−.13987
.81962	−.27858
.71490	−.41038
.59885	−.53210
.46932	−.63923
.32489	−.72497
.16663	−.78084
0	−.80000
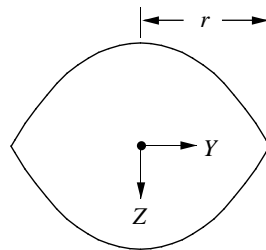
Table II. Pressure Port Coordinates

[Pressure port ring located 9.67 in. aft of forebody tip. Coordinates listed below in inches.]

Y	Z
0	−2.0008
−.4158	−1.9532
−.8107	−1.8141
−1.1711	−1.6007
−1.4943	−1.3340
−1.7839	−1.0310
−2.0452	−.7032
−2.2828	−.3579
−2.4465	−.0932
−2.4465	.0932
−2.2828	.3579
−2.0452	.7032
−1.7839	1.0310
−1.4943	1.3340
−1.1711	1.6007
−.8107	1.8141
−.4158	1.9532
0	2.0008
.4158	1.9532
.8107	1.8141
1.1711	1.6007
1.4943	1.3340
1.7839	1.0310
2.0452	.7032
2.2828	.3579
2.4465	.0932
2.4465	−.0932
2.2828	−.3579
2.0452	−.7032
1.7839	−1.0310
1.4943	−1.3340
1.1711	−1.6007
.8107	−1.8141
.4158	−1.9532
0	−2.0008
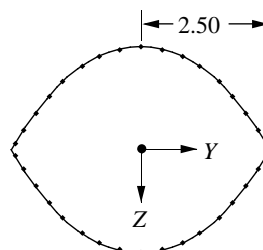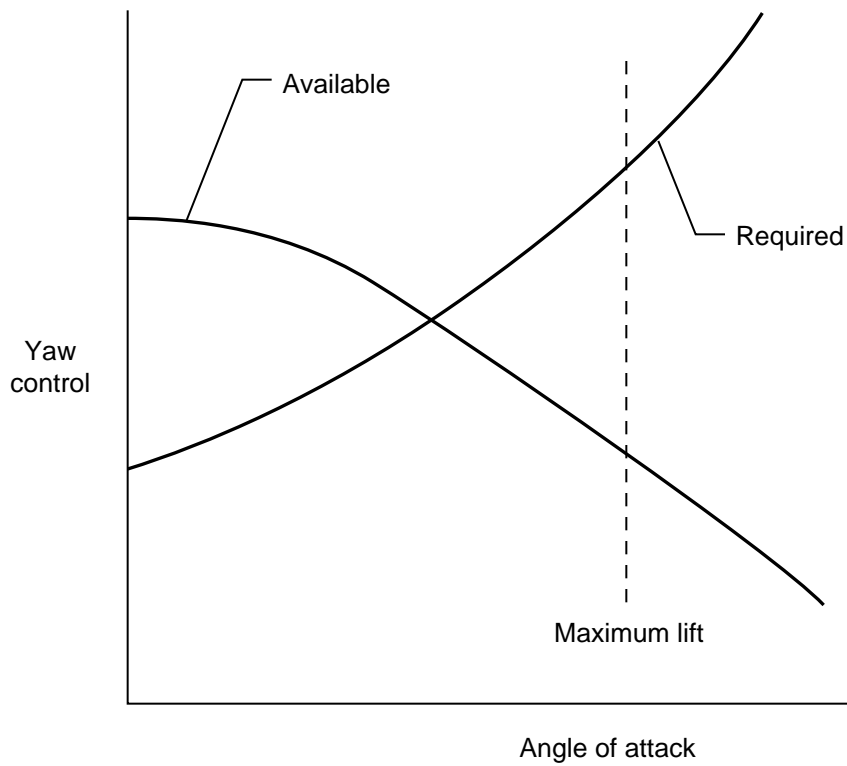
Figure 1. Illustration showing need for increased yaw control at high angles of attack required for coordinating rolling maneuvers.
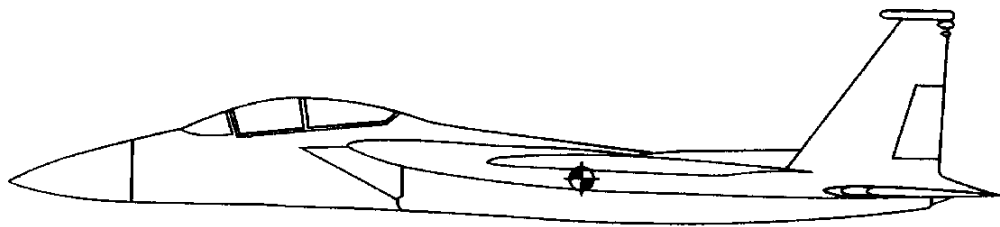
McDonnell Douglas F-15
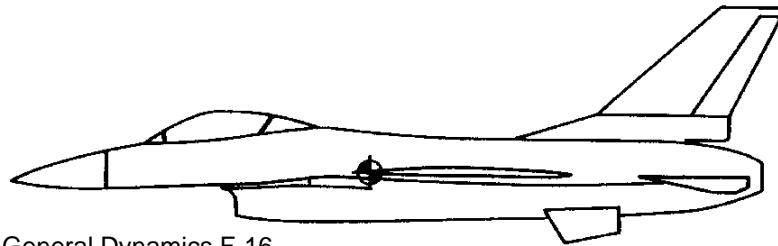
General Dynamics F-16
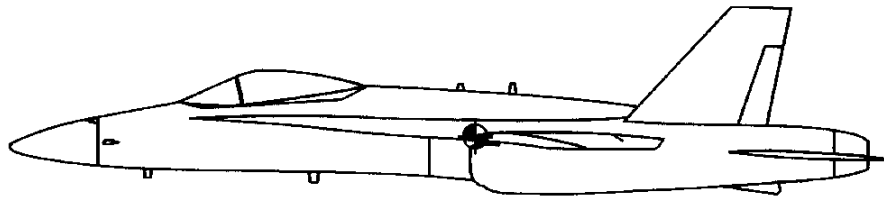
McDonnell Douglas F/A-18
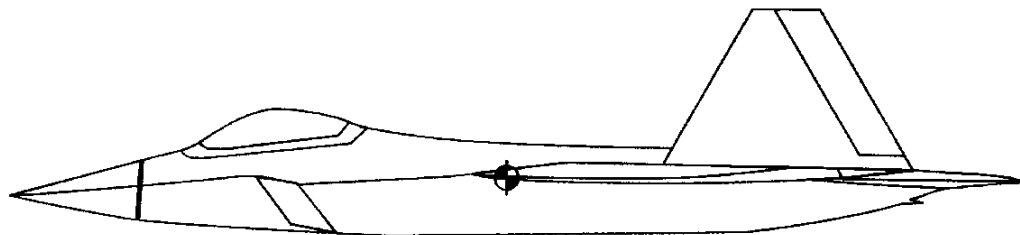
Lockheed YF-22
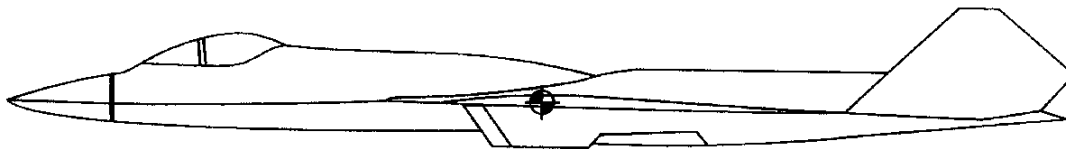
Northrop YF-23

Figure 2. Illustration of forebody moment arm of several modern fighter aircraft.

Pressure port ring

9.67

Section A-A (not to scale)

60°

Y

Z

5.29

6.61

Forebody Pressure port ring

S = 745.60 in^2

b = 40.00 in.

$\bar{c}$ = 21.96 in.

19.34

A   A

5.50

Transition zone

6.00

19.94

25.75

28.53

50.40

16.28

9.64

0.75

5.50

1.58

7.56

45°

5.57

$\bar{c}$

5.00

20°

45°

2.76

20°

2.45

30°   30°

11.13

15.31

30°

40.00
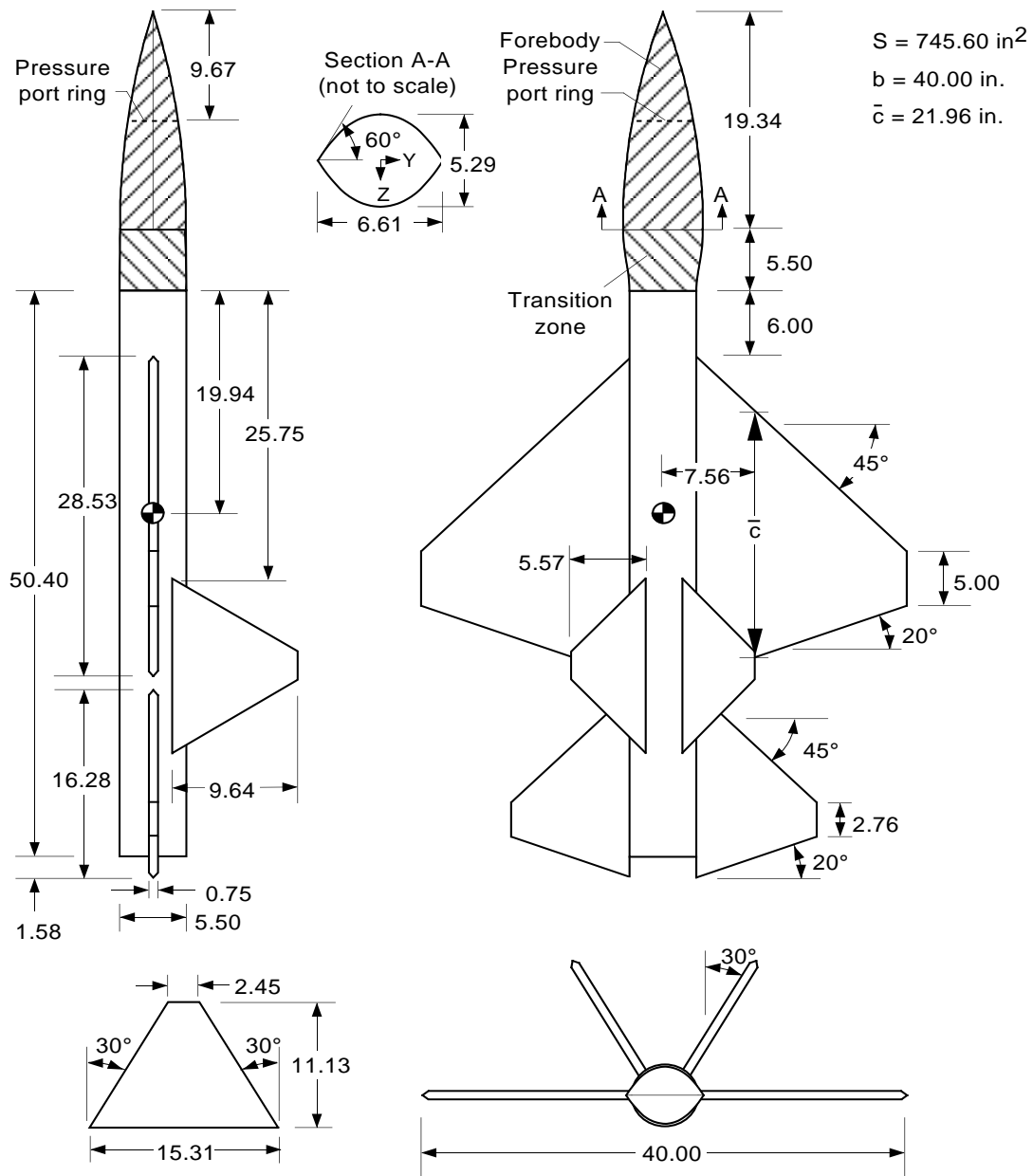
(a) Model dimensions and detail of vertical tail planform geometry. Linear dimensions in inches.

Figure 3. Generic fighter model configuration.

(b) Photo of model in Langley 12-Foot Low-Speed Tunnel.

Figure 3. Concluded.
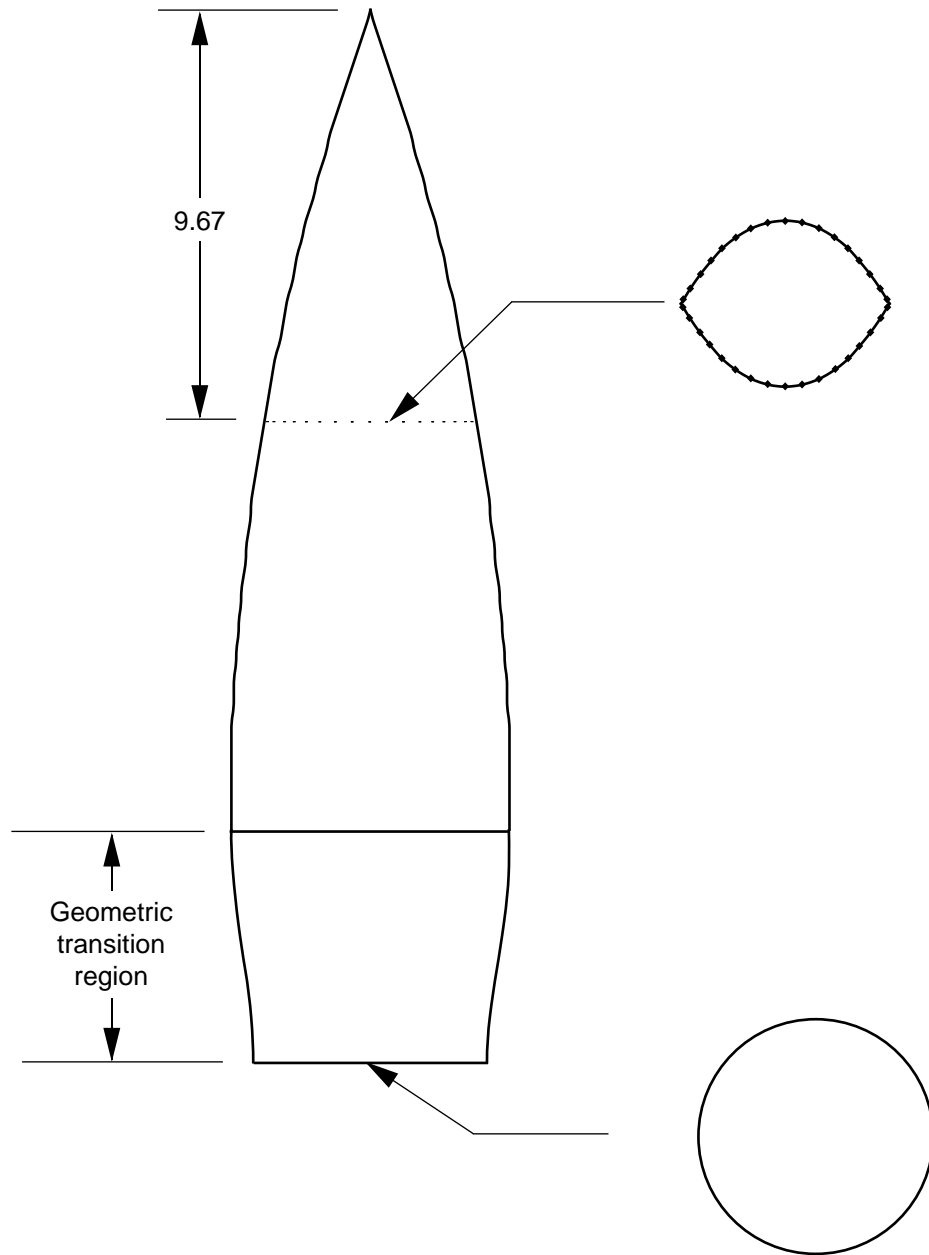
Figure 4. Location of surface static pressure port ring on forebody. Linear dimension in inches.
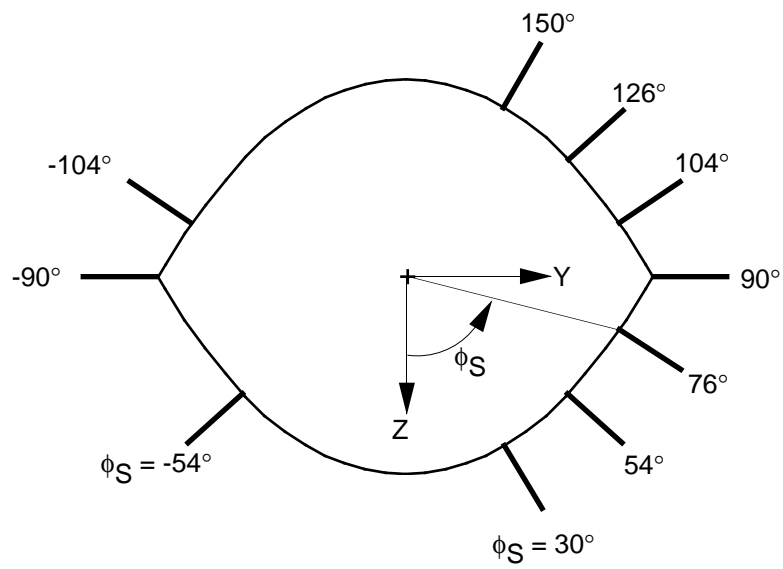
Figure 5. Radial locations tested. View is upstream.

9.67

19.34

Pressure
port ring

$\dfrac{C_R}{R_B} = 0.3$

$R_B = 3.30$

$C_R = 0.99$

.3 long ogive

9.67

0.99

.3 short ogive
Front position

4.83

9.67

.3 short ogive
Middle position

9.67

.3 short ogive
Aft position

4.83

1/2 length
.3 short ogive

2.42

1/4 length
.3 short ogive

1.21

1/8 length
.3 short ogive

0.60

1/16 length
.3 short ogive
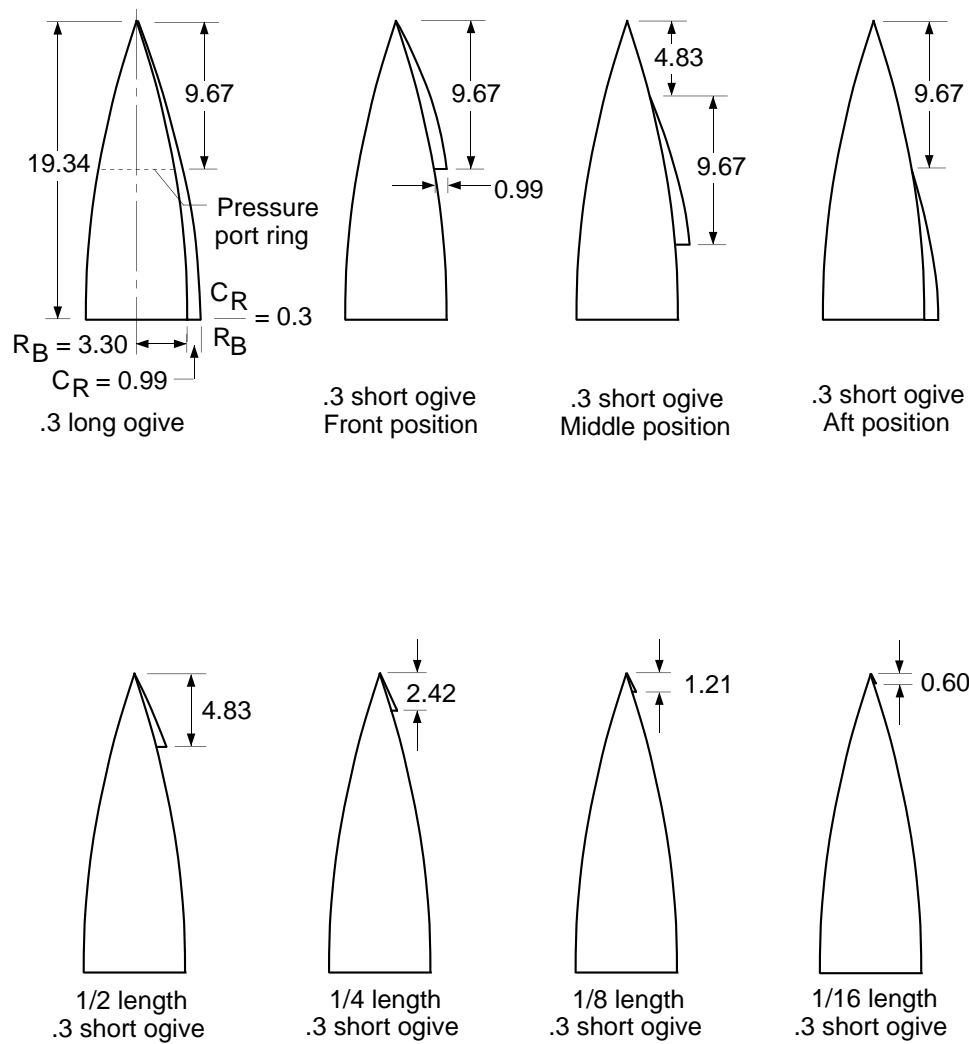
Figure 6. Ogival strake shapes shown at locations tested. Linear dimensions in inches.

$$\frac{C_R}{R_B} = 0.6$$

4.83

9.67

1.98

.6 cropped
Middle position

9.67

45°

45°

.6 cropped
Aft position

$$\frac{C_R}{R_B} = 0.3$$

4.83

9.67

0.99

.3 cropped
Middle position

9.67

45°

45°

.3 cropped
Aft position
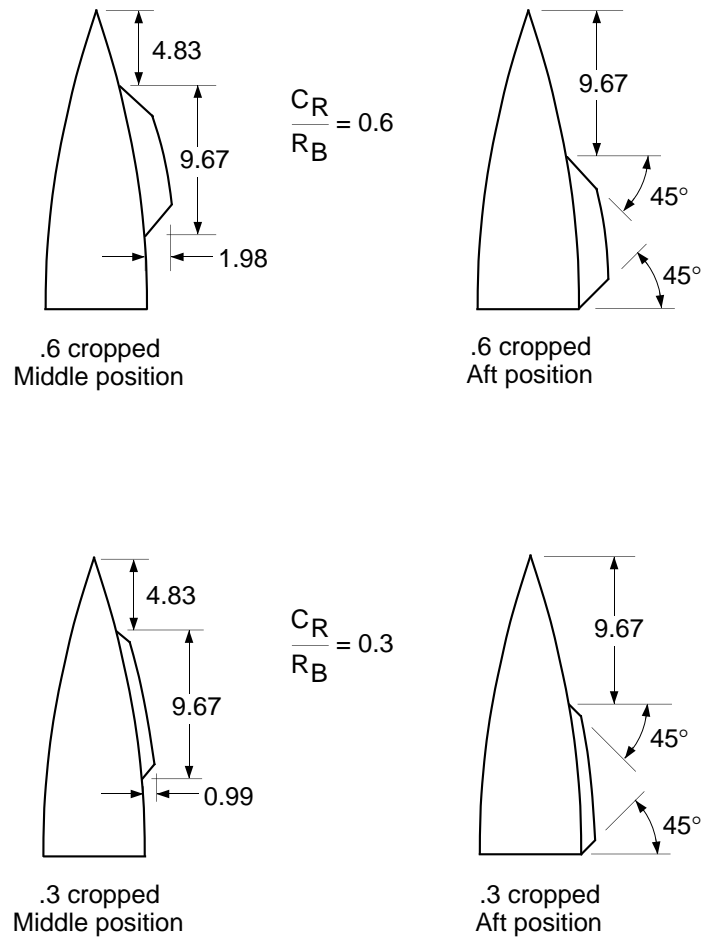
Figure 7. Cropped strake shapes shown at locations tested. Linear dimensions in inches.
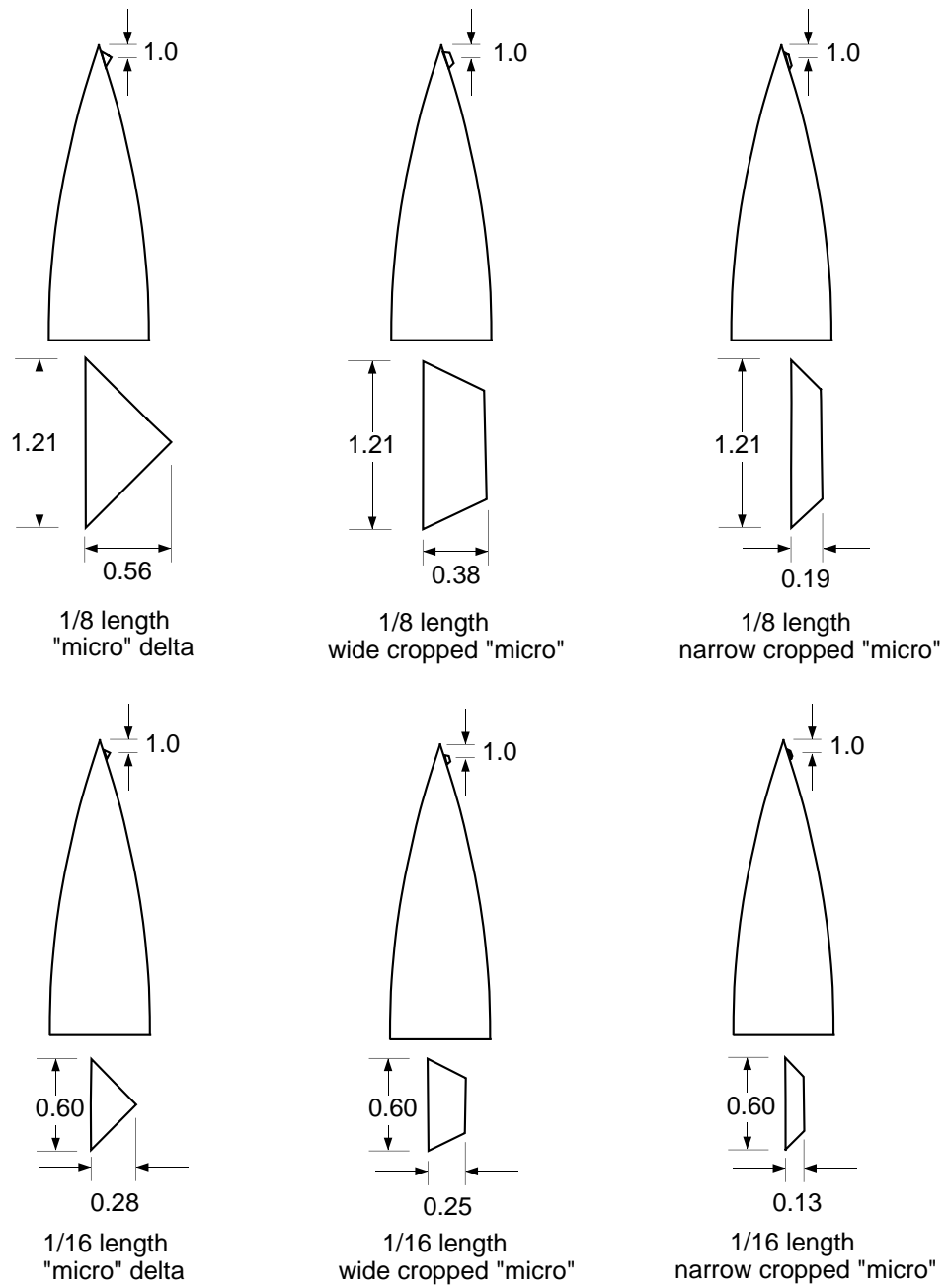
Figure 8. "Micro" strake shapes and dimensions. All were tested with strake midpoint at 1 in. from forebody tip. Linear dimensions in inches.
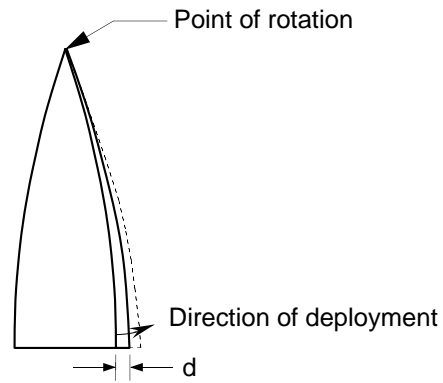
(a) Deployment scheme used for strake rotation and definition of rotation distance, *d*.

d = 0.50   d = 0.99   d = 1.98
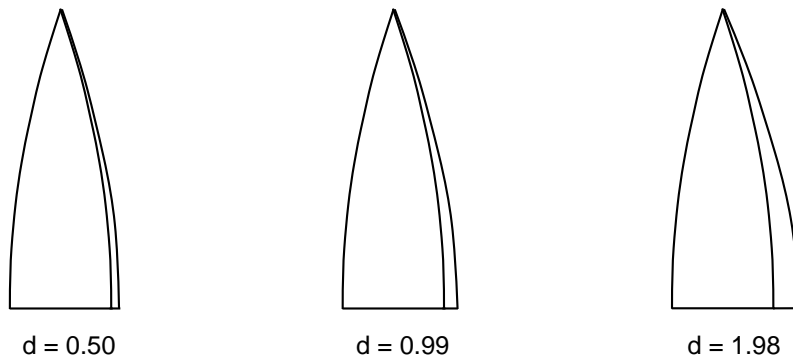
(b) Rotation distances tested.

Figure 9. Strakes tested for rotation of long ogive strakes about forebody tip. Linear dimensions in inches.
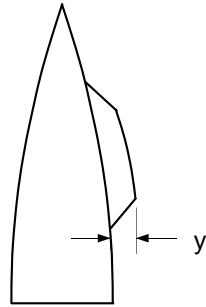
(a) Definition of lateral translation distance, *y*.
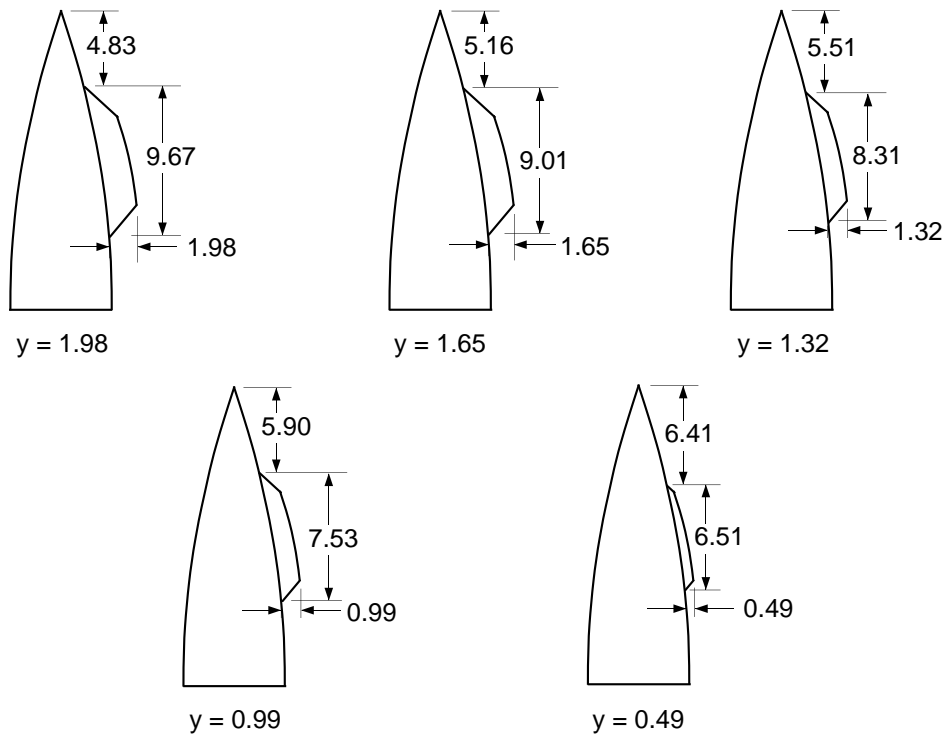
(b) Dimensions of strakes tested for lateral translation.

Figure 10. Strake shapes and locations used for lateral translation of .6 cropped strake in middle position. Linear dimensions in inches.
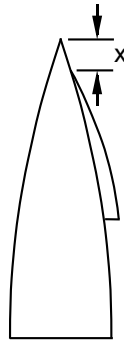
(a) Definition of axial translation distance, x.

x = 0 in.   x = 0.5 in.   x = 1 in.   x = 2 in.   x = 3 in.
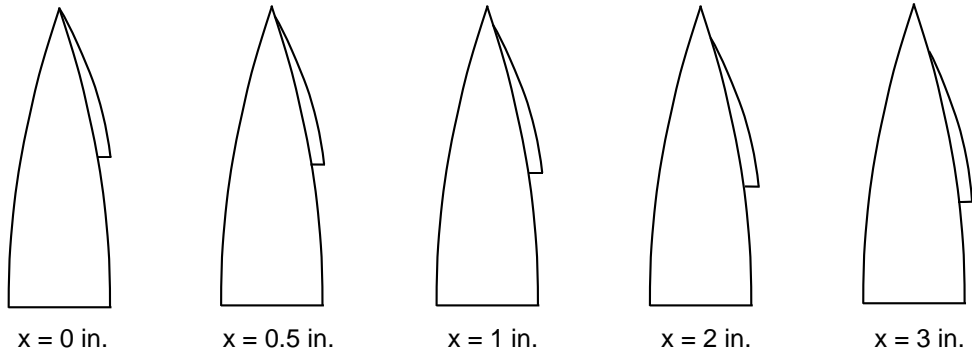
(b) Axial translation distances tested for .3 short ogive strake.

x = 0 in.   x = 0.5 in.   x = 1 in.   x = 2 in.
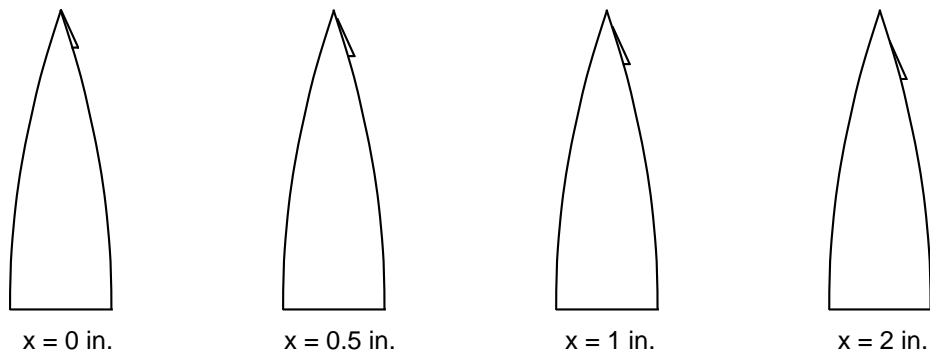
(c) Axial translation distances tested for 1/4 length .3 short ogive strake.

Figure 11. Positions of .3 short ogive and 1/4 length .3 short ogive strakes for axial translation tests.
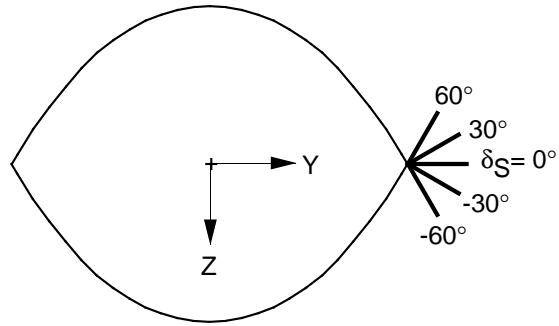
(a) $\phi_S = 90°$.
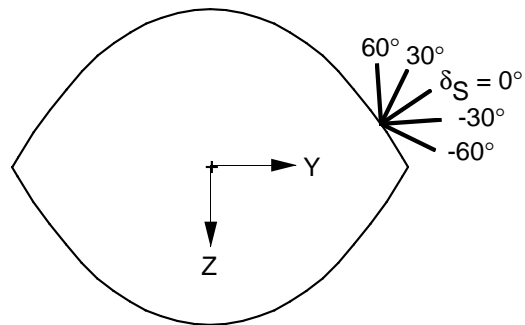
(b) $\phi_S = 104°$.

Figure 12. Definition of strake deflection angles. View is upstream.
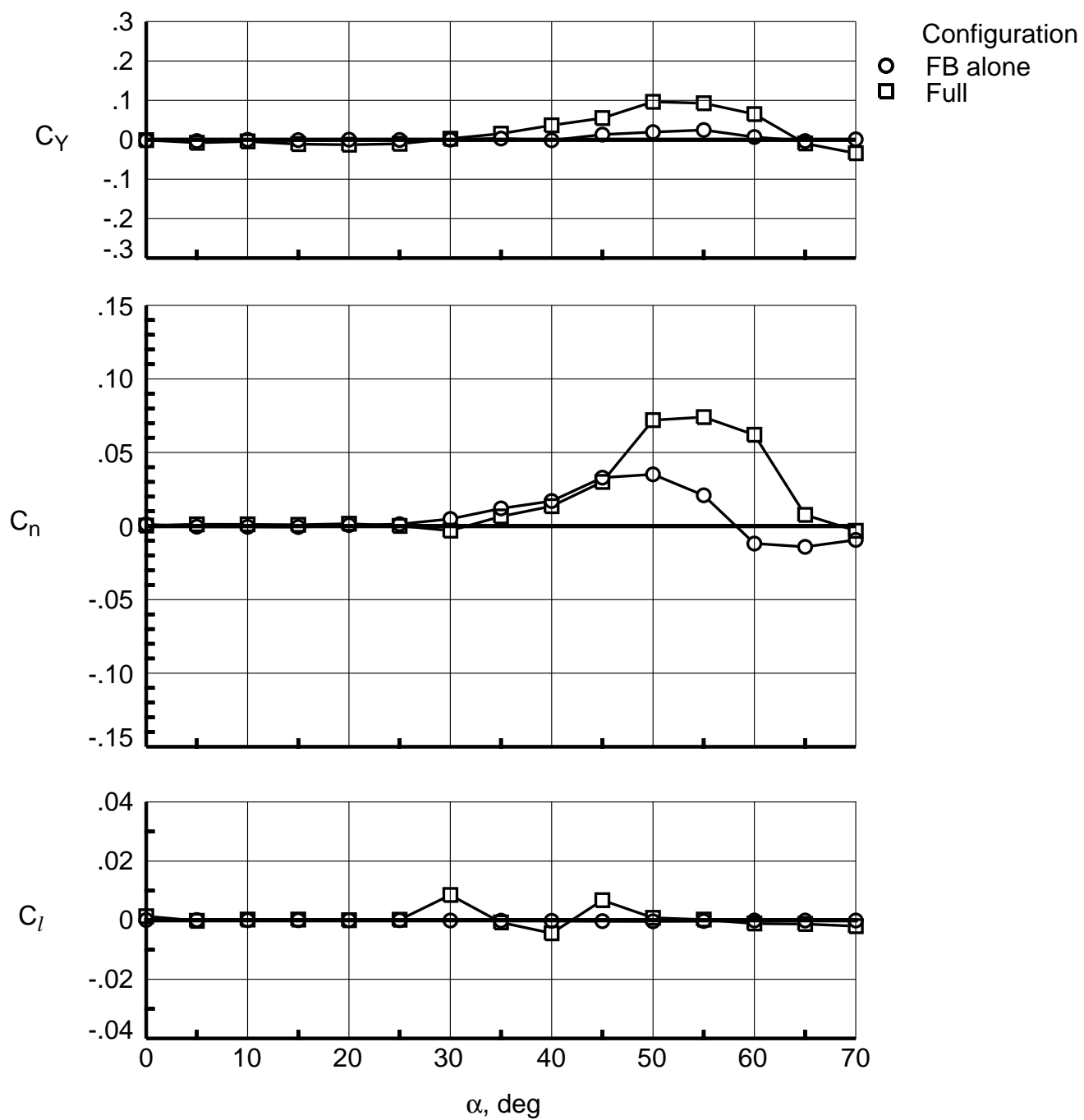
Figure 13. Comparison of forebody (FB) alone configuration with full configuration.
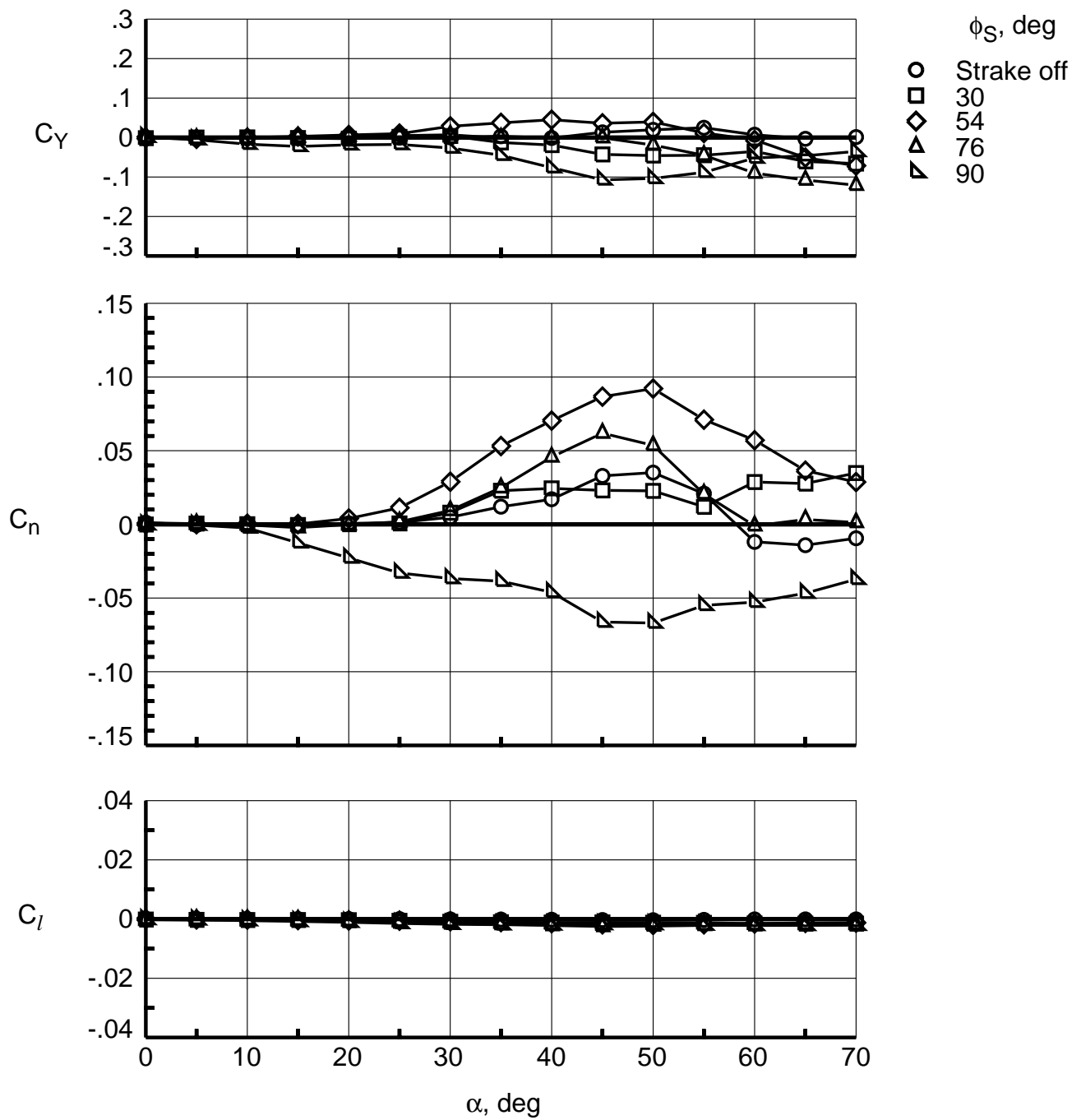
Figure 14. Effect of lower surface strake radial locations on lateral-directional characteristics using .3 long ogive strake with forebody alone.
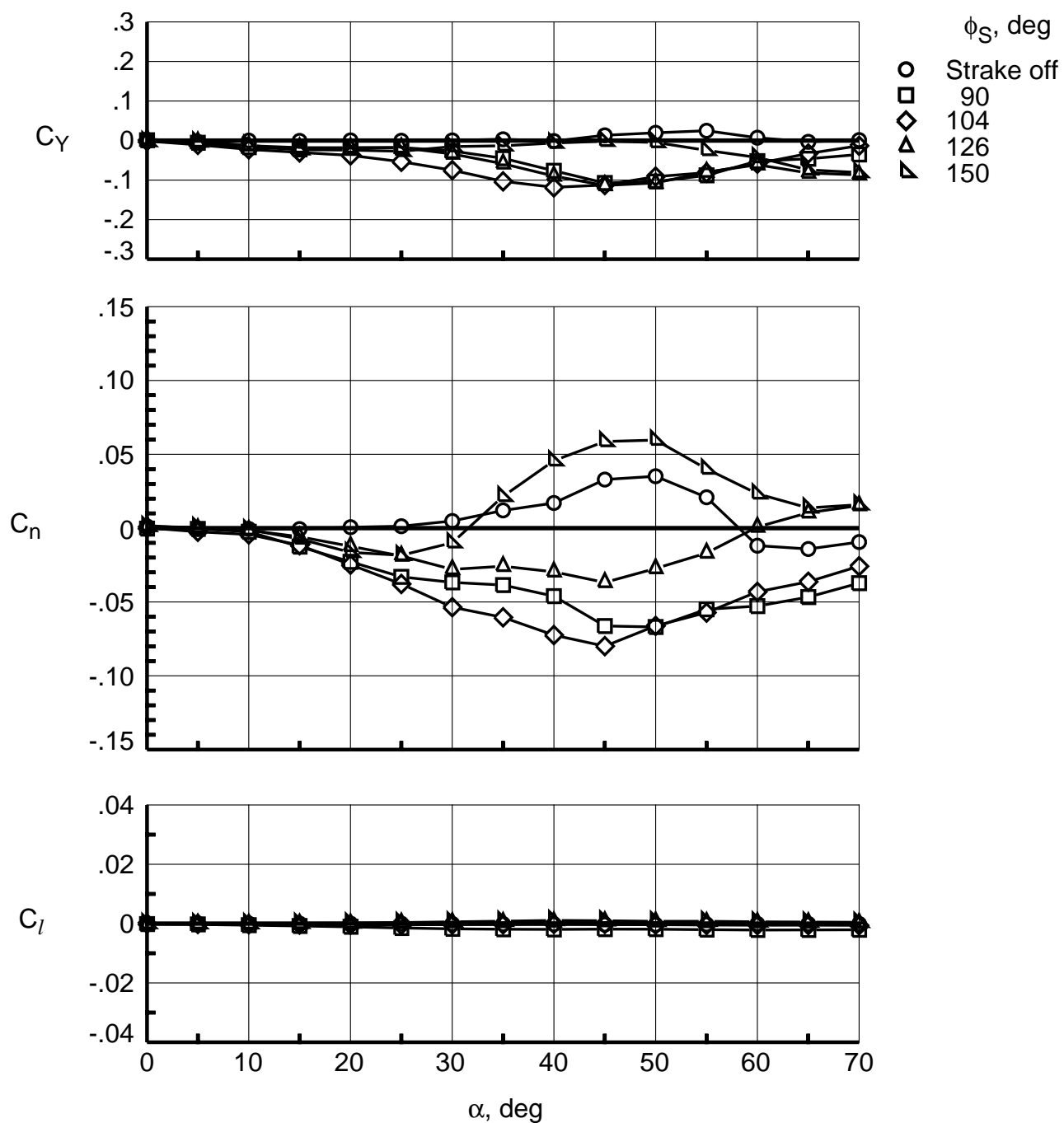
Figure 15. Effect of upper surface strake radial locations on lateral-directional characteristics using .3 long ogive strake with forebody alone.

(a) Strake off.

(b) $\phi_S = 54°$.

(c) $\phi_S = 90°$.

(d) $\phi_S = 104°$.
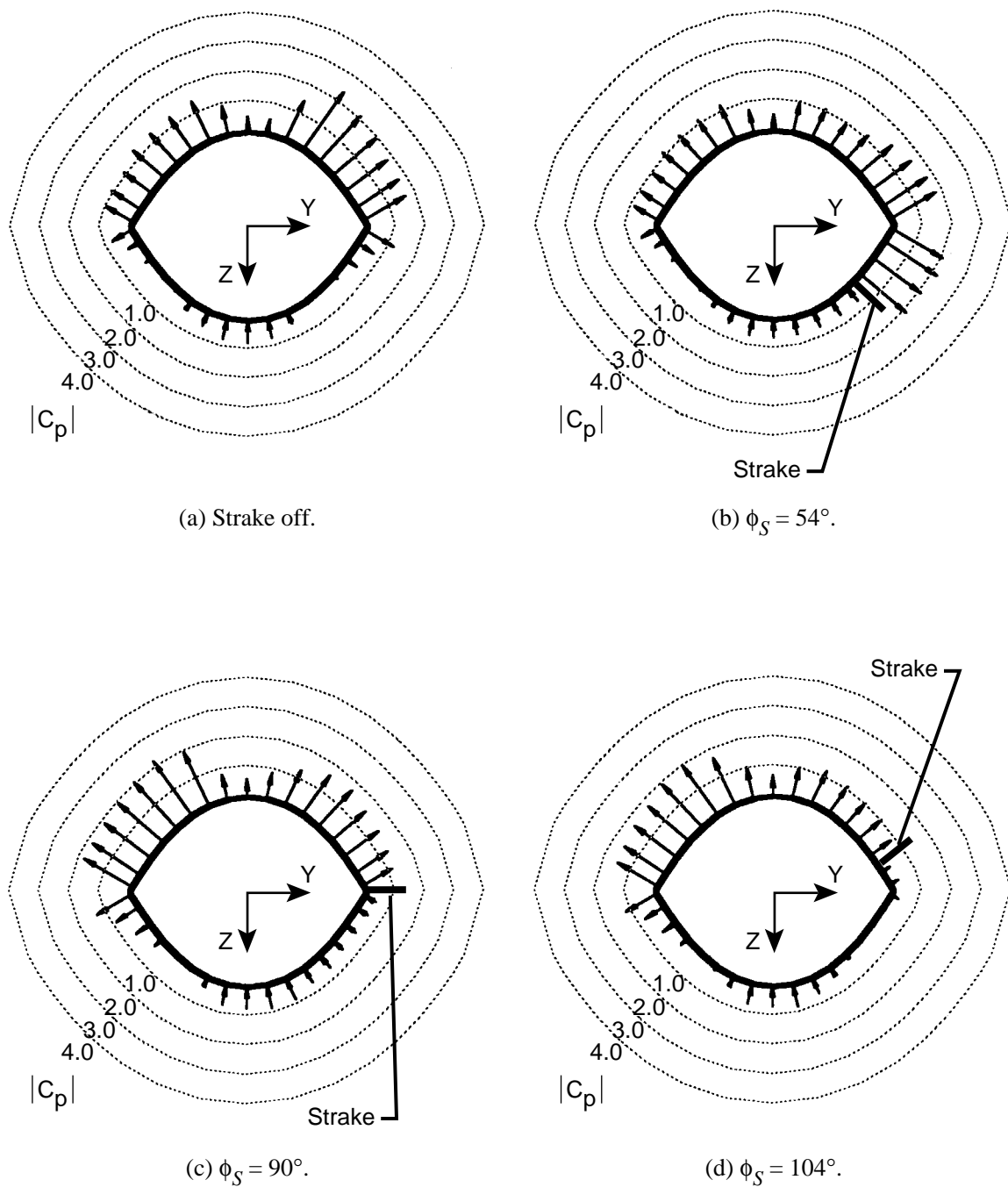
Figure 16. Effect of radial strake location on pressure distribution at $\alpha = 50^\infty$ with .3 long ogive strake with forebody alone. View is upstream. Arrows leading into cross section indicate compression and arrows leading out of cross section indicate suction.
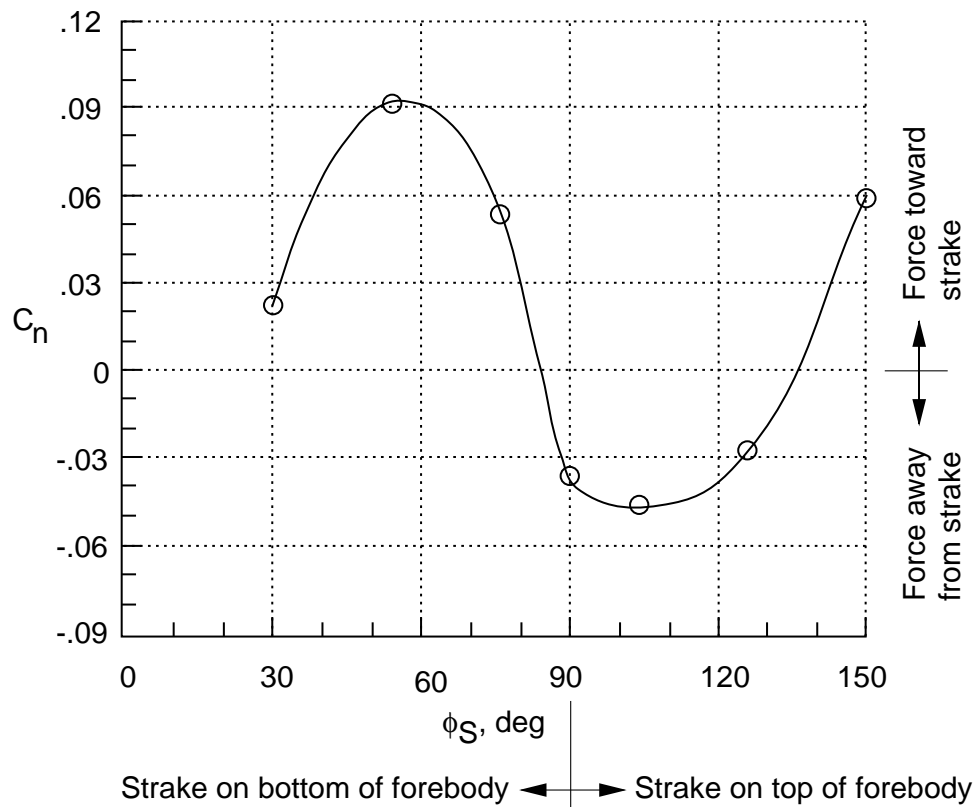
Figure 17. Effect of strake radial location on yawing moment coefficient at $\alpha = 50°$ with .3 long ogive strake with fore-body alone.
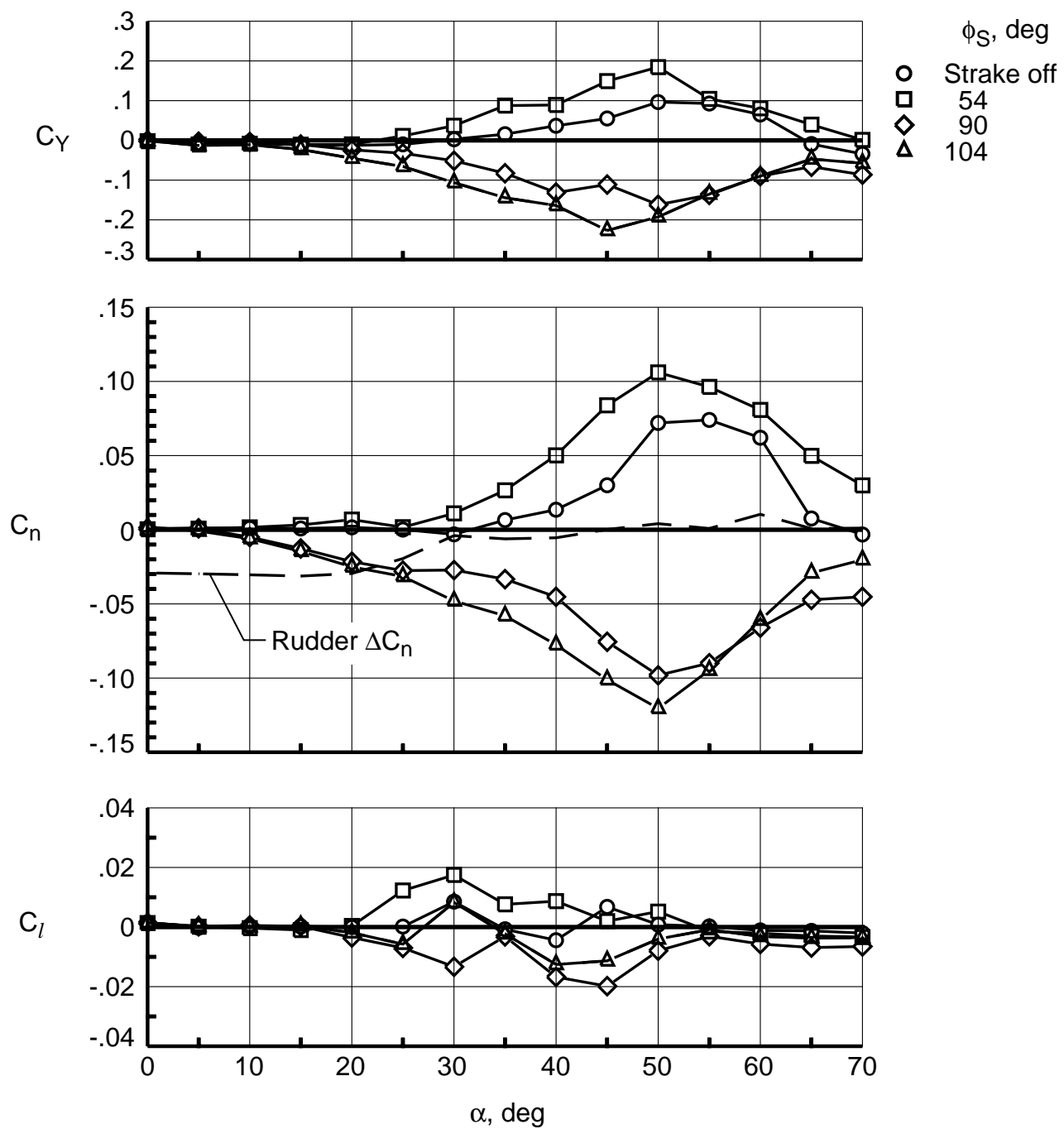
Figure 18. Effect of strake radial location on lateral-directional characteristics with .3 long ogive strake with full configuration.
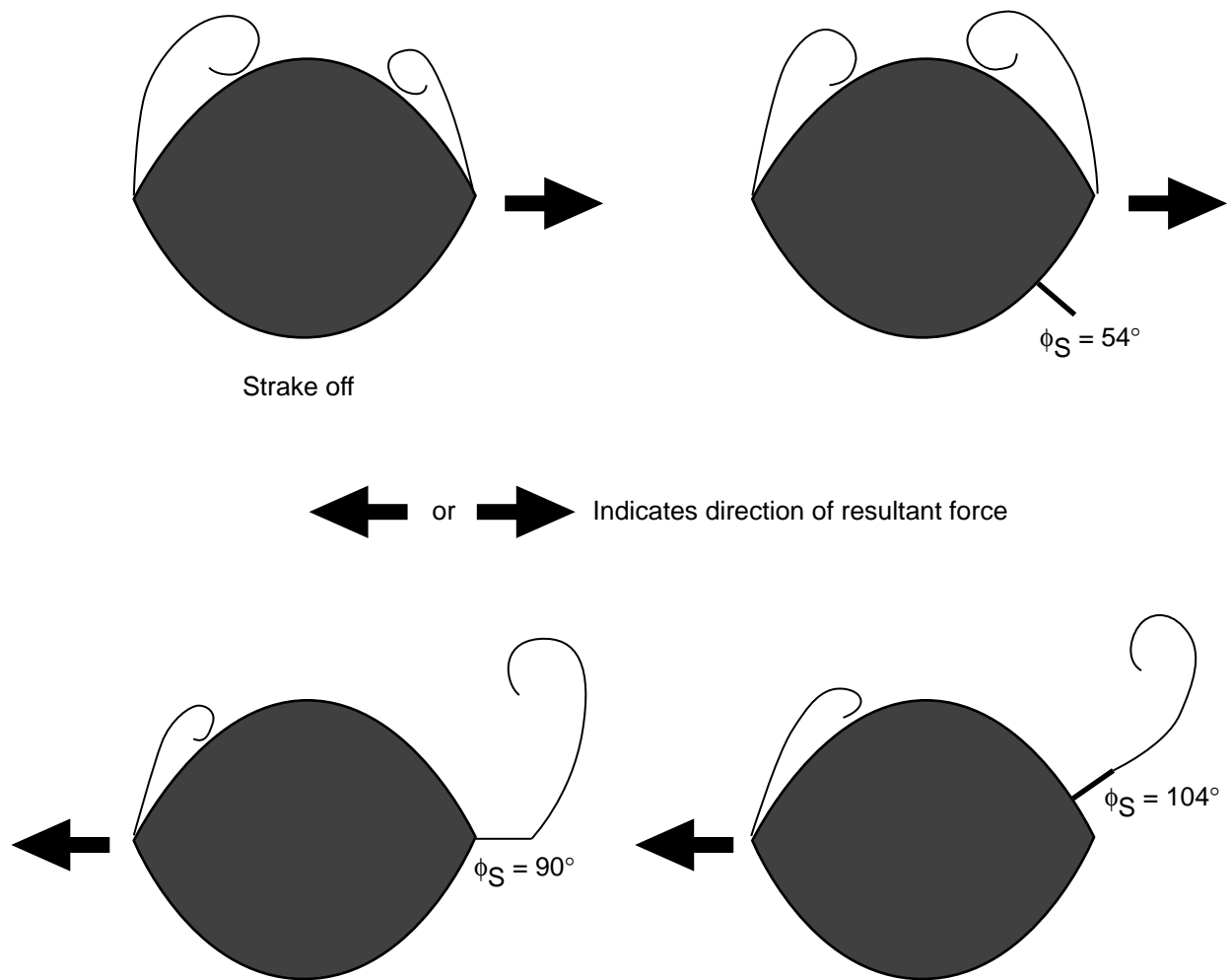
Figure 19. Cross-flow sketches at $\alpha = 50°$ for baseline and .3 long ogive strake at $\phi_S = 54°$, 90°, and 104° with full configuration. Sketches based on flow visualization. View is upstream.

Strake off

or   Indicates direction of resultant force

$\phi_S = 54°$

$\phi_S = 90°$

$\phi_S = 104°$
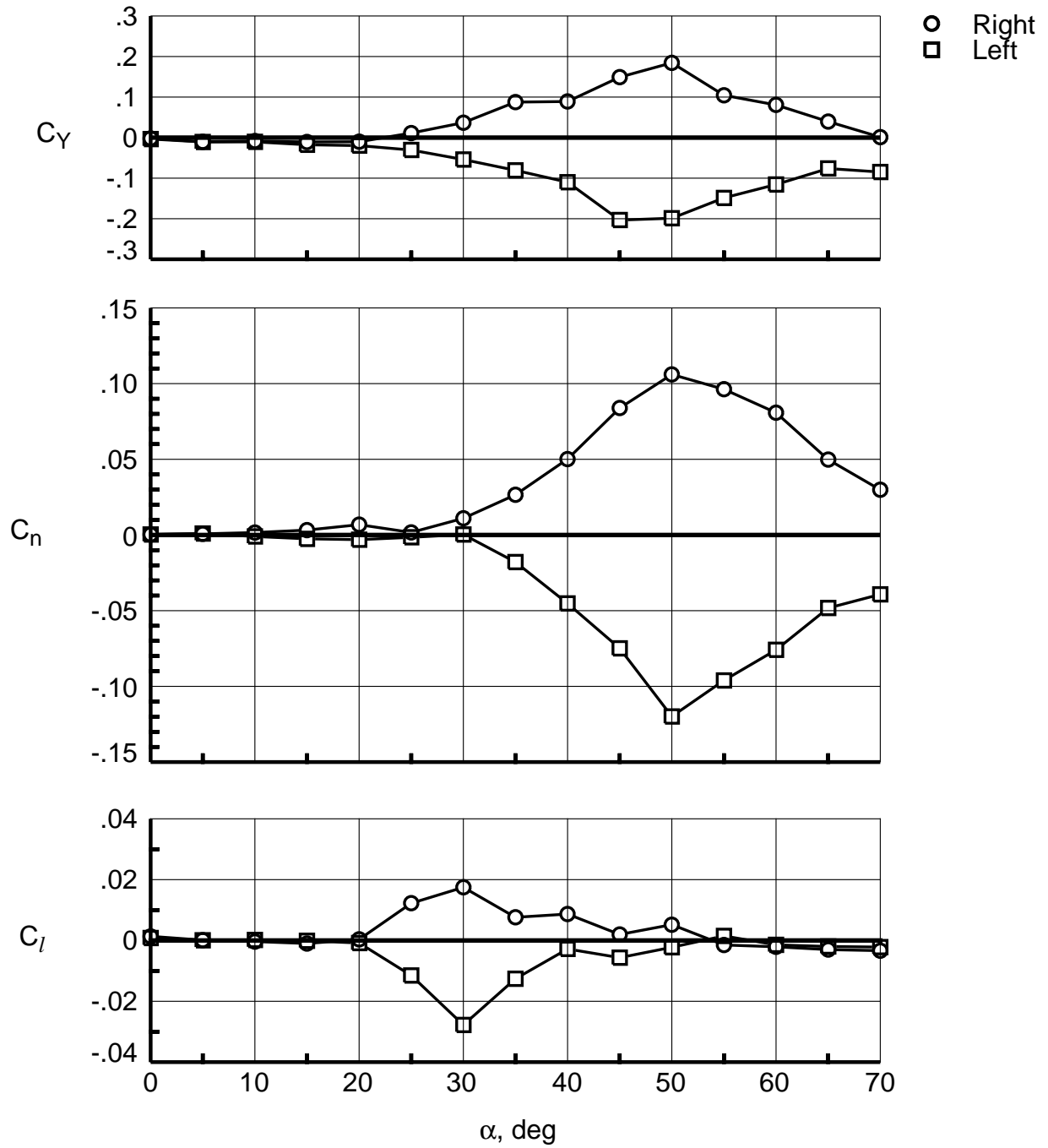
Figure 20. Effect of strake being placed on right or left side of forebody with .3 long ogive strake at $\phi_S = 54°$ with full configuration.
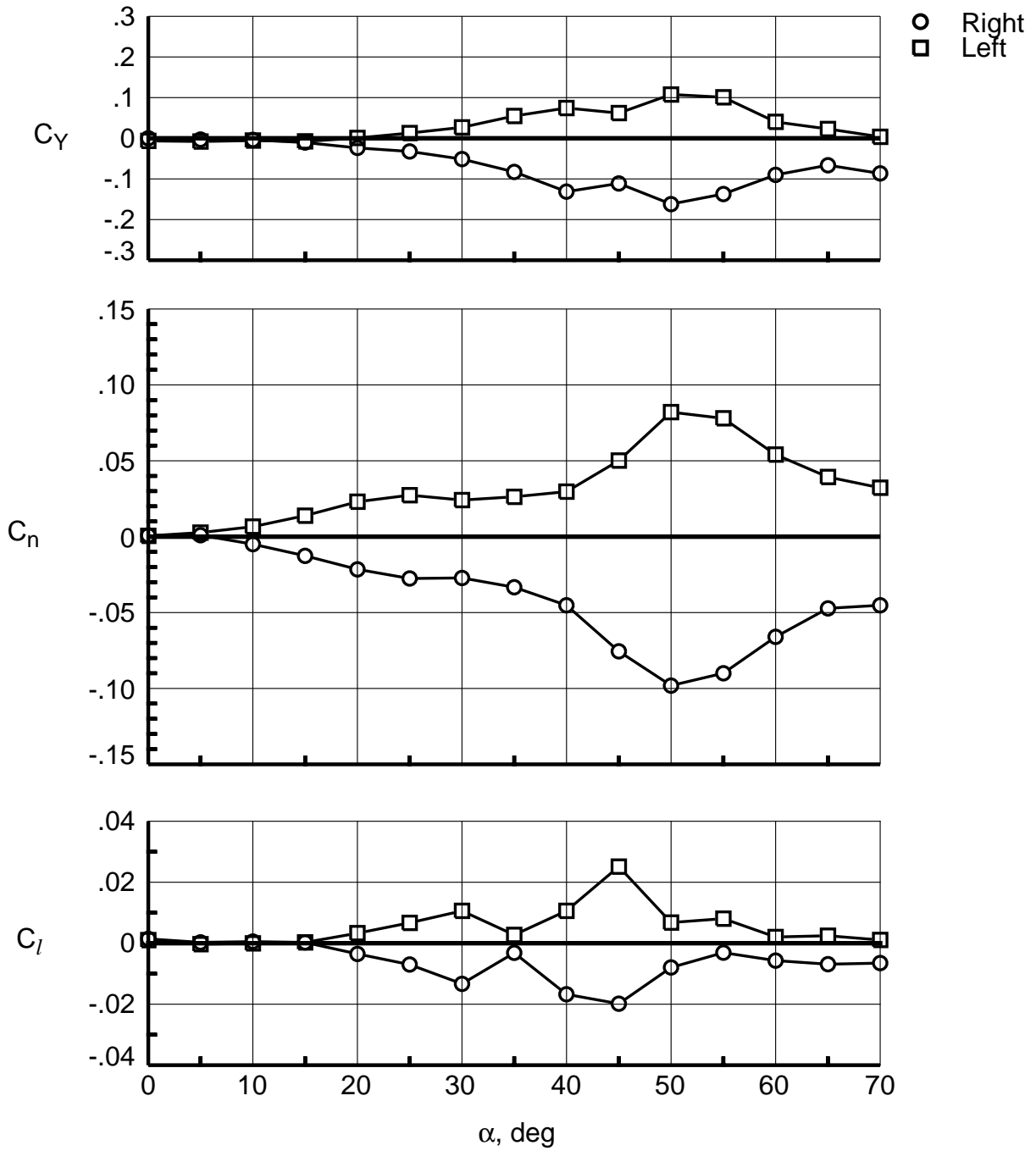
Figure 21. Effect of strake being placed on right or left side of forebody with .3 long ogive strake at $\phi_S = 90°$ with full configuration.
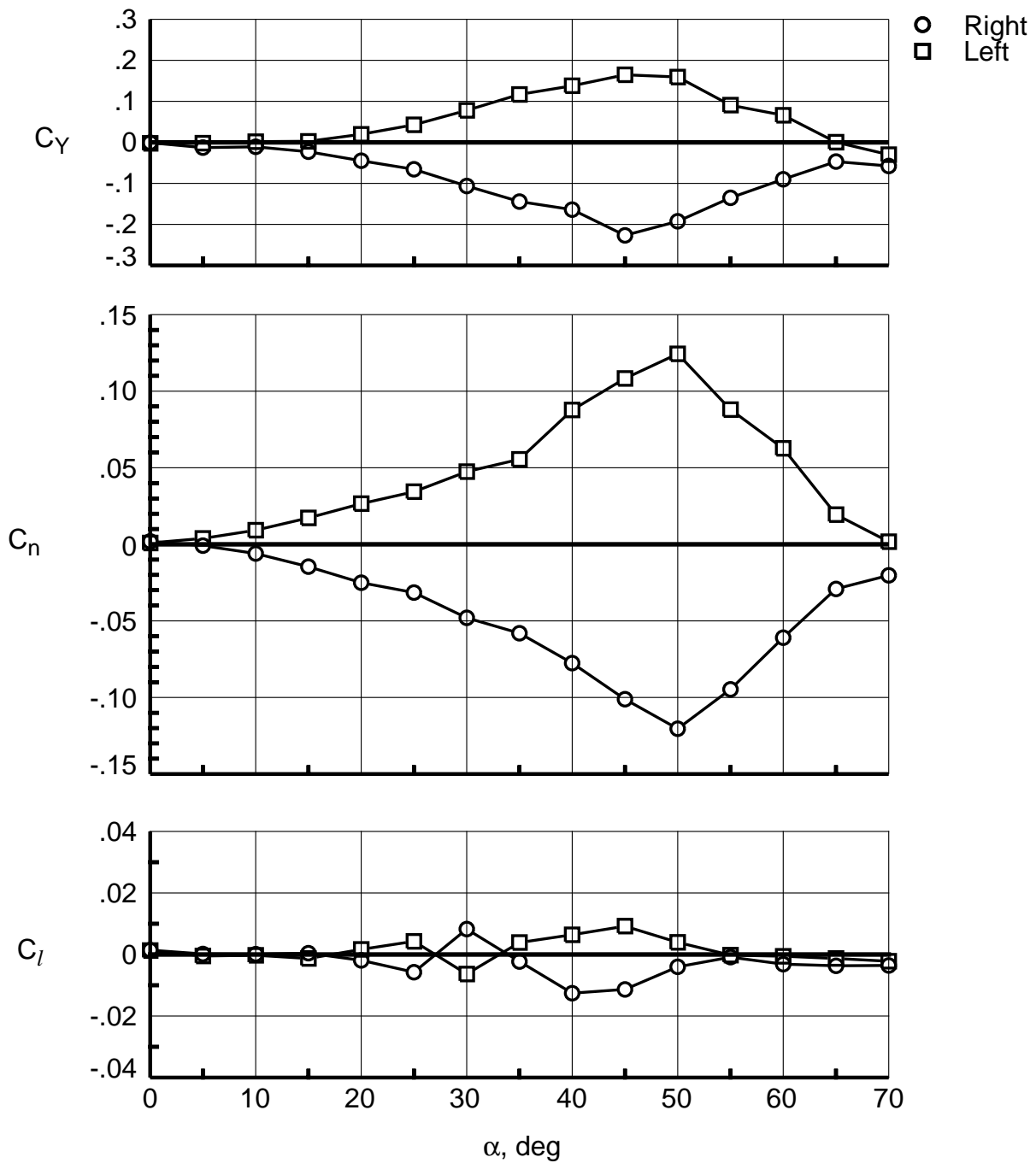
Figure 22. Effect of strake being placed on right or left side of forebody with .3 long ogive strake at $\phi_S = 104°$ with full configuration.
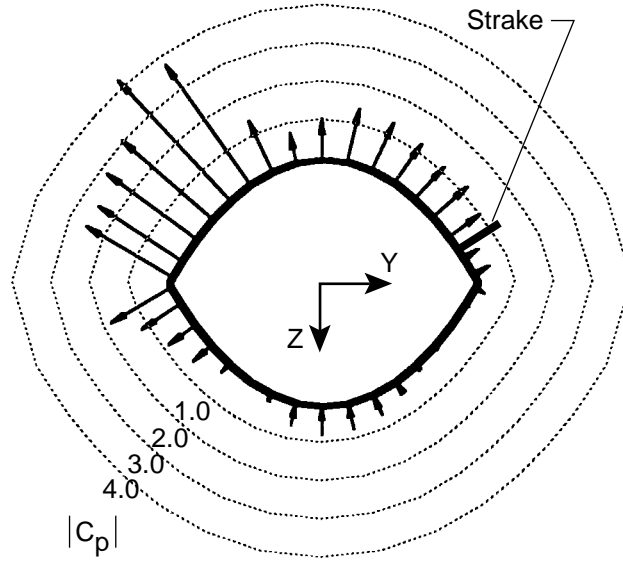
(a) Right side.
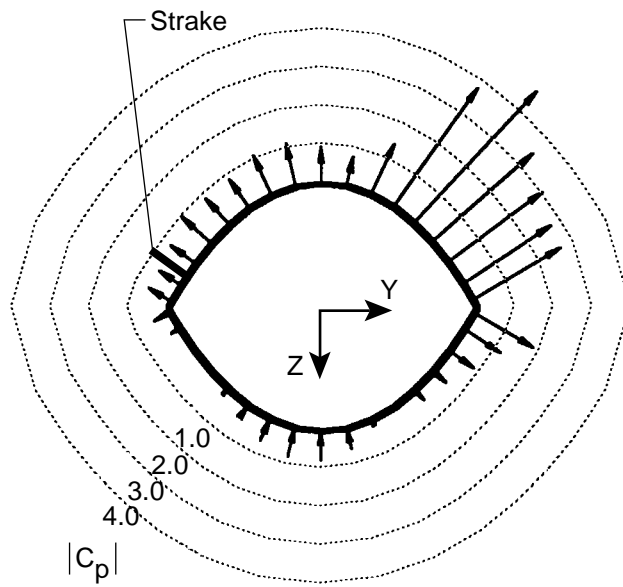
(b) Left side.

Figure 23. Effect of strake placement on pressure distribution at $\alpha = 50°$ with .3 long ogive strake at $\phi_S = 104°$ with full configuration. View is upstream. Arrows leading into cross section indicate compression and arrows leading out of cross section indicate suction.
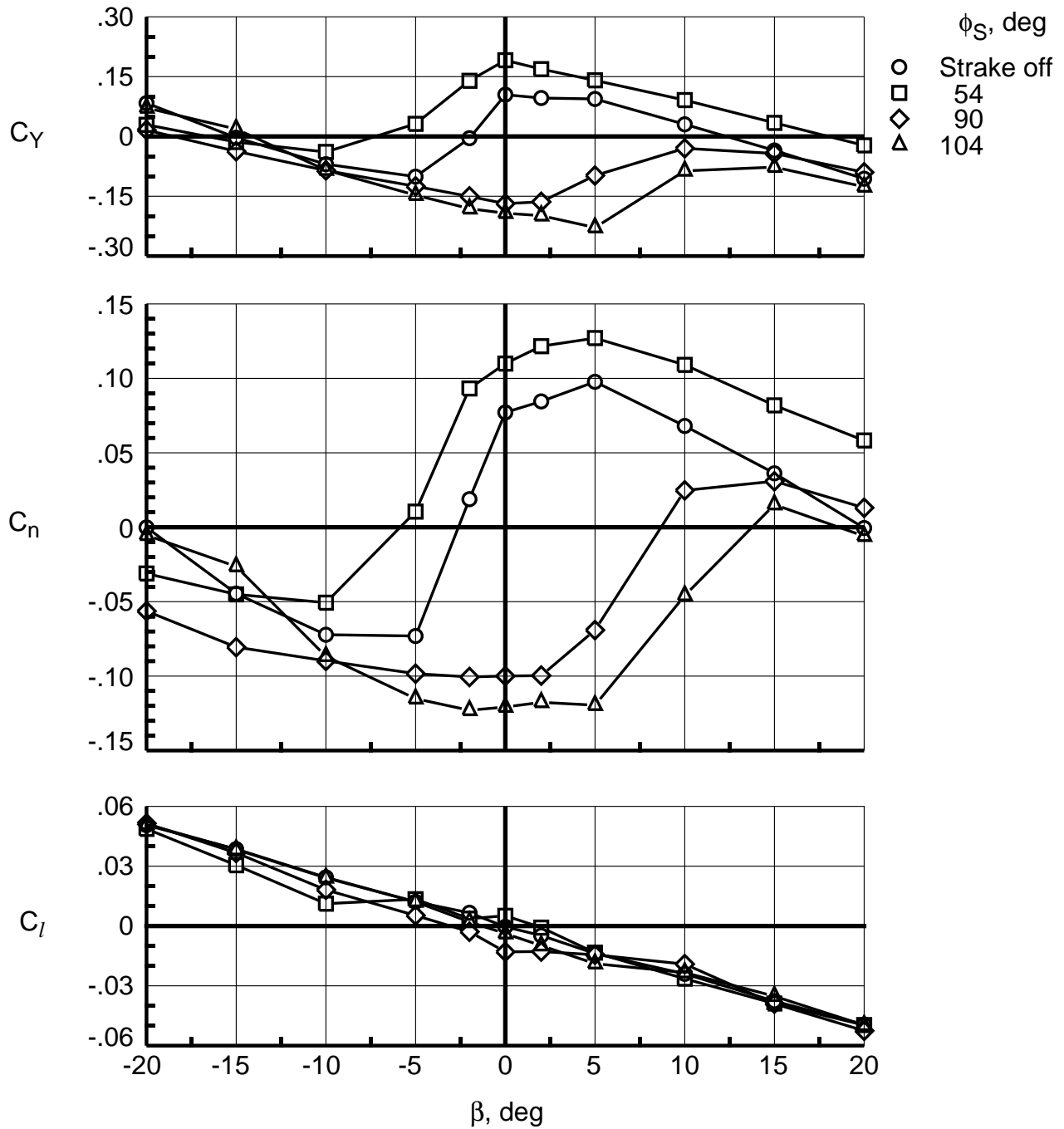
Figure 24. Effectiveness in sideslip at $\alpha = 50°$ for different radial locations with .3 long ogive strake with full configuration.
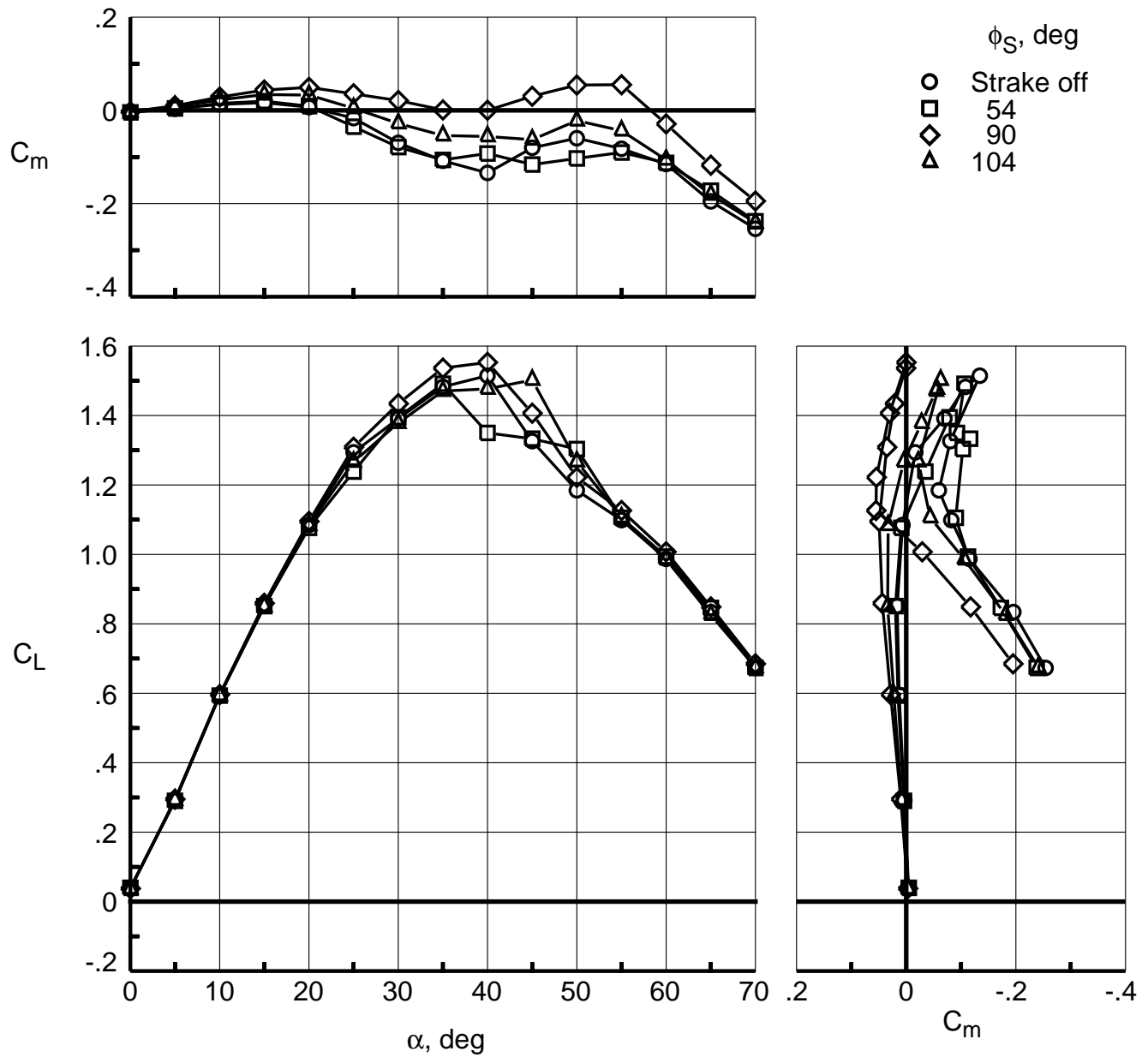
Figure 25. Effect of strake radial location on longitudinal characteristics with .3 long ogive strake with full configuration.
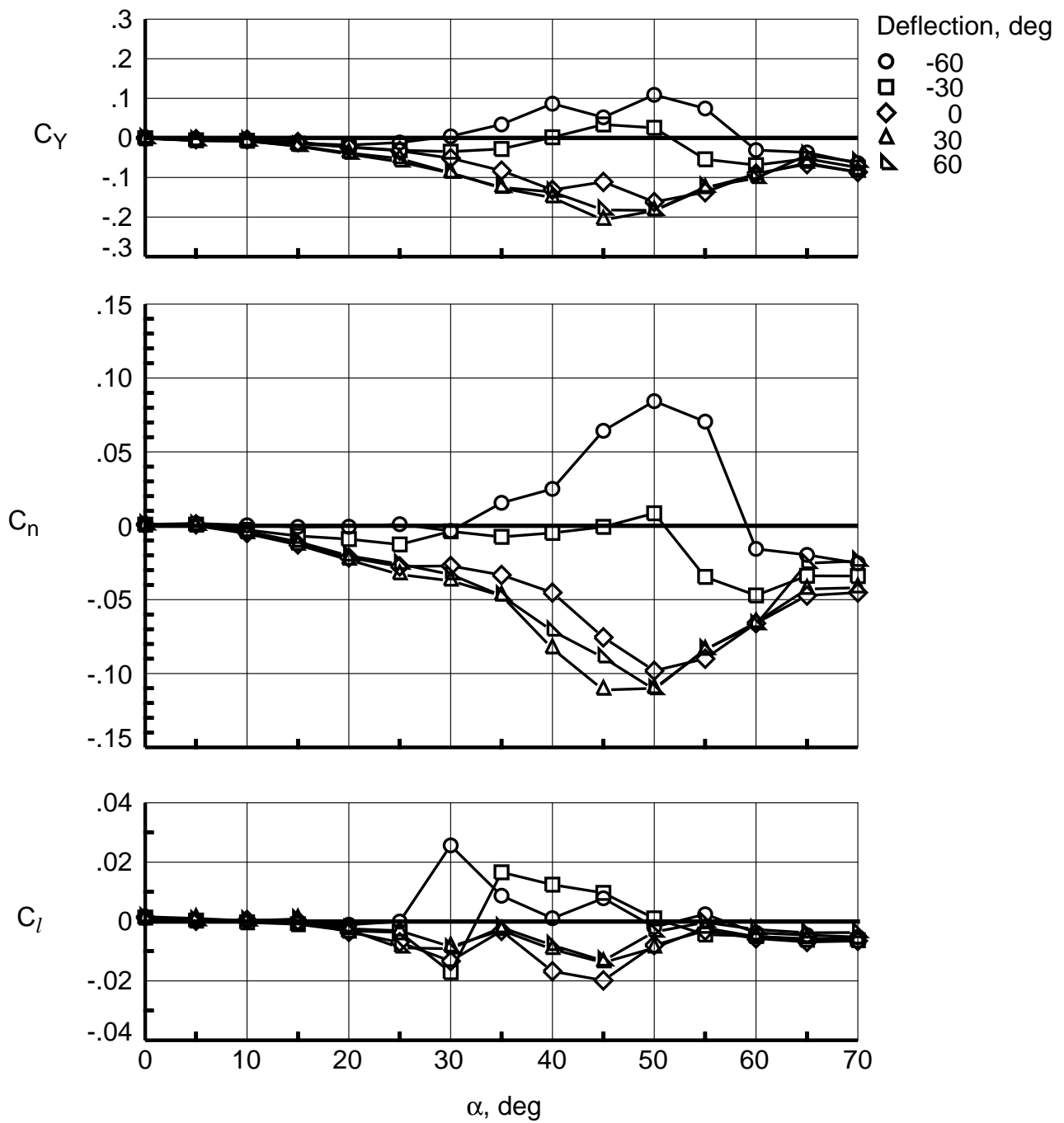
Figure 26. Effect of strake deflections on lateral-directional characteristics with .3 long ogive strake at $\phi_S = 90°$ with full configuration.
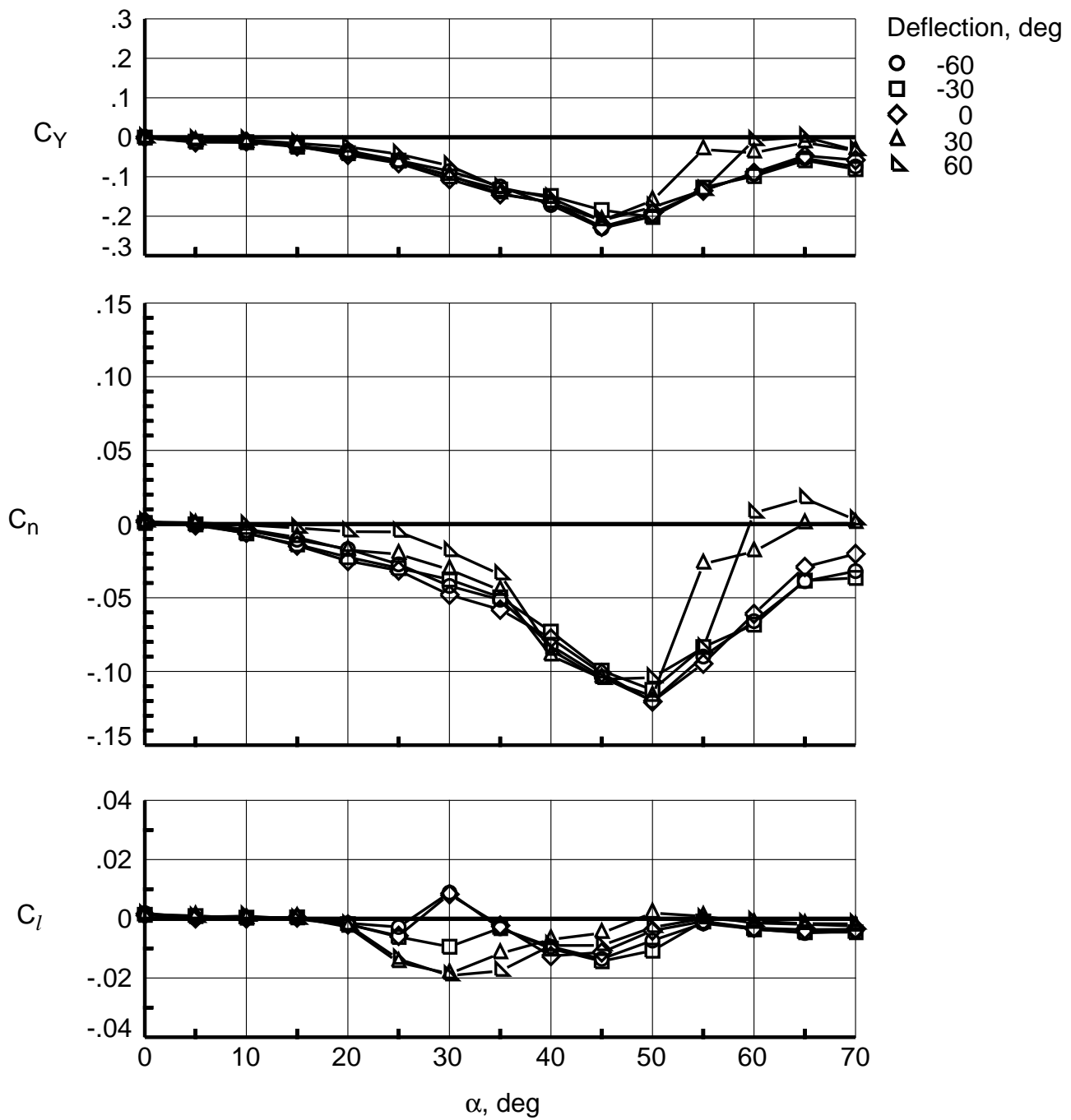
Figure 27. Effect of strake deflections on lateral-directional characteristics with .3 long ogive strake at $\phi_S = 104°$ with full configuration.
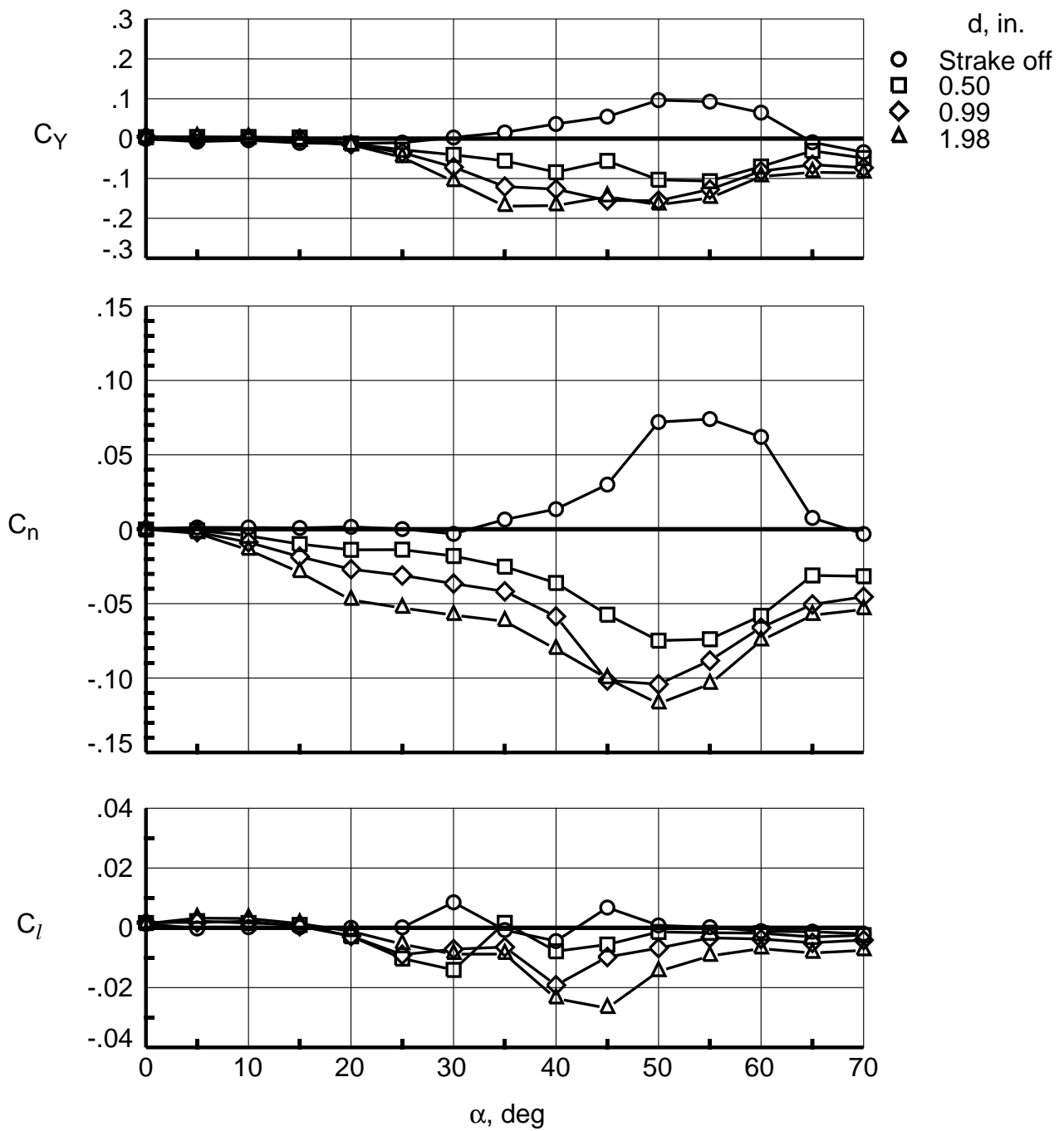
Figure 28. Effect of strake rotation about tip for modulation with long ogive strake at $\phi_S = 90°$ with full configuration.
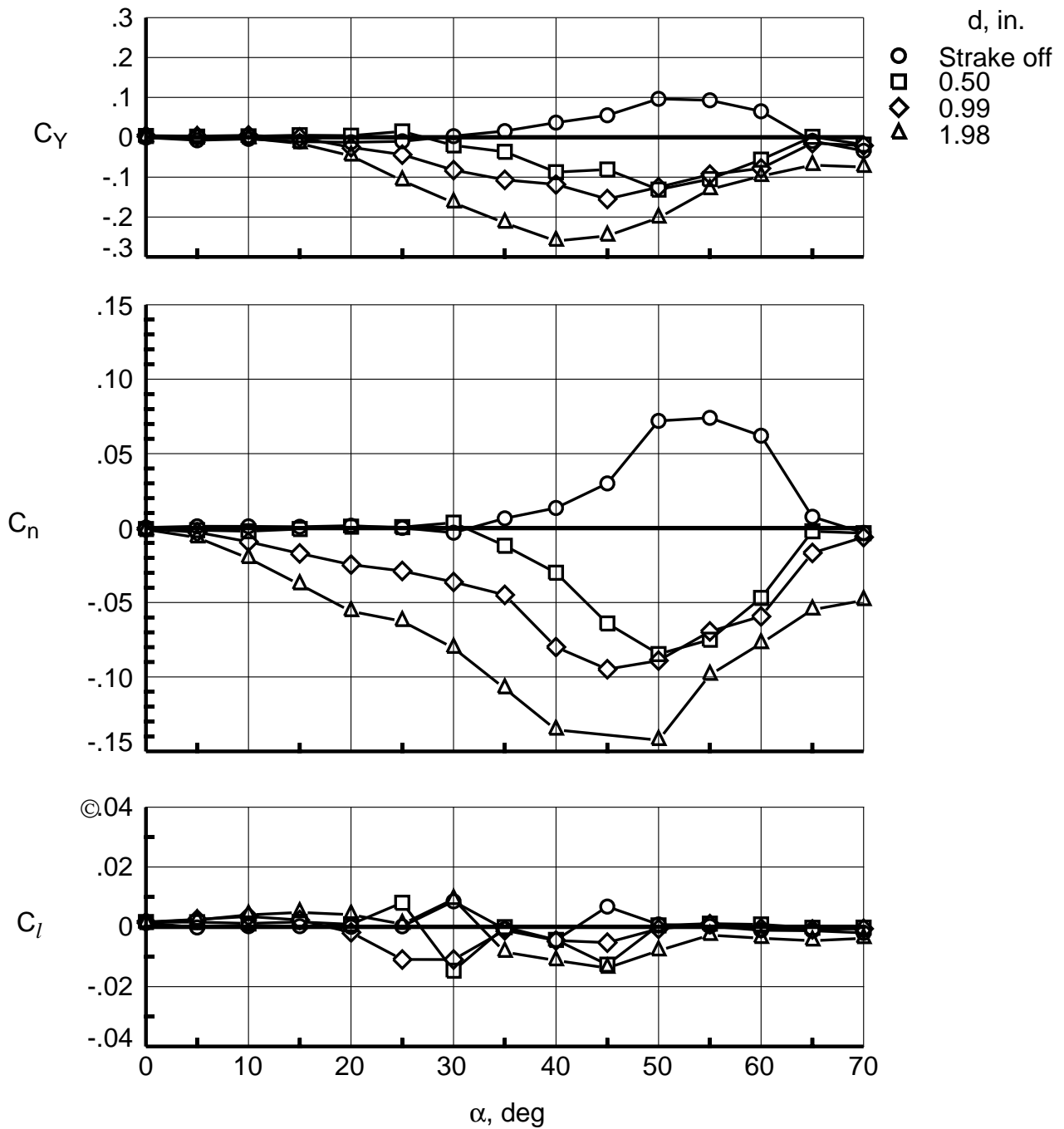
Figure 29. Effect of strake rotation about tip for modulation with long ogive strake at $\phi_S = 104°$ with full configuration.
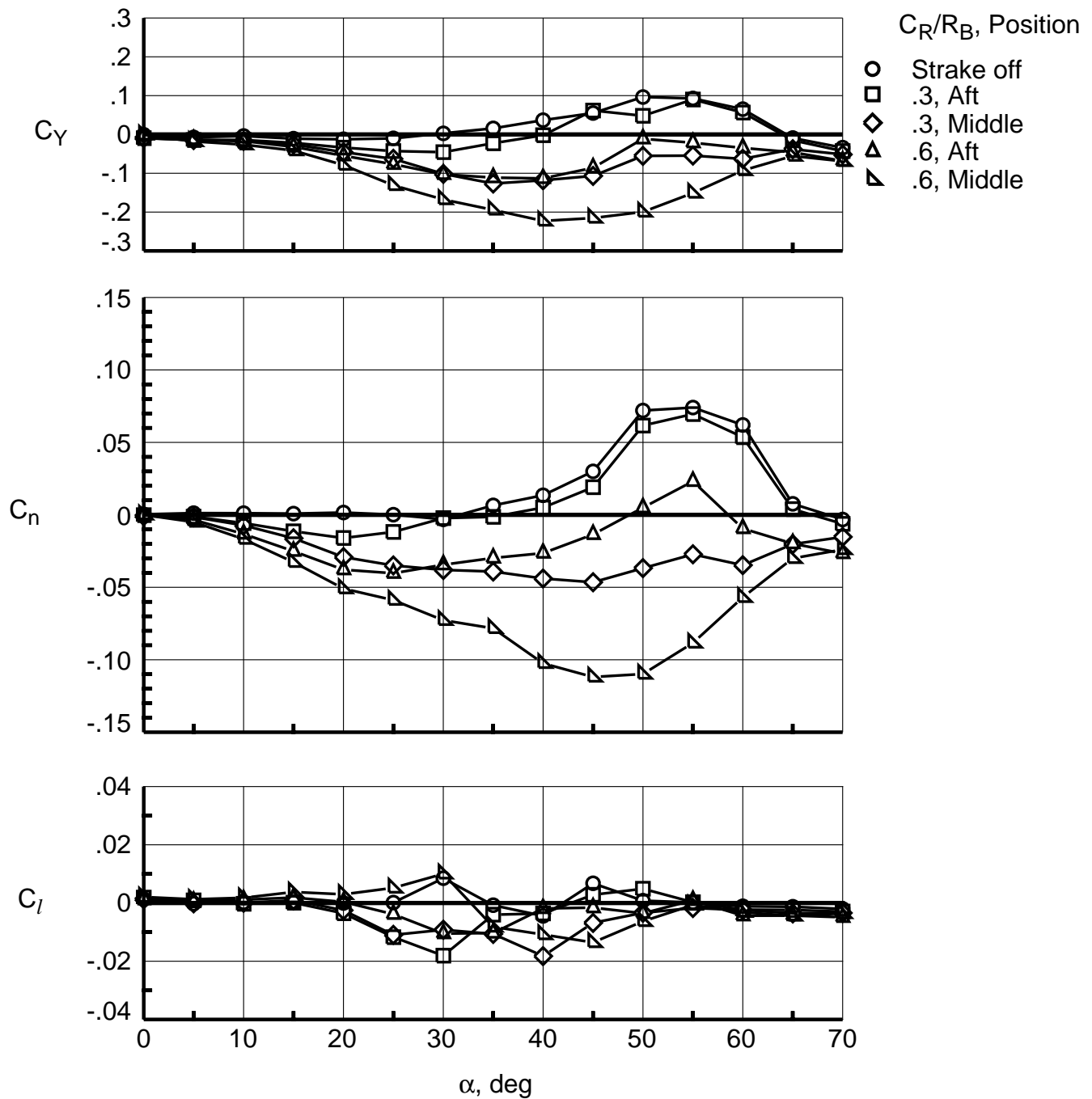
Figure 30. Effect of variation of C_R/R_B and axial position on lateral-directional characterisitics with cropped strake at $\phi_S = 104°$ with full configuration.

$\phi_S = 104°$

.3 cropped strake

Indicates direction of resultant force
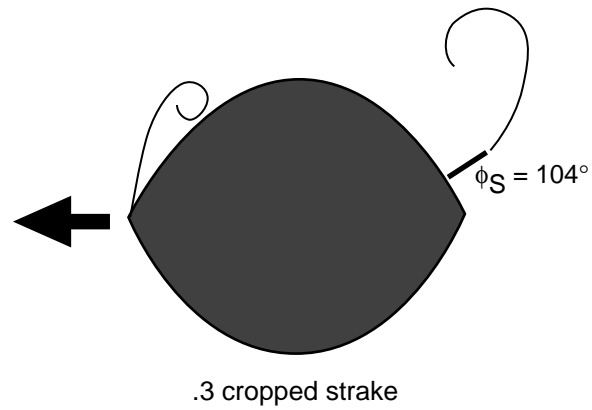
$\phi_S = 104°$
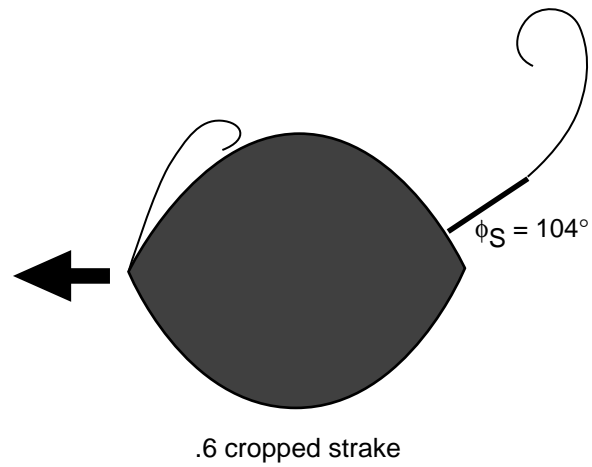
.6 cropped strake

Figure 31. Cross-flow sketches at $\alpha = 50°$ for .3 cropped strake and .6 cropped strake in middle position at $\phi_S = 104°$ with full configuration. Sketches based on flow visualization. View is upstream.
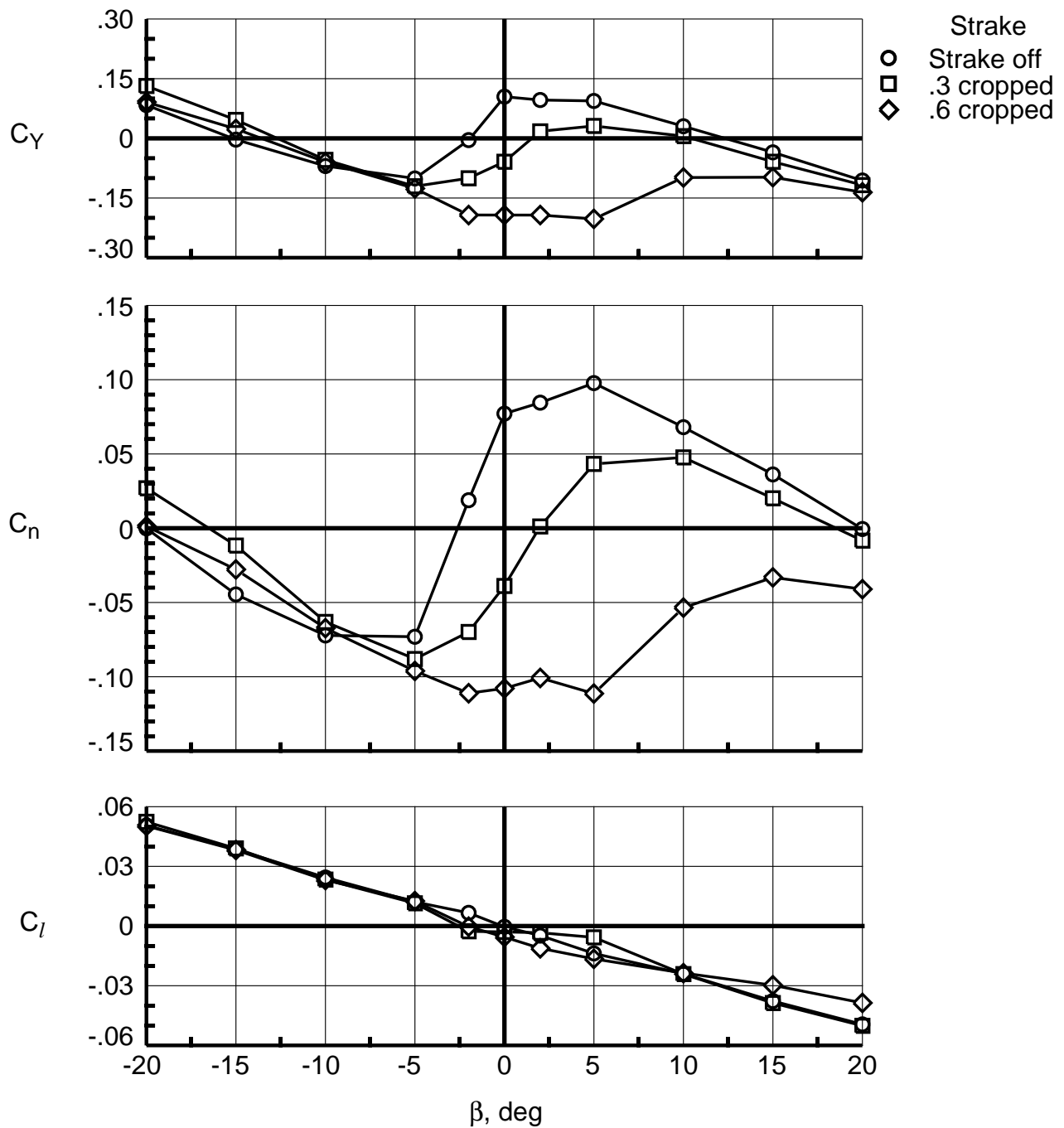
Figure 32. Effectiveness in sideslip at $\alpha = 50°$ with cropped strakes in middle position at $\phi_S = 104°$ with full configuration.
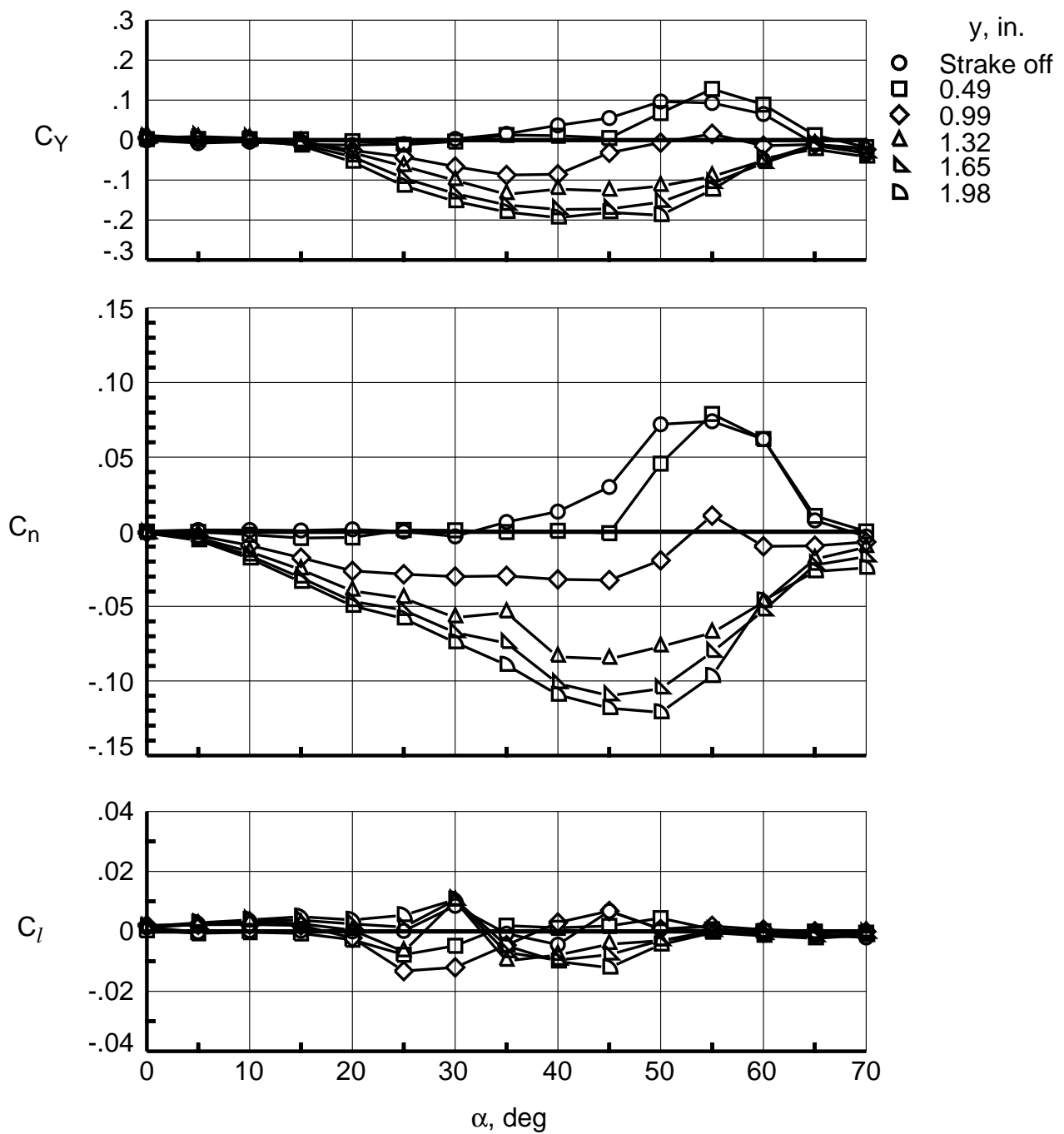
Figure 33. Effect of lateral translation to simulate modulation of .6 cropped strake in middle position at $\phi_S = 104°$ with full configuration.
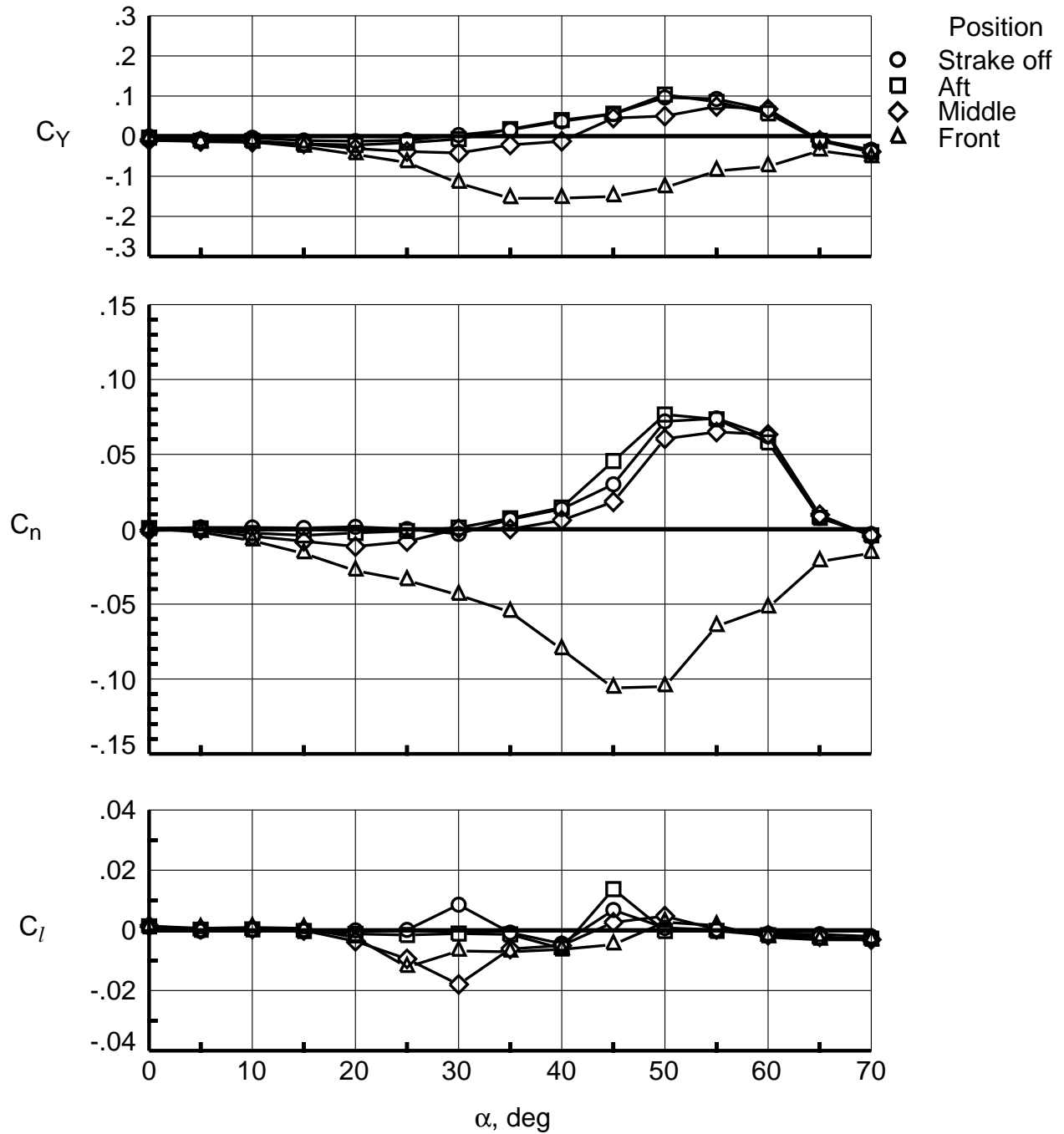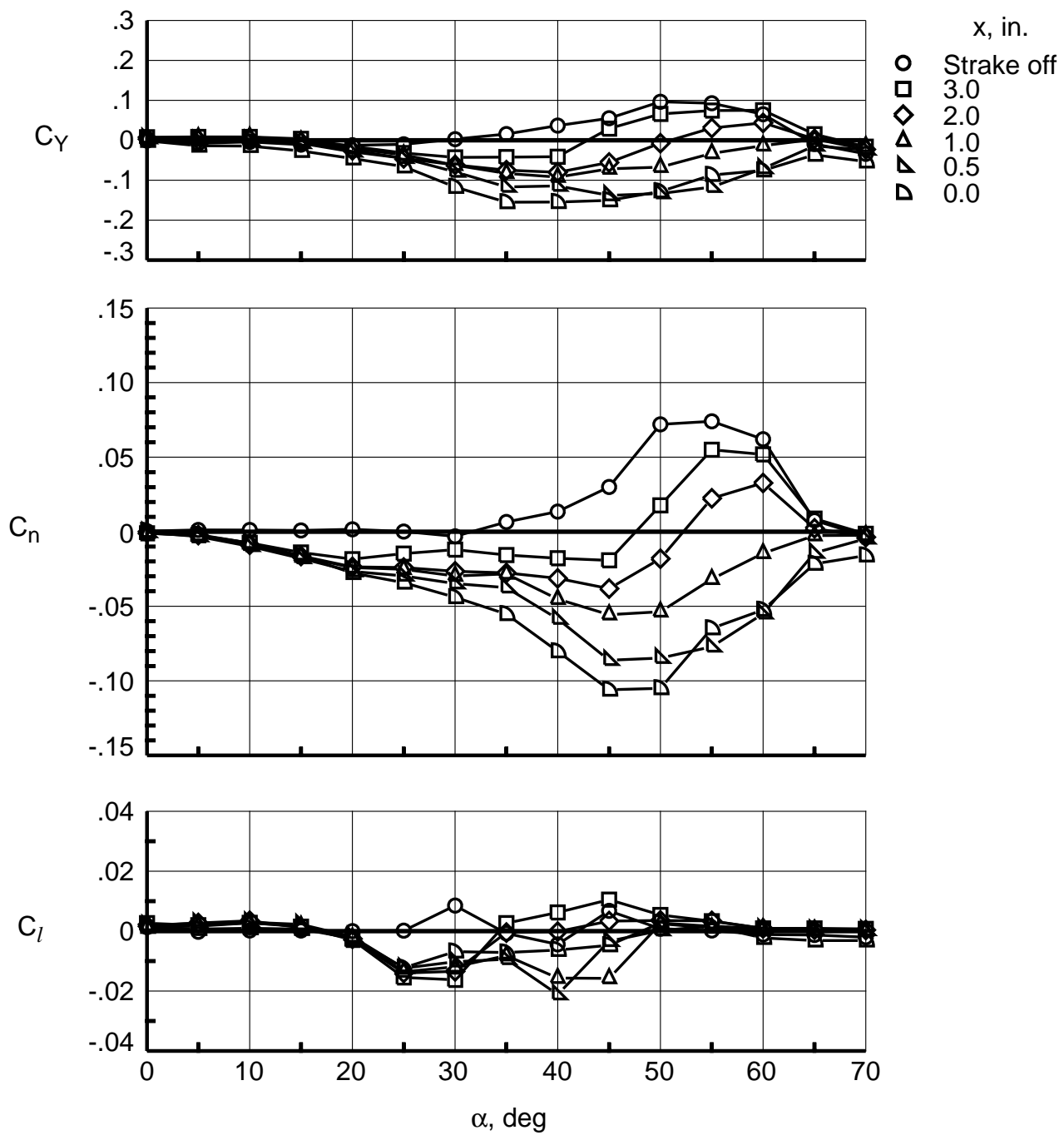
Figure 34. Effect of axial position on lateral-directional characteristics with .3 short ogive strake at $\phi_S = 104°$ with full configuration.
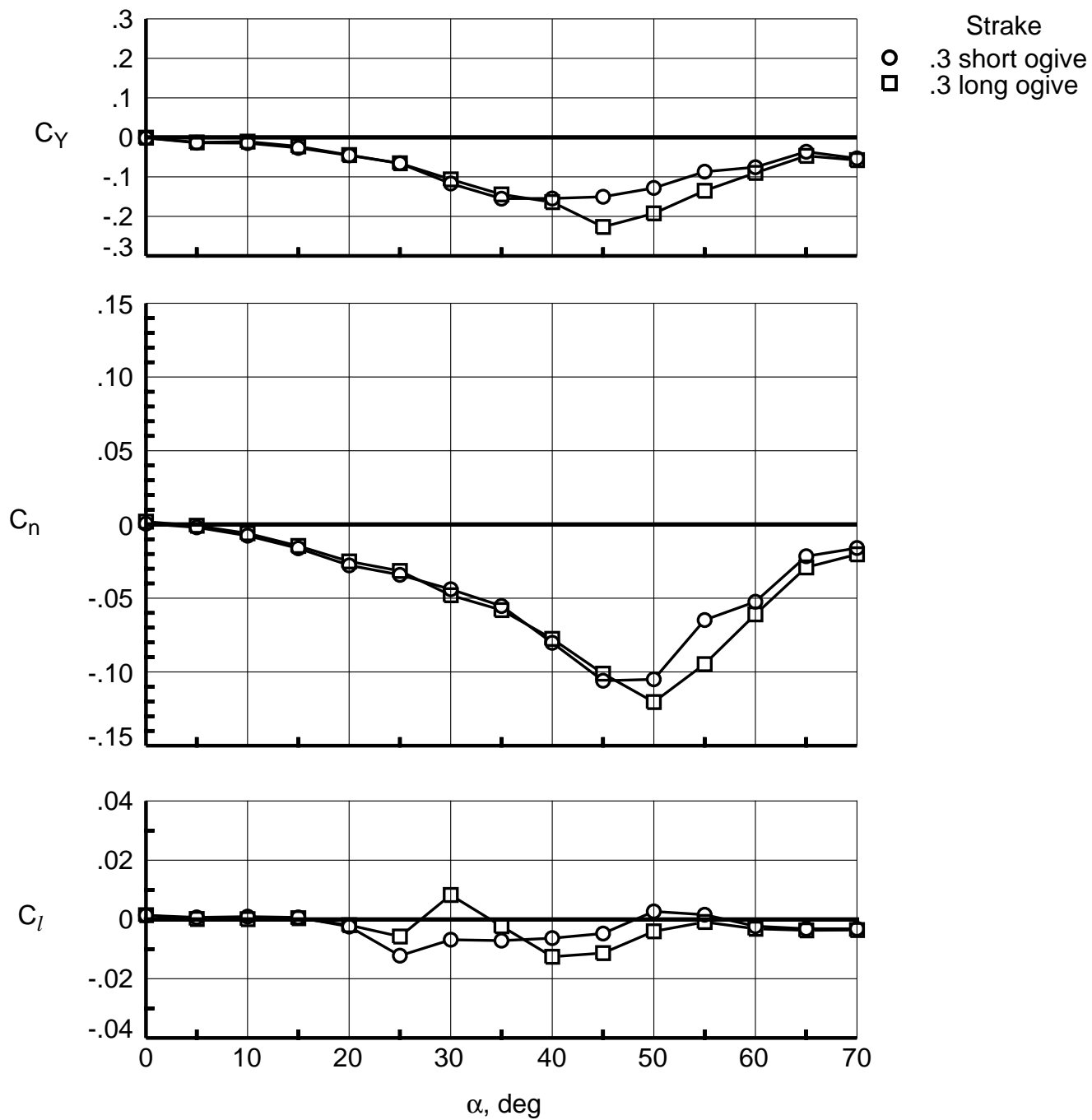
Figure 35. Comparison of .3 short ogive strake in front position with .3 long ogive strake at $\phi_S = 104°$ with full configuration.
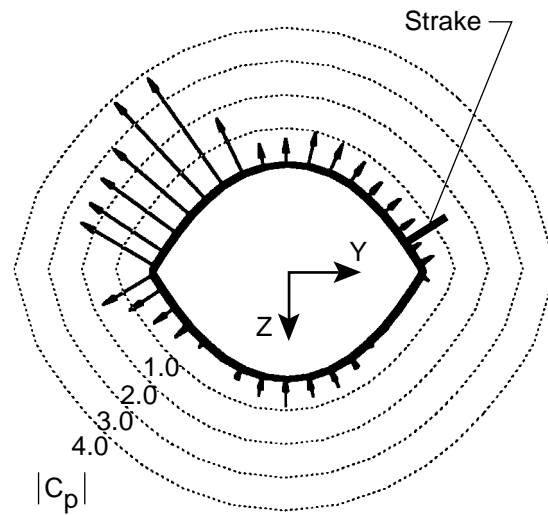
Figure 36. Pressure distribution at $\alpha = 50°$ for .3 short ogive strake in front position at $\phi_S = 104°$ with full configuration. View is upstream. Arrows leading into cross section indicate compression and arrows leading out of cross section indicate suction.
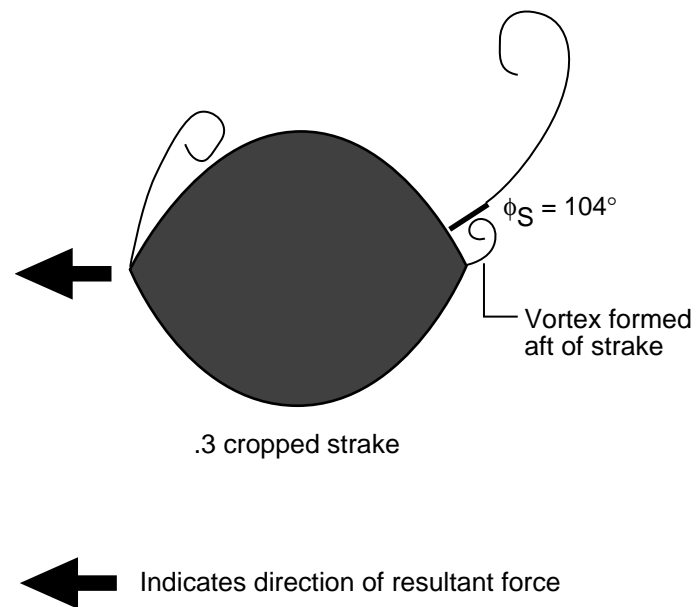
Figure 37. Cross-flow sketch at $\alpha = 50°$ for .3 short ogive strake in front position at $\phi_S = 104°$ with full configuration. Sketch based on flow visualization. View is upstream.

$\phi_S = 104°$

Vortex formed
aft of strake
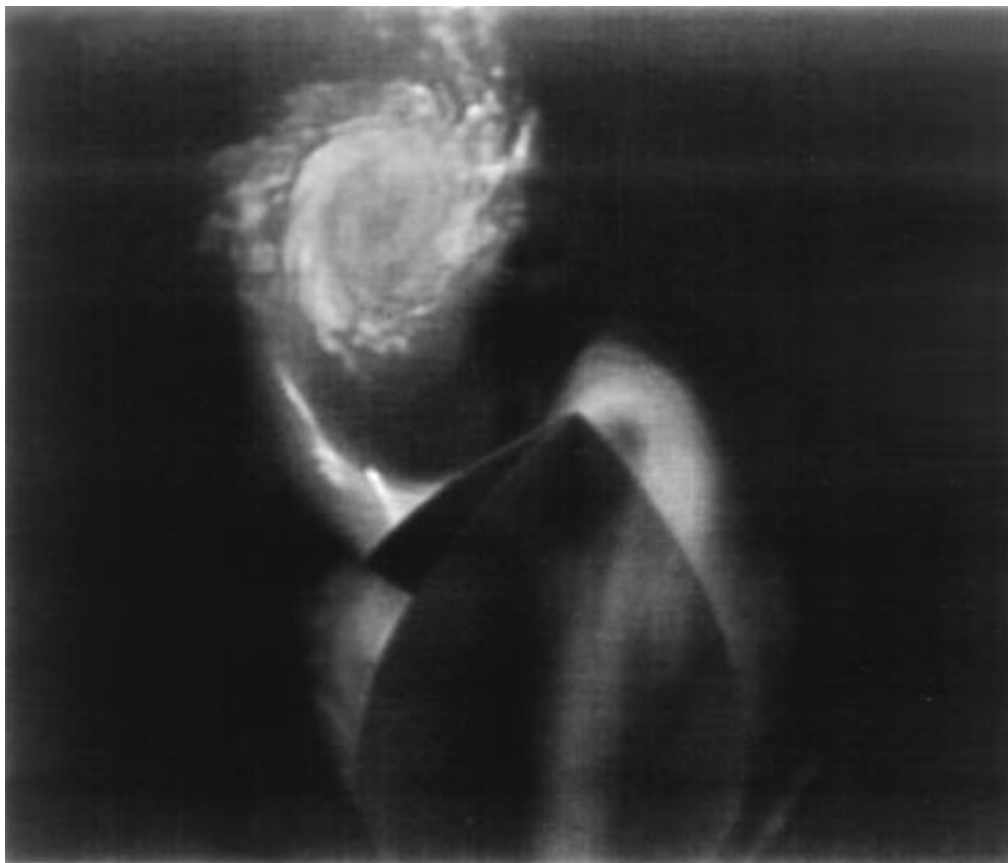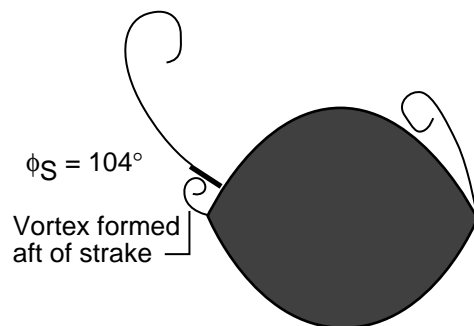
Figure 38. Flow visualization at $\alpha = 50°$ for .3 short ogive strake in front position at $\phi_S = 104°$ with full configuration. View is downstream. Cross-flow sketch is mirror image of figure 37.
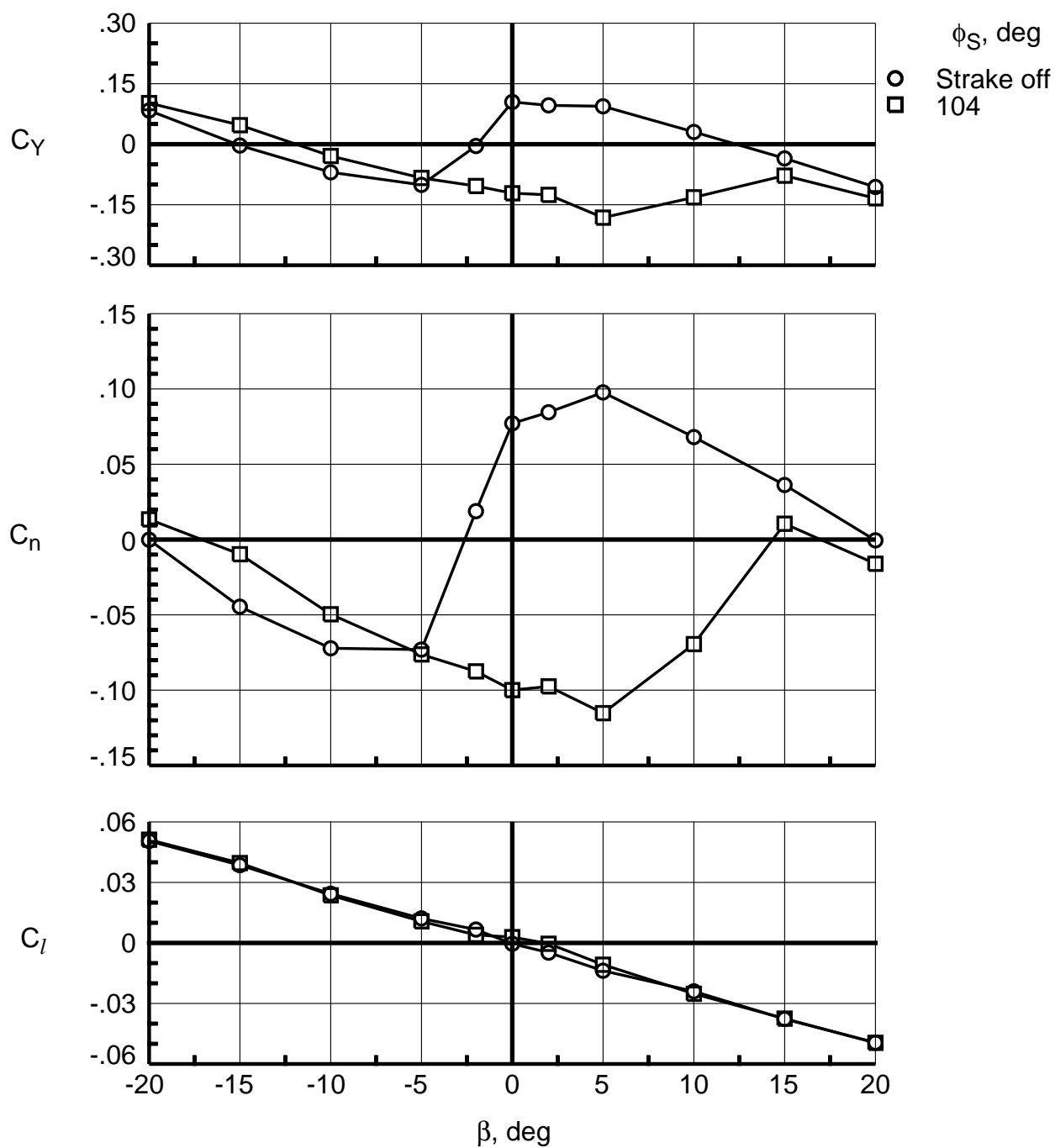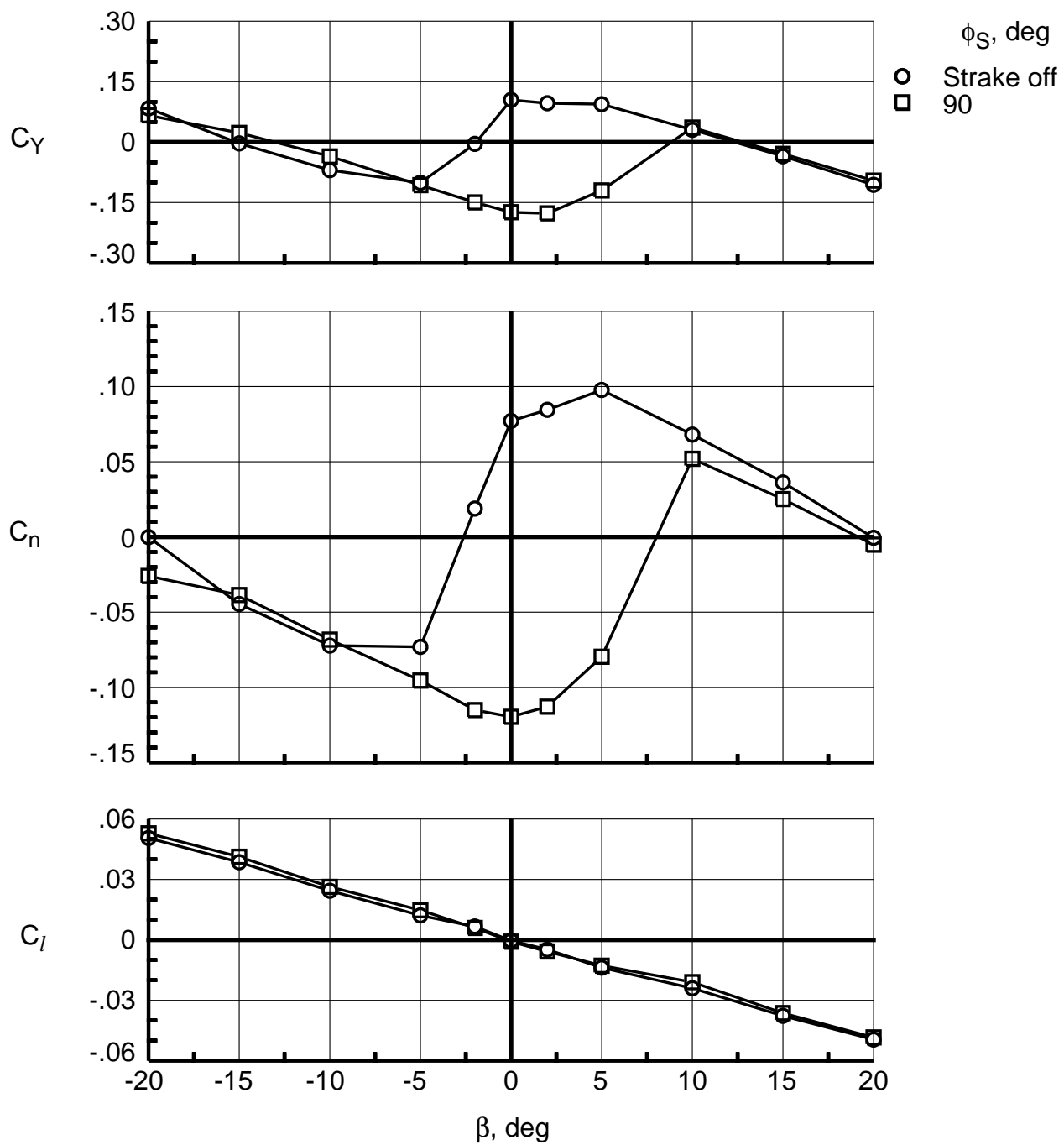
Figure 39. Effectiveness in sideslip at $\alpha = 50°$ with .3 short ogive strake in front position with full configuration.

Figure 40. Effect of axial translation on lateral-directional characteristics with .3 short ogive strake at $\phi_S = 104°$ with full configuration.
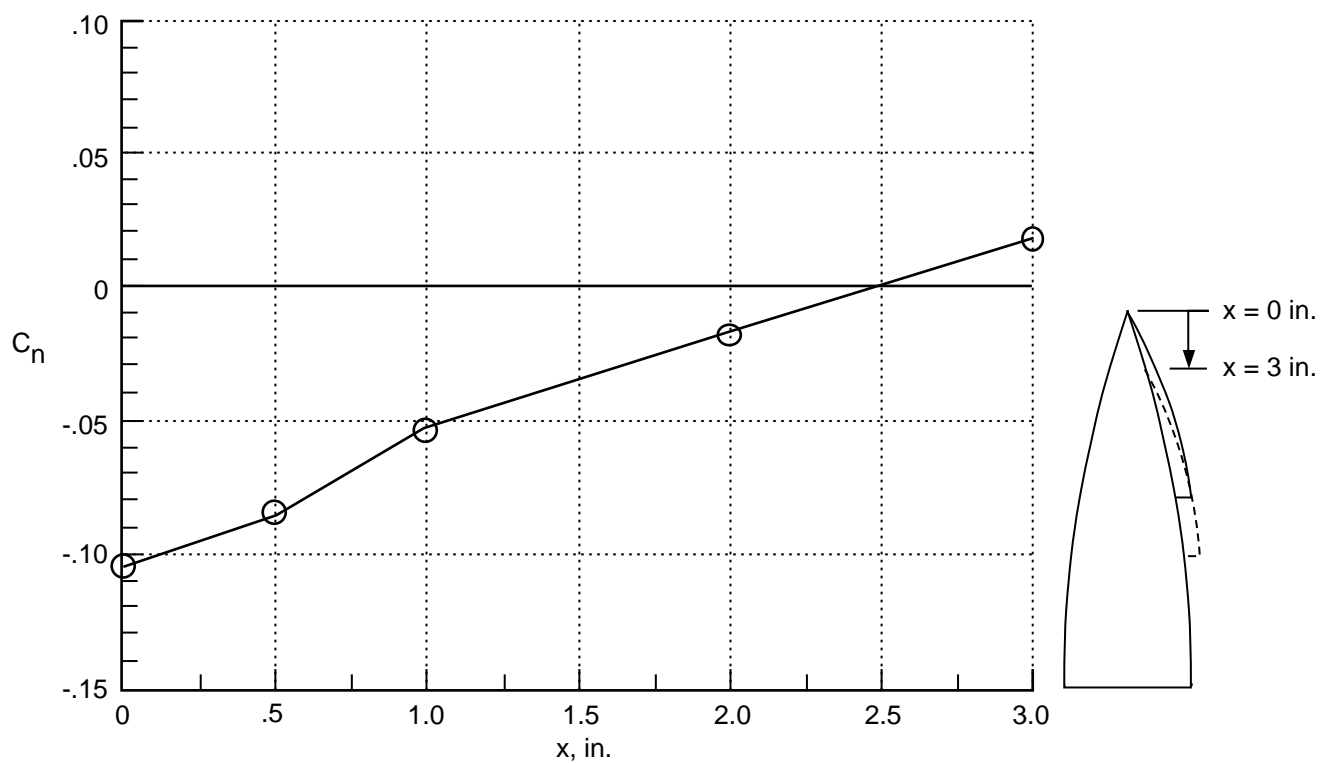
Figure 41. Effect of axial translation on yawing moment coefficient at $\alpha = 50°$ with .3 short ogive strake at $\phi_S = 104°$ with full configuration.
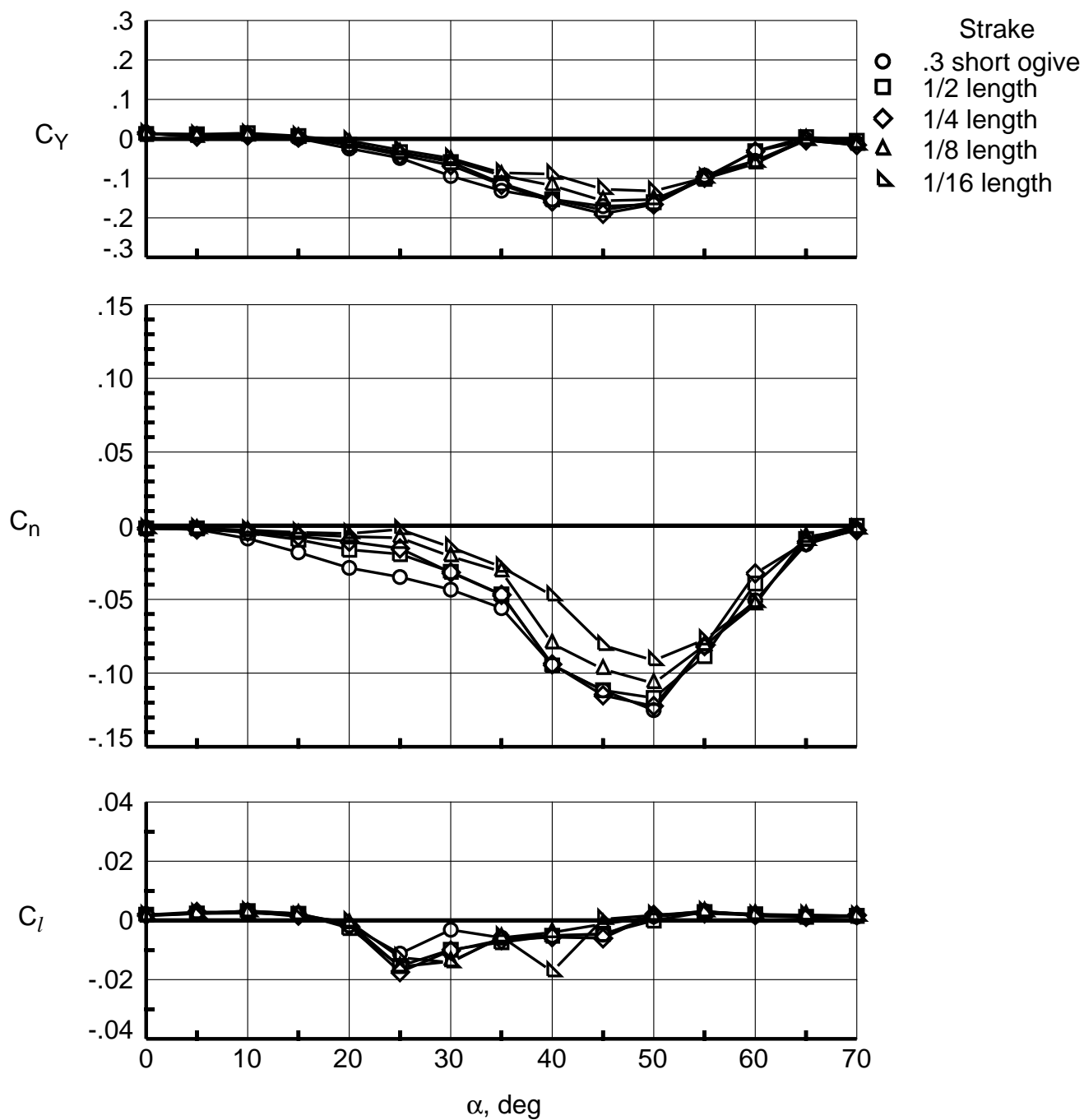
Figure 42. Effect of strake length on lateral-directional characteristics at $\phi_S = 104°$ with full configuration.
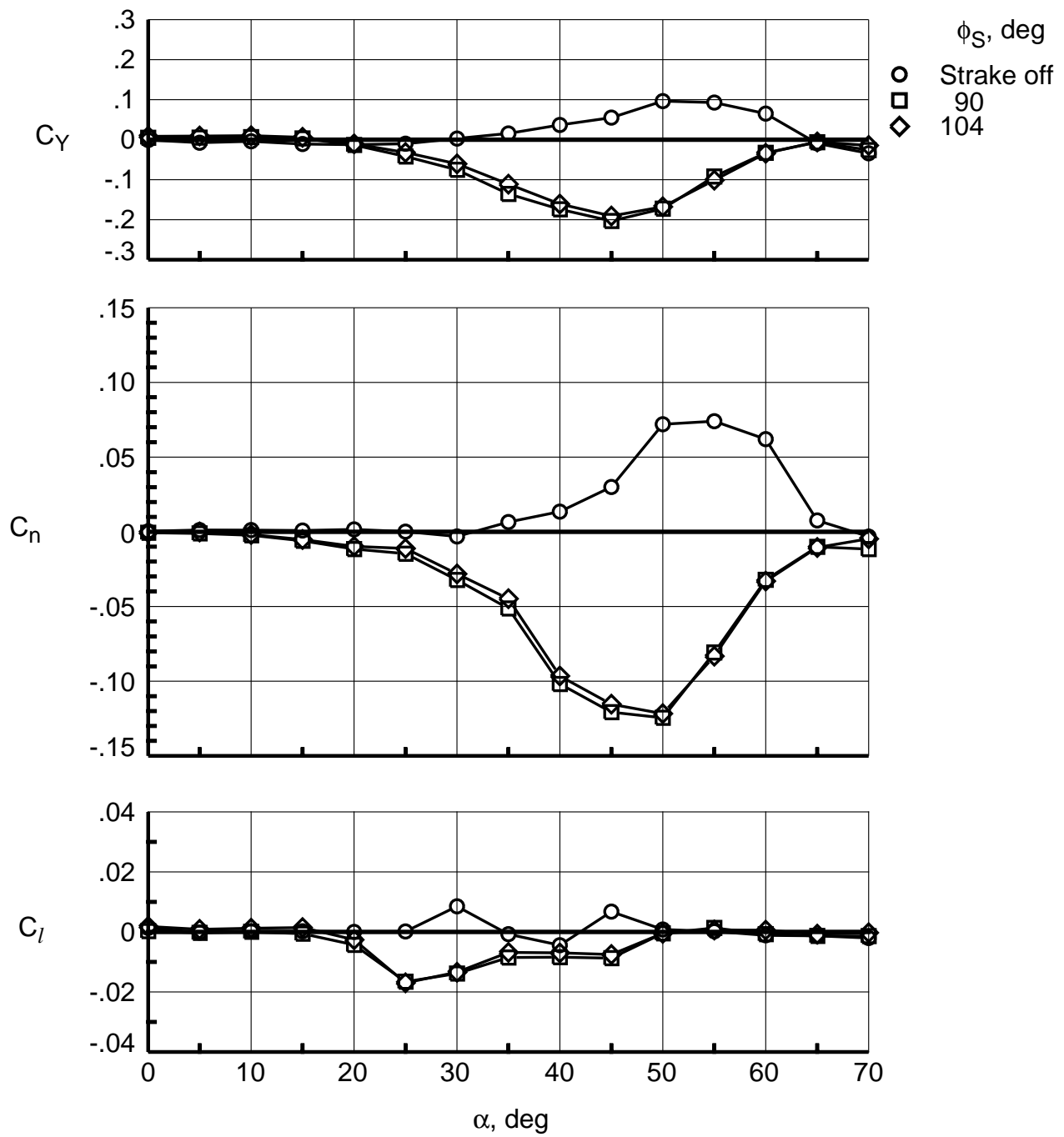
Figure 43. Effect of strake radial location on lateral-directional characteristics with 1/4 length .3 short ogive strake at forebody tip with full configuration.
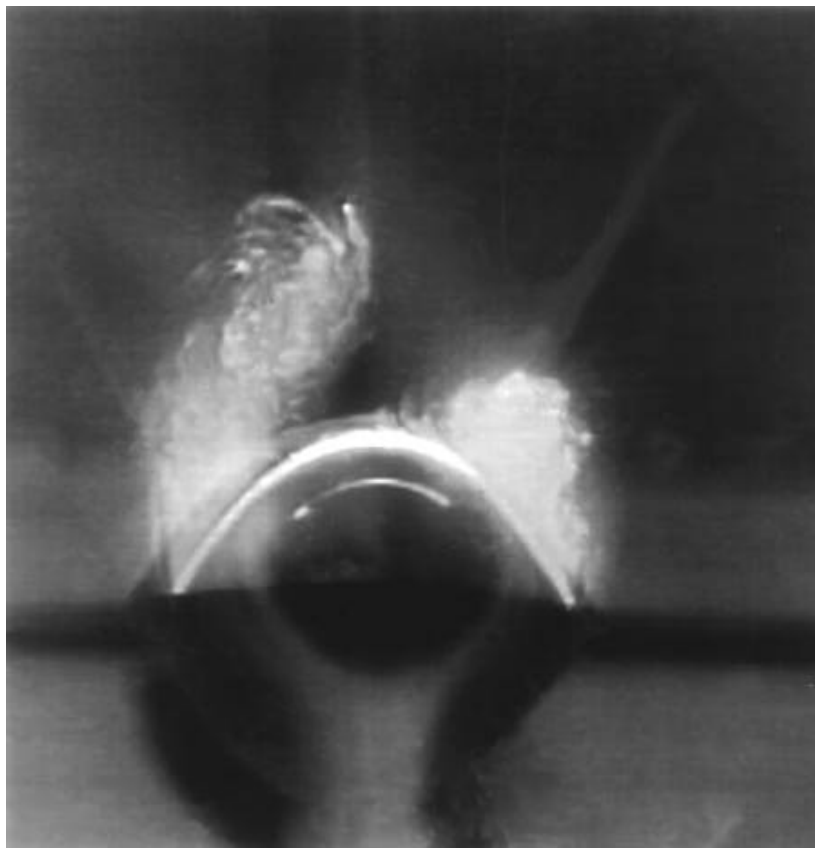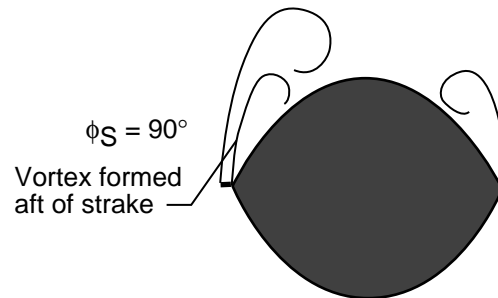
Figure 44. Cross-flow sketch and flow visualization at $\alpha = 40°$ for 1/4 length .3 short ogive strake in front position at $\phi_S = 90°$ with full configuration. View is downstream.
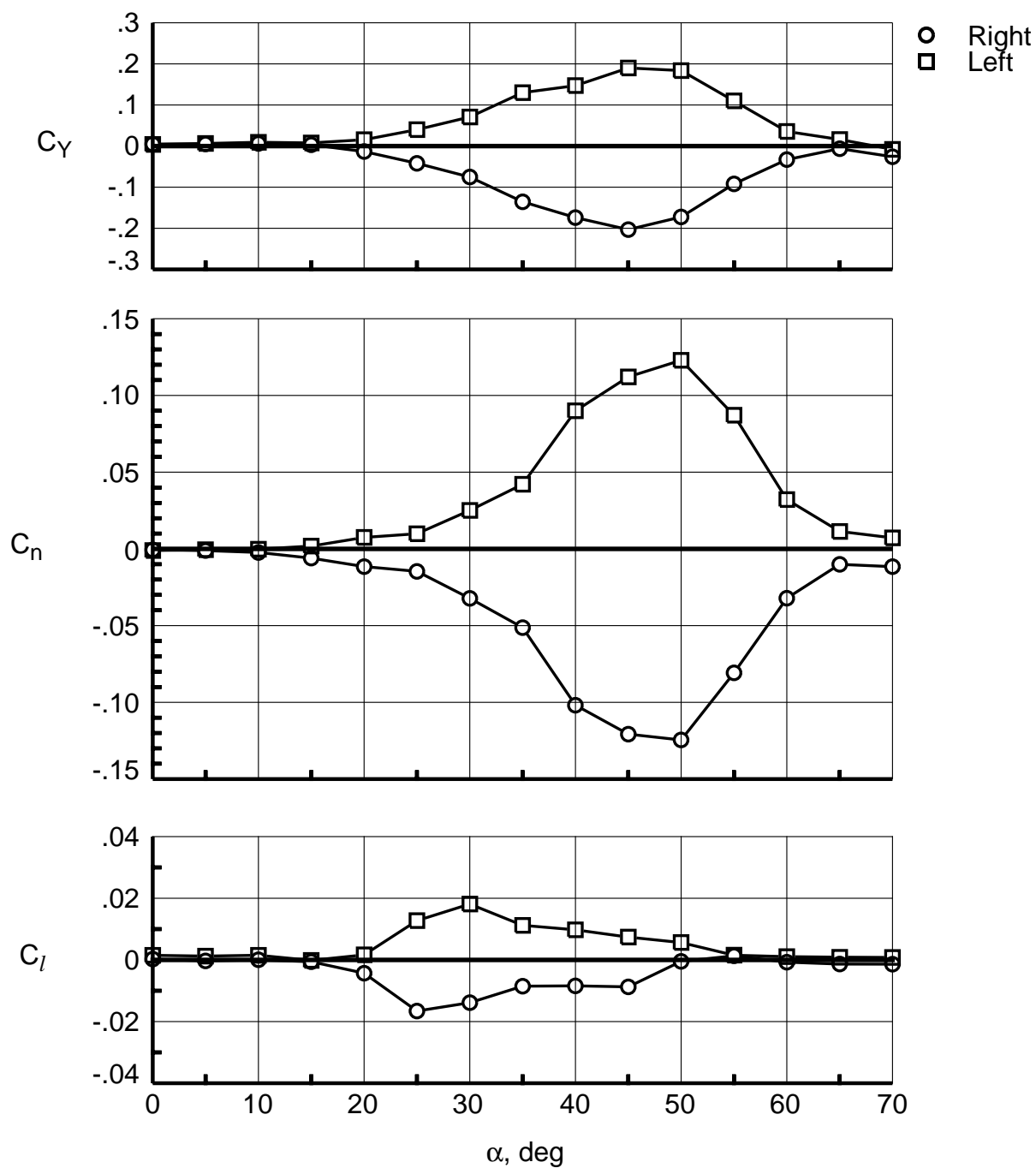
Figure 45. Effect of strake on right and left sides of forebody with 1/4 length .3 short ogive strake at $\phi_S = 90°$ at forebody tip with full configuration.

Figure 46. Effectiveness in sideslip at $\alpha = 50°$ with 1/4 length .3 short ogive strake in front position with full configuration.
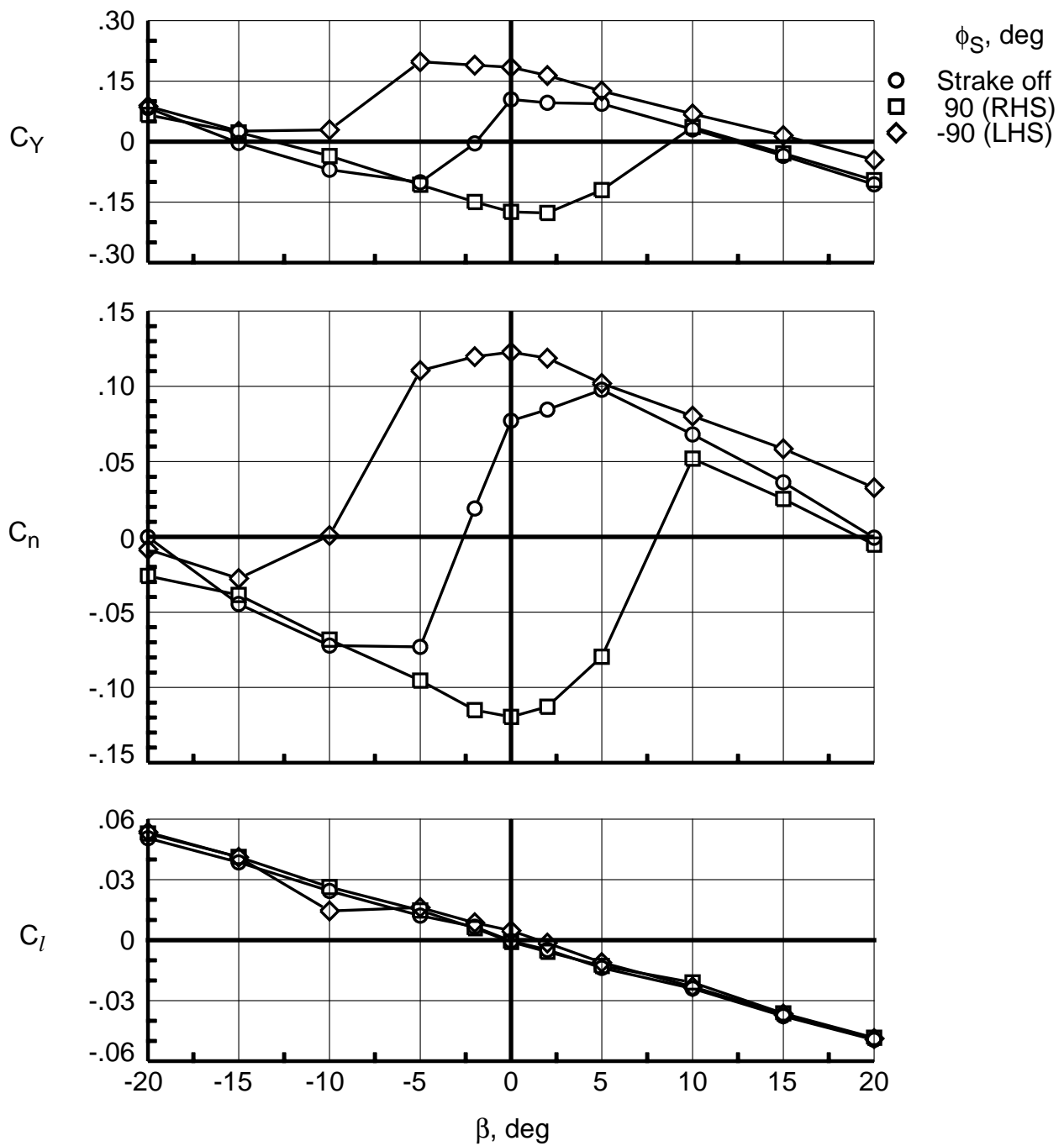
Figure 47. Effect of strake being placed on right (RHS) or left (LHS) side of forebody with 1/4 length .3 short ogive strake in front position with full configuration.
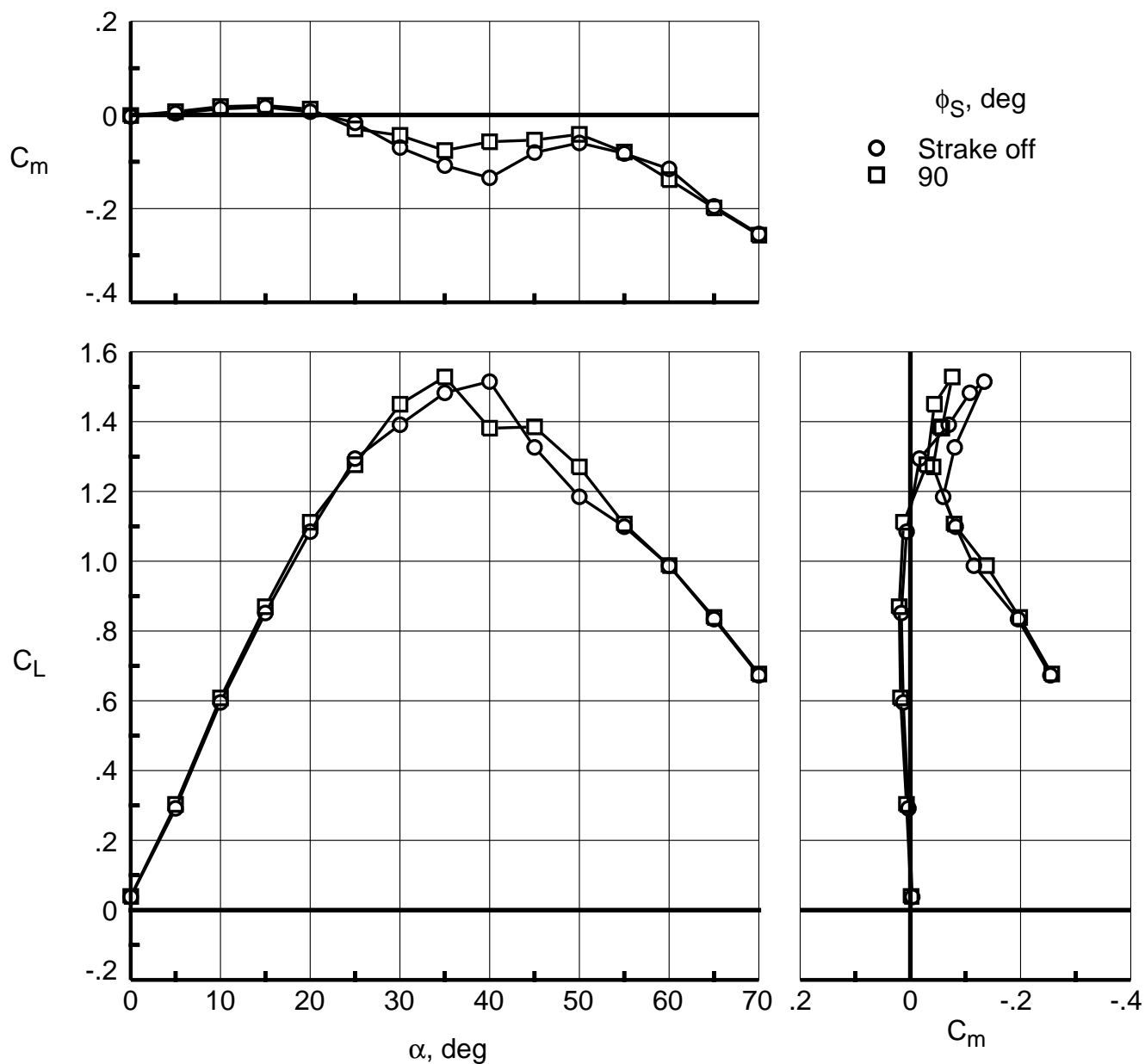
Figure 48. Effect of strake radial location on longitudinal characteristics with 1/4 length .3 short ogive at forebody tip with full configuration.
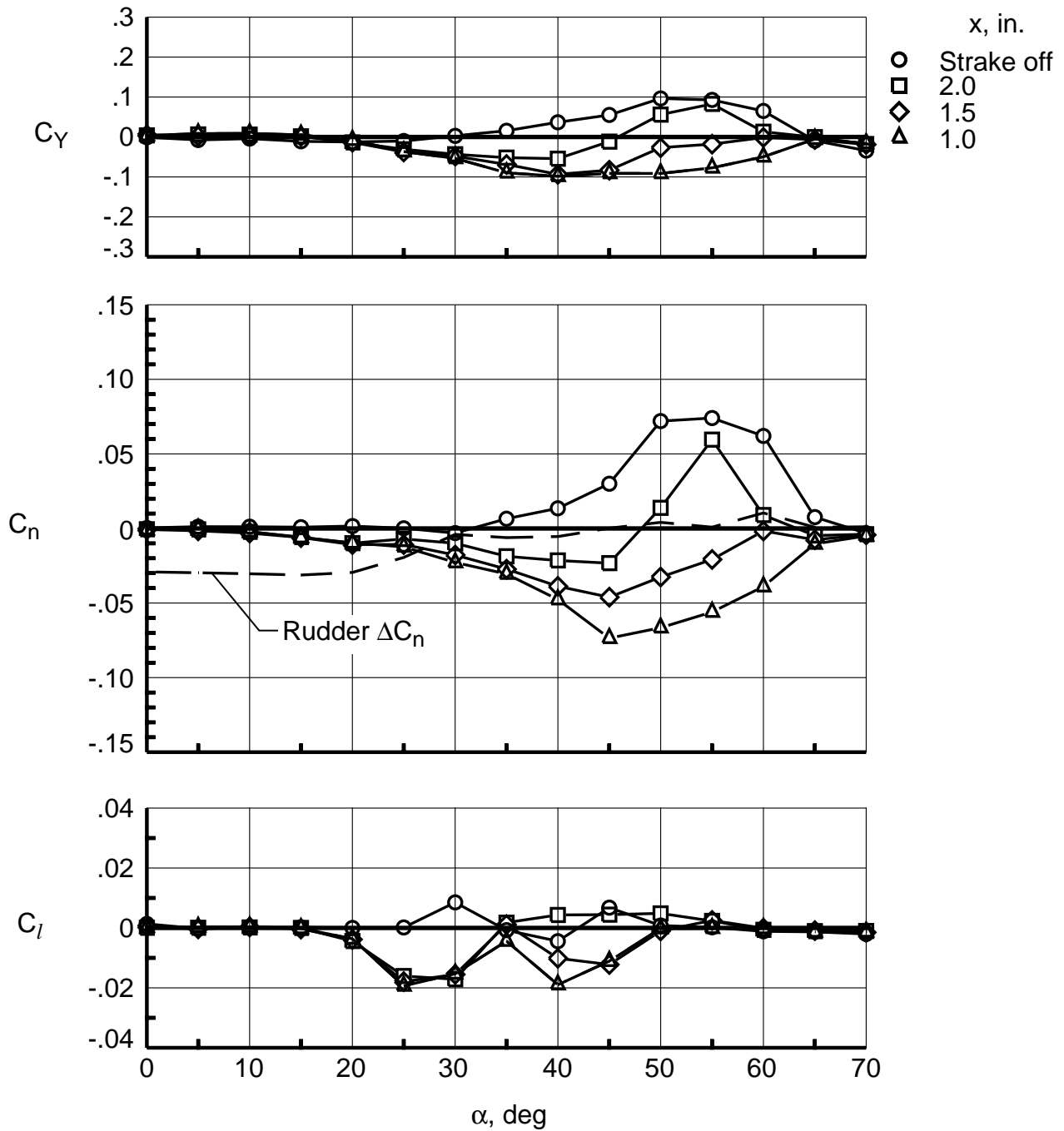
Figure 49. Effect of axial translation on lateral-directional characteristics with 1/4 length .3 short ogive strake at $\phi_S = 90°$ with full configuration.
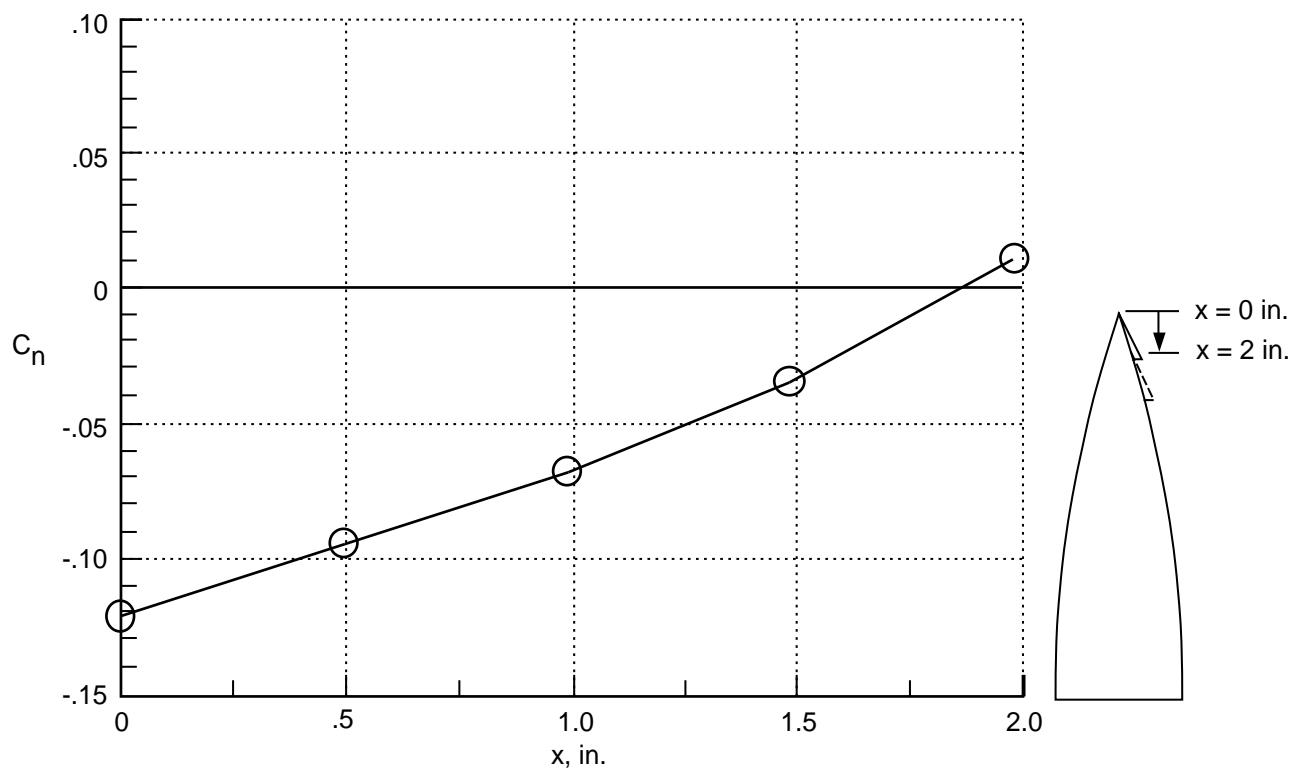
Figure 50. Effect of axial translation on yawing moment coefficient at $\alpha = 50°$ with 1/4 length .3 short ogive strake at $\phi_S = 90°$ with full configuration.
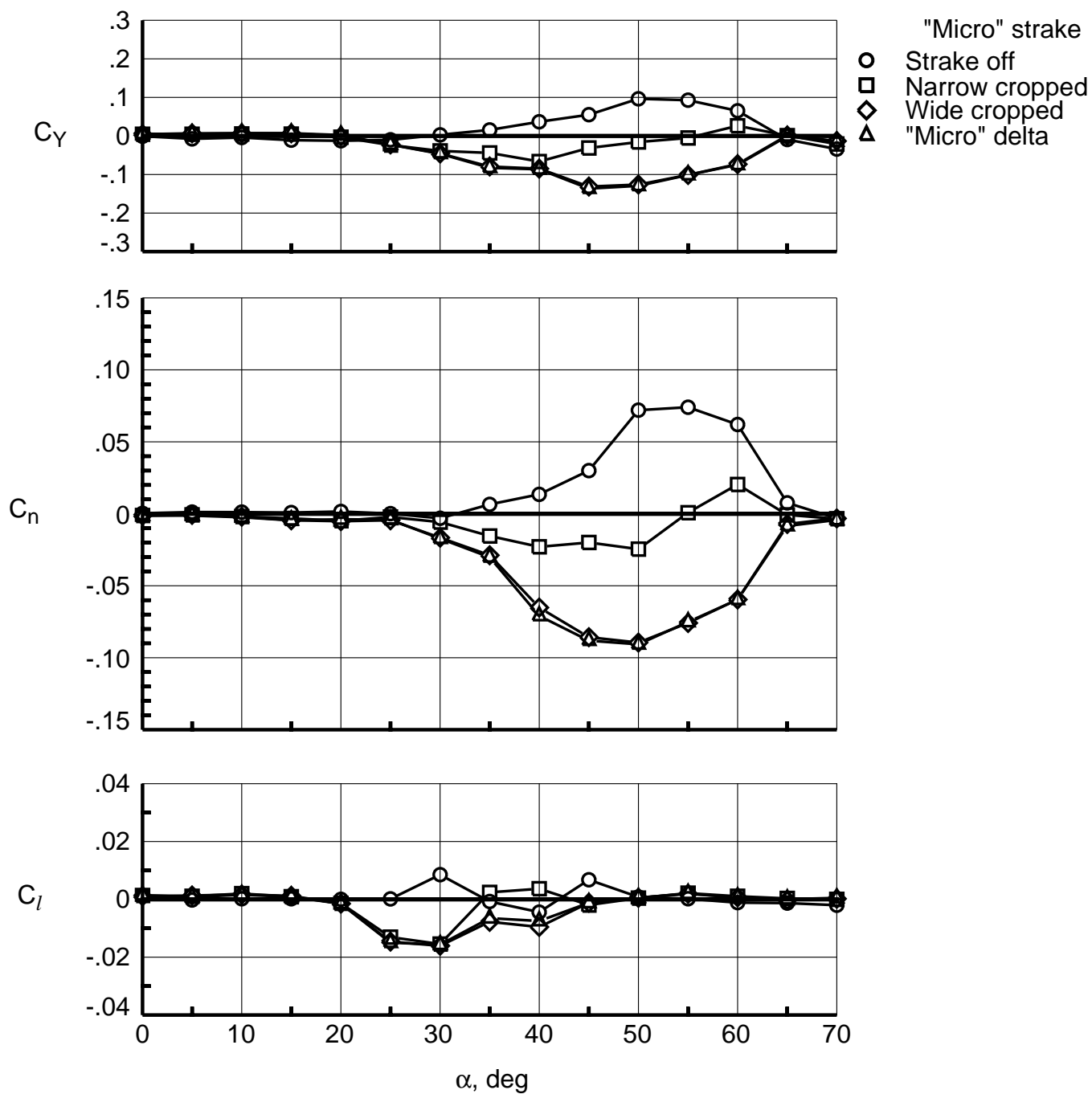
Figure 51. Effect of "micro" strakes on lateral-directional characteristics with 1/16 length "micro" strakes at $\phi_S = 104°$ with full configuration.
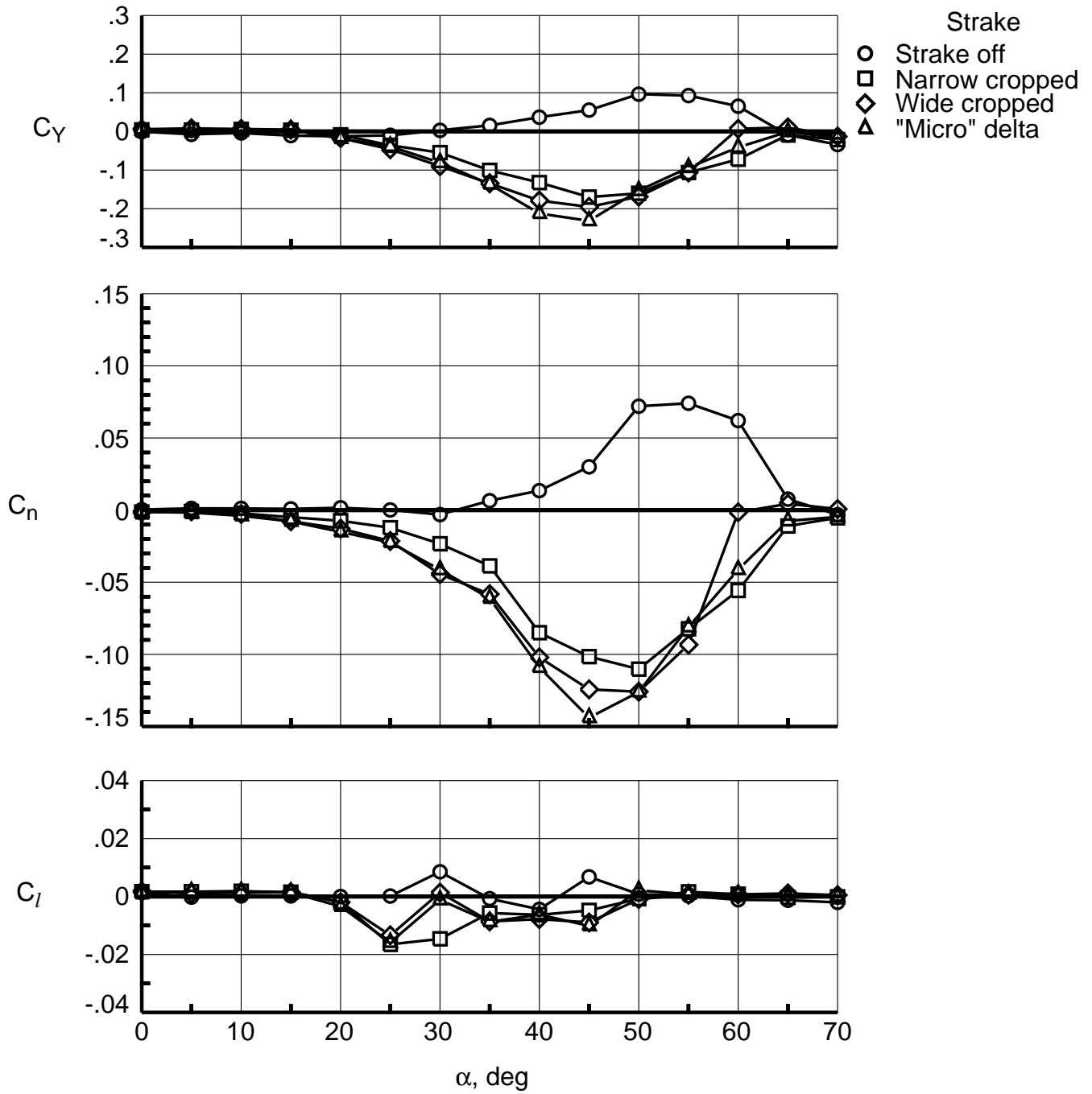
Figure 52. Effect of "micro" strakes on lateral-directional characteristics with 1/8 length "micro" strakes at $\phi_S = 104°$ with full configuration.
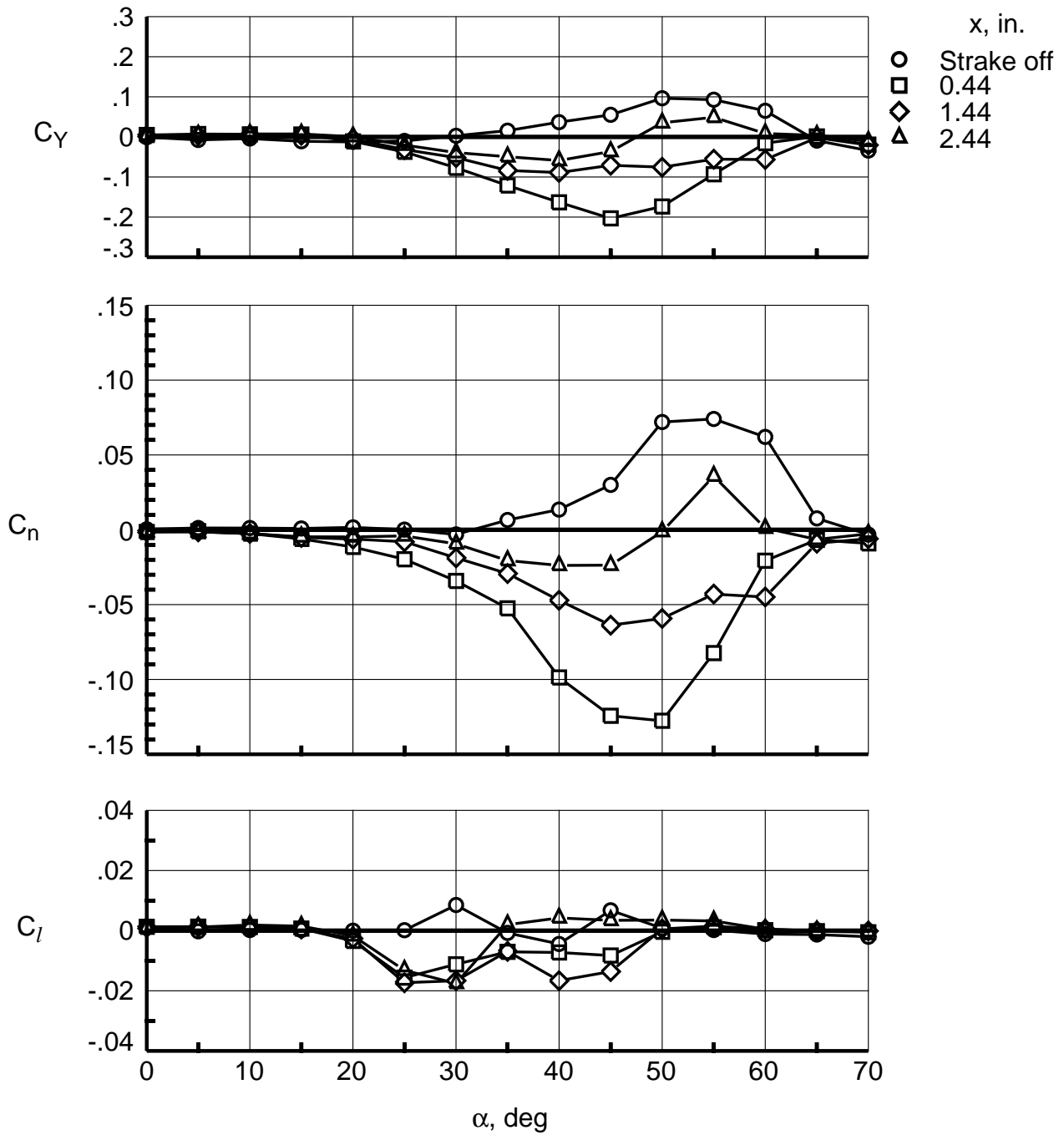
Figure 53. Effect of axial translation on lateral-directional characteristics with 1/8 length wide cropped "micro" strake at $\phi_S = 90°$ with full configuration.
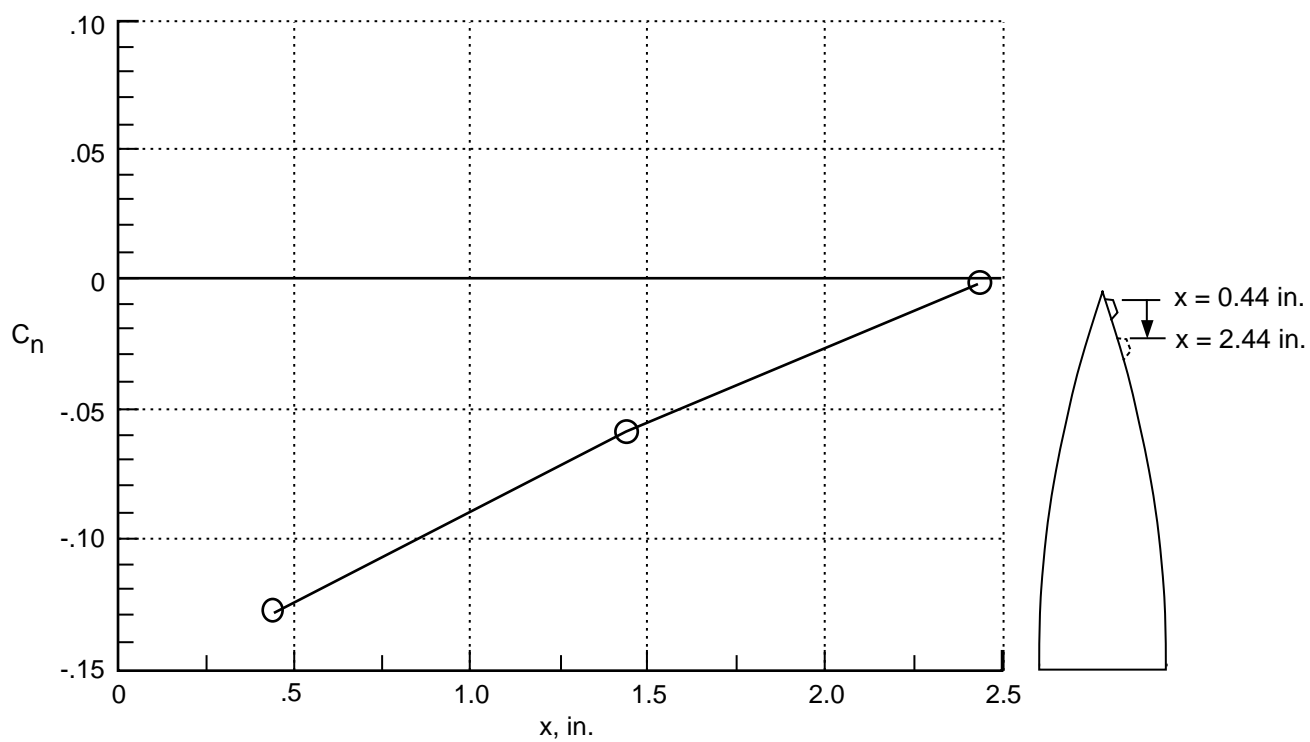
Figure 54. Effect of axial translation on yawing moment coefficient at $\alpha = 50°$ with 1/8 length wide cropped "micro" strake at $\phi_S = 90°$ with full configuration.
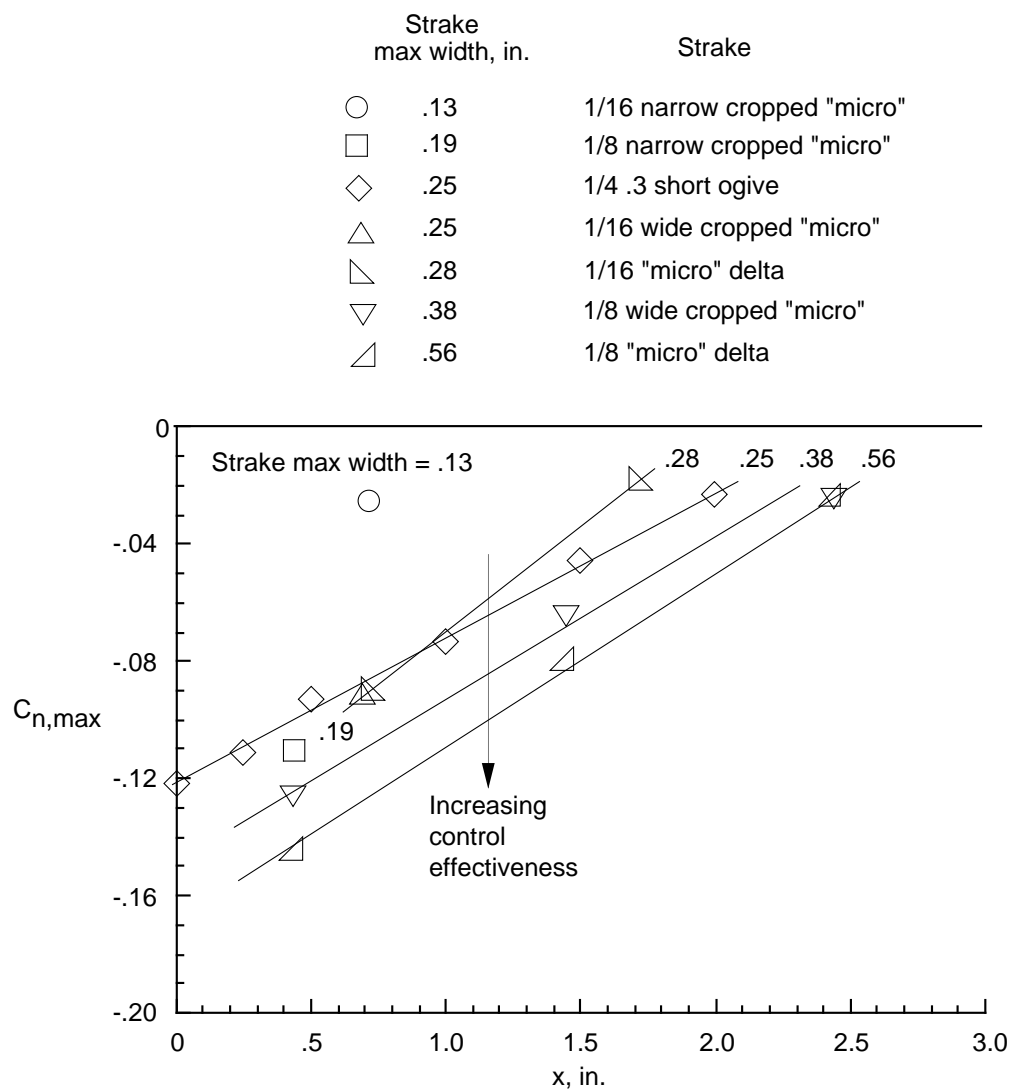
Figure 55. Effect of strake axial position on maximum yawing moment coefficient. Solid lines indicate constant values
    of maximum strake widths.

REPORT DOCUMENTATION PAGE

Public reporting burden for this collection of information is estimated to average 1 hour per response, including the time for reviewing instructions, searching existing data sources, gathering and maintaining the data needed, and completing and reviewing the collection of information. Send comments regarding this burden estimate or any other aspect of this collection of information, including suggestions for reducing this burden, to Washington Headquarters Services, Directorate for Information Operations and Reports, 1215 Jefferson Davis Highway, Suite 1204, Arlington, VA 22202-4302, and to the Office of Management and Budget, Paperwork Reduction Project (0704-0188), Washington, DC 20503.

1. AGENCY USE ONLY *(Leave blank)*	2. REPORT DATE April 1997	3. REPORT TYPE AND DATES COVERED Technical Paper

4. TITLE AND SUBTITLE
Exploratory Investigation of Forebody Strakes for Yaw Control of a Generic Fighter With a Symmetric 60° Half-Angle Chine Forebody°

5. FUNDING NUMBERS
WU 505-68-30-01

6. AUTHOR(S)
Holly M. Ross and Matthew J. O'Rourke

7. PERFORMING ORGANIZATION NAME(S) AND ADDRESS(ES)

NASA Langley Research Center
Hampton, VA 23681-0001

8. PERFORMING ORGANIZATION REPORT NUMBER
L-17519

9. SPONSORING/MONITORING AGENCY NAME(S) AND ADDRESS(ES)

National Aeronautics and Space Administration
Washington, DC 20546-0001

10. SPONSORING/MONITORING AGENCY REPORT NUMBER
NASA TP-3604

11. SUPPLEMENTARY NOTES
Ross: Langley Research Center, Hampton, VA; O'Rourke: Lockheed Martin Engineering & Sciences Company, Hampton, VA.

12a. DISTRIBUTION/AVAILABILITY STATEMENT

Unclassified–Unlimited
Subject Category 02
Availability: NASA CASI (301) 621-0390

12b. DISTRIBUTION CODE

13. ABSTRACT *(Maximum 200 words)*

Forebody strakes were tested in a low-speed wind tunnel to determine their effectiveness producing yaw control on a generic fighter model with a symmetric 60° half-angle chine forebody. Previous studies conducted using smooth, conventionally shaped forebodies show that forebody strakes provide increased levels of yaw control at angles of attack where conventional rudders are ineffective. The chine forebody shape was chosen for this study because chine forebodies can be designed with lower radar cross section (RCS) values than smooth forebody shapes. Because the chine edges of the forebody would fix the point of flow separation, it was unknown if any effectiveness achieved could be modulated as was successfully done on the smooth forebody shapes. The results show that use of forebody strakes on a chine forebody produce high levels of yaw control, and when combined with the rudder effectiveness, significant yaw control is available for a large range of angles of attack. The strake effectiveness was very dependent on radial location. Very small strakes placed at the tip of the forebody were nearly as effective as very long strakes. An axial translation scheme provided almost linear increments of control effectiveness.

14. SUBJECT TERMS
Chine forebody aerodynamics; Forebody controls, Forebody strakes, Yaw control; High angle of attack

15. NUMBER OF PAGES
69

16. PRICE CODE
A04

17. SECURITY CLASSIFICATION OF REPORT Unclassified	18. SECURITY CLASSIFICATION OF THIS PAGE Unclassified	19. SECURITY CLASSIFICATION OF ABSTRACT	20. LIMITATION OF ABSTRACT